Volume Electron Microscopy with 64 Beams and Optical Transmission Detection

Kievits, A.J.

DOI
10.4233/uuid:68281e49-f57a-4307-b369-9866c0299323

Publication date
2025

Document Version
Final published version

Citation (APA)
Kievits, A. J. (2025). *Volume Electron Microscopy with 64 Beams and Optical Transmission Detection*. [Dissertation (TU Delft), Delft University of Technology]. https://doi.org/10.4233/uuid:68281e49-f57a-4307-b369-9866c0299323

Volume electron microscopy with 64 beams and optical transmission detection

Arent Kievits

Volume electron microscopy with 64 electron beams and optical transmission detection

Volume electron microscopy with 64 electron beams and optical transmission detection

Proefschrift

ter verkrijging van de graad van doctor
aan de Technische Universiteit Delft,
op gezag van de Rector Magnificus prof. dr. ir. T. H. J. J. van der Hagen,
voorzitter van het College voor Promoties,
in het openbaar te verdedigen op vrijdag 27 juni 2025 om 12:30 uur

door

Arent Johan KIEVITS

Master of Science in Nanobiology,
Technische Universiteit Delft, Nederland
Erasmus Universiteit Rotterdam, Nederland

geboren te Leeuwarden, Nederland.

Dit proefschrift is goedgekeurd door de promotoren.

Samenstelling promotiecommissie:

Rector Magnificus,	voorzitter
Prof. dr. ir. J. P. Hoogenboom,	Technische Universiteit Delft, promotor
Dr. ir. C. S. Smith,	Technische Universiteit Delft, promotor
Onafhankelijke leden:	
Prof. dr. G. H. Koenderink,	Technische Universiteit Delft
Prof. dr. R. A. Fleck,	King's College London, Verenigd Koninkrijk
Prof. dr. B. Rieger,	Technische Universiteit Delft
Dr. L. M. Collinson,	The Francis Crick Institute, Verenigd Koninkrijk
Dr. B. N. G. Giepmans,	Universitair Medisch Centrum Groningen
Dr. A. Mohammadi-Gheidari	Technische Universiteit Delft, reservelid

Het onderzoek in dit proefschrift is gedaan in de Microscopy Instrumentation and Techniques groep, departement Imaging Physics, Faculteit Technische Natuurwetenschappen, Technische Universiteit Delft.

Trefwoorden: volume electron microscopy, array tomography, FAST-EM, optical scanning transmission electron microscopy
Geprint door: Ridderprint | www.ridderprint.nl

Omslag: Theatrale afbeelding van multibundel scannende elektronenmicroscopie met optische detectie.
Stijl: TU Delft Huisstijl, met aanpassingen door Moritz Beller
`https://github.com/Inventitech/phd-thesis-template`

De omslag is ontworpen door MY dissertation designs

This is the time in your life where you need not discover who someone else is within you, but who yóu are within you

Cory Wong

Contents

Summary

Imaging across multiple scales can provide valuable insights into complex biological systems, thereby enhancing the understanding of physiology in healthy and diseased states. Electron microscopy (EM) is a technique that resolves the nanoscale structure of tissues and cells on millimeter length scales, thus making it an effective tool for studying intricate biological processes. Recently, several EM techniques have been established that reveal the three-dimensional structure, collectively referred to as volume electron microscopy (volume EM).

Traditionally, 3D reconstructions of tissue and cells are achieved by cutting serial thin sections of resin-embedded samples, mounting them on support grids, and imaging with transmission EM. Today, volume EM includes several complementary techniques, each with different resolutions and field-of-view. For example, in array tomography, serial sections are placed on a solid substrate and imaged with scanning EM. In serial block-face scanning EM, a thin tissue slice is removed by an *in situ* ultramicrotome, and the exposed tissue block face is imaged. With a focused ion beam in a scanning EM, an even thinner slice can be precisely removed. The expanded toolkit has extended volume EM beyond its original application in neuroscience to a wide range of fields.

Advances in volume EM have largely been made possible by improvements in instrumentation, such as more automated workflows and faster and sensitive detectors. Nevertheless, the limited throughput of EMs remains a major bottleneck, especially for large volume imaging. Recent methodological innovations are, however, making possible the imaging of millimeter-sized samples and small organisms. In transmission EM, the throughput is limited by time-consuming sample grid replacement, stage movements and limited field-of-view at high magnification. Reel translation systems with transparent tape, faster sample stages, larger camera arrays and advanced beam deflection have solved these bottlenecks and increased throughput.

On the other hand, the acquisition speed in scanning EM is hindered by the maximum beam current allowing for high resolution imaging. Multibeam scanning EM circumvents this limit by using multiple beams that scan the sample in parallel. However, the signals originating from multiple beams must be separately detected. This problem is tackled differently in two (commercial) implementations of multibeam scanning EM. In MultiSEM, secondary electrons generated by the primary beam impact are collected from each beam and detected. In FAST-EM, optical detection is used to separate the signals. The latter approach, referred to as Optical Scanning Transmission EM (OSTEM), places ultrathin biological sections on a scintillator substrate that converts transmitted electrons into photons, which are then detected. OSTEM provides large, unobstructed views by avoiding the grid supports used in traditional transmision EM and scanning transmission EM.

The introduction of new microscopy techniques requires development, benchmarking and sharing of workflows for applications. Workflows for high-throughput volume EM techniques, such as parallel transmission EM and MultiSEM, are now being shared. In a

similar way, FAST-EM, a 64-beam scanning transmission EM developed by Delft University of Technology and industry partners, is aimed at improving volume EM throughput and automation. We first benchmarked OSTEM (implemented in FAST-EM) as a detection technique for large-scale volume EM. We compared it with existing detection techniques in scanning EM as well as scanning transmission EM, including backscattered (BSD) and secondary electron detection (SE) and annular dark field scanning transmission EM (ADF-STEM). OSTEM offers comparable apparent image contrast, signal-to-noise ratio, and resolution to BSD and SE at optimal landing energies. While BSD with a negative stage bias and ADF-STEM may outperform OSTEM for moderate to long dwell times, OSTEM outperforms biased backscattered electron detection at shorter dwell times, which are preferred in large-scale volume EM. Experimental data further suggests that the signal from the scintillator partially saturates, indicating potential for further optimization in substrate design and dwell time reduction.

We subsequently incorporated an early-adopter FAST-EM system into a workflow for array tomography. It is shown that high-resolution FAST-EM array tomography datasets can be acquired, stitched and aligned to form complete, coherent 3D volumes of tissues and cell cultures. Additionally, FAST-EM is shown to be compatible with conventional EM sample preparation protocols. Image analysis tools developed for other volume EM modalities can be directly applied to FAST-EM datasets. Despite being significantly faster than single-beam scanning EMs, FAST-EM currently has a lower throughput than Multi-SEM and parallel transmission EM. To reach the highest possible throughput, the overhead should be minimized. Moreover, imaging parameters and detection conditions have to be optimized towards shorter dwell times. A redesign of the electron-optical column can possibly lead to even higher throughput.

Previously undocumented artifacts were identified through the combination of conventional biological sample preparation, optical transmission detection with solid scintillator substrates and multibeam scanning EM (FAST-EM). Interactions between the sample and substrate boundary can lead to artifacts that obstruct the view. OSTEM is shown to be sensitive to substrate surface variations, which may result in image artifacts that obscure the biological ultrastructure. Repeated exposure of certain sample regions by scanning with multiple beams leads to contrast differences in OSTEM images. The effective signal-to-noise ratio and contrast may be lowered by detector crosstalk. Together, these image artifacts impact the quality of FAST-EM datasets and limit their interpretability. Nonetheless, many of these artifacts have been mitigated through modifications in sample preparation, substrate quality control, sample pre-irradiation, and detection setting adjustments.

FAST-EM expedites array tomography workflows by increasing acquisition speeds, thereby enabling new experimental designs such as examining large populations of cell organelles under varying biological conditions. Nevertheless, it shares some limitations of conventional array tomography, including voxel size anisotropy due to the limited section thickness (40–100 nm). Achieving near-isotropic voxel resolution in large-scale imaging could be feasible through a combination of iterative broad-ion beam milling and high-throughput FAST-EM imaging. Regular array tomography also allows for correlative fluorescence microscopy, enabling selective labelling of biomolecules, an approach which is not yet possible with FAST-EM array tomography. Therefore, future research should explore suitable substrates for correlative light and electron microscopy with FAST-EM.

Samenvatting

Met beeldvorming op verschillende lengteschalen kan waardevol inzicht gekregen worden in complexe biologische systemen. Op deze manier wordt het begrip vergroot van de fysiologie in gezonde en zieke toestanden. Elektronenmicroscopie (EM) is een techniek die de kleinste structuur van weefsels en cellen op millimeterschaal kan vastleggen, wat het een effectief hulpmiddel maakt voor het bestuderen van biologische processen. Recentelijk zijn verschillende EM-technieken ontwikkeld die de driedimensionale structuur weergeven, gezamenlijk aangeduid als volume-elektronenmicroscopie (volume EM).

Traditioneel worden 3D-reconstructies verkregen door opeenvolgende dunne sneden (coupes) van in kunsthars ingebedde weefsels en cellen te snijden, deze op kleine steunroosters te monteren en met transmissie EM te bekijken. Tegenwoordig omvat volume EM verschillende complementaire technieken, elk geschikt voor verschillende volumegroottes en resoluties. Bij array-tomografie, bijvoorbeeld, worden seriële coupes in geordende lintjes (arrays) gesneden, op een vast substraat geplaatst en opgenomen met scannende EM. Bij seriële blok-oppervlak scannende EM wordt een dun weefsellaagje verwijderd met een ultramicrotoom gesitueerd in de vacuümkamer van de microscoop. Vervolgens wordt het blootgestelde blokoppervlak in beeld gebracht. Met een gefocusseerde ionenbundel in een scannende EM, kan nog preciezer een heel dun laagje verwijderd worden. Deze toevoegingen aan de “gereedschapskist” hebben ervoor gezorgd dat volume EM nu in diverse wetenschappelijke velden wordt toegepast.

Vooruitgang in volume EM is grotendeels mogelijk gemaakt door verbeteringen in instrumentatie, zoals geautomatiseerde workflows en snellere, gevoeligere detectoren. Desondanks blijft de beperkte verwerkingssnelheid van EM een belangrijk knelpunt, vooral bij grootschalige beeldvorming. Recente methodologische innovaties maken het echter mogelijk om volledige reconstructies te maken van millimeter grote monsters en zelfs kleine organismen. In transmissie EM wordt de doorvoer doorgaans beperkt door tijdrovende wisselingen van het preparaat, veranderingen van de preparaattafelpositie en het beperkte beeldveld bij hoge vergroting. Snellere preparaattafels, grotere camera-arrays, transportsystemen met transparante tape en geavanceerde snelle bundelafbuiging hebben deze knelpunten opgelost en de doorvoer verhoogd.

In scannende EM wordt de acquisitiesnelheid beperkt door de hoogst mogelijke bundelstroomsterkte die nog beeldvorming met hoge resolutie toestaat. Multibundel scannende EM omzeilt deze beperking door meerdere bundels parallel over het preparaat te scannen. Signalen van meerdere bundels moeten echter apart worden gedetecteerd. Twee bestaande (commerciële) multibundel scannende EMs pakken dit probleem verschillend aan. Bij “MultiSEM” worden secundaire elektronen, die door de primaire bundelimpact worden gecreëerd, per bundel apart opgevangen en gedetecteerd. Bij “FAST-EM” wordt optische detectie gebruikt, waarbij ultradunne biologische coupes op een scintillatorsubstraat worden geplaatst dat doorgelaten elektronen omzet in fotonen. Dit laatste wordt Optische Scannende Transmissie EM (OSTEM) genoemd. OSTEM maakt een groot, onbe-

lemmerd beeldveld mogelijk door het vermijden van de steunroosters die gebruikt worden in transmissie EM en scannende transmissie EM.

Nieuwe microscopietechnieken vereisen de ontwikkeling, het benchmarken en delen van workflows voor toepassingen. Workflows voor hoge-doorvoer volume-EM-technieken, zoals parallele transmissie EM en MultiSEM, worden momenteel gepubliceerd en gedeeld. FAST-EM, een 64-bundel scannende tranmissie EM ontwikkeld door de TU Delft en industriële partners, richt zich op het verbeteren van de doorvoer en automatisering van grootschalige EM. Als eerste hebben we daarom OSTEM, toegepast in FAST-EM, gebenchmarkt als een detectietechniek voor grootschalige (volume) EM. We vergeleken OSTEM met bestaande detectietechnieken in scannende EM en scannende transmissie EM, zoals terugverstrooide elektronendetectie (BSD) en secundaire elektronendetectie (SE) en annulaire donkere veld scannende transmissie EM (ADF-STEM). OSTEM levert biologische plaatjes met een vergelijkbaar beeldcontrast, en vergelijkbare signaal-ruisverhouding en resolutie als bij BSD en SE bij optimale bundelenergie. ADF-STEM en BSD met een negatieve voorspanning op de preparaattafel presteren beter dan OSTEM bij middellange tot lange belichtingstijden. Echter, bij korte belichtingstijden die de voorkeur hebben bij grootschalige volume EM, presteert OSTEM beter dan BSD met voorspanning. Experimentele resultaten suggereren verder dat het signaal van de scintillator gedeeltelijk verzadigt, wat wijst op mogelijkheden voor verdere optimalisatie in substraatontwerp en belichtingstijdverkorting.

Daarna hebben we een pioniersmodel van FAST-EM geïntegreerd in een workflow voor array-tomografie. We hebben aangetoond dat FAST-EM datasets met hoge resolutie kunnen worden opgenomen en samengevoegd tot complete, coherente 3D-volumes van weefsels en celculturen. FAST-EM is compatibel met gangbare protocollen voor EM-monsterpreparatie. Daarnaast kunnen hulpmiddelen voor de beeldverwerking en -analyse van andere volume EM methoden direct worden toegepast. Hoewel FAST-EM significant sneller is dan normale scannende EM, heeft het systeem momenteel een lagere verwerkingssnelheid dan MultiSEM en parallelle transmissie EM. De hoogste verwerkingssnelheid kan worden bereikt door het minimaliseren van de overhead en het optimaliseren van acquisitieparameters en detectieomstandigheden voor kortere belichtingstijden. Een herontwerp van de elektronen-optische kolom kan mogelijk leiden tot nog hogere doorvoercapaciteit.

Door het combineren van conventionele biologische monsterpreparatie, optische transmissiedetectie met scintillatorsubstraten en mSEM kwamen we niet eerder gedocumenteerde artefacten tegen. Interacties tussen het monster en het substraatoppervlak kunnen artefacten veroorzaken die het zicht belemmeren. OSTEM blijkt gevoelig te zijn voor variaties in het substraatoppervlakte, wat kan resulteren in beeldartefacten die de biologische ultrastructuur verdoezelen. Herhaalde blootstelling van bepaalde monstergebieden door het scannen met meerdere elektronenbundels leidt tot contrastverschillen in OSTEM-beelden, en de effectieve signaal-ruisverhouding en het contrast kunnen worden verlaagd door signaaloverdracht tussen detectoren. Samen beïnvloeden deze beeldartefacten de kwaliteit van FAST-EM datasets en beperken ze hun interpreteerbaarheid. Desalniettemin zijn veel van deze artefacten verminderd of aangepakt door aanpassingen in de monstervoorbereiding, substraatkwaliteitscontrole, voorbestraling van het monster en aanpassingen in de detectie-instellingen.

FAST-EM versnelt array-tomografie workflows met behulp van hogere acquisitiesnelheden. Hierdoor kunnen nieuwe onderzoeksvragen kunnen worden beantwoord, zoals hoe de structuur van grote populaties celorganellen verandert onder verschillende biologische omstandigheden. Het deelt echter enkele beperkingen van conventionele array-tomografie, zoals anisotrope volume pixels door de beperkte coupedikte (40−100 nm). Het verkrijgen van bijna isotrope volume pixels in grootschalige beeldvorming kan haalbaar zijn door een combinatie van iteratief breed-ionenbundelfrezen en FAST-EM beeldvorming. Conventionele array-tomografie wordt ook gebruikt in combinatie met correlatieve fluorescentiemicroscopie, waarmee biomoleculen selectief kunnen worden gelabeld. Dit kan nog niet in FAST-EM array-tomografie. Daarom moeten er in toekomstig onderzoek geschikte substraten verkend worden voor correlatieve licht- en elektronenmicroscopie met FAST-EM.

Acknowledgments

I think it is fitting to put the acknowledgements here. It is, for many, probably the second most interesting thing to read after the summary.

It has been more than 10 years since I first arrived in Delft, which marked the start of an intellectual journey that came to an end by finishing and defending this dissertation. I have met a lot of special people in those 10 years, without whom this dissertation would never have come about. You have truly made this PhD a great and instructive experience!

First of all I would like to thank my promoter and supervisor Jacob Hoogenboom for the opportunity to work on this project. Jacob, you have created an interesting, collaborative environment of research groups and companies which was very fruitful to the project, as well as having been highly enjoyable to work in. I am grateful for all your suggestions and feedback over the years that have significantly improved the quality of the research and output. Finally, thank you for the opportunity to publish in the new journal Methods in Microscopy.

Elizabeth, unfortunately you had to step down as copromotor before the project ended, but it was a joy to be part of the Zebrafish lab and to learn about fish biology! I wish you all the best in the US. Carlas, thank you for stepping in afterwards.

Starting a PhD amidst the COVID pandemic was definitely a challenge, but fortunately I ended up in a warm and supportive environment called MInT. Vidya, Maurice, Qiangrui, Rui, you were great office mates. Thank you for the listening ear and your advice, which helped keep my spirits high. Vidya, I appreciate your patience, warmth and discipline. Qiangrui, I wish you all the best with your happy family! Aya, Xin, Vidya, Laura, Huma, Marco Locarno, Zhenzhen, Mariska, you entertained me well with your excellent taste in food, amazing cooking and baking skills and wonderful artistic crafts. Bless you for sharing this with us! Laura, it was great to share our mutual interest in music. Marco, Laura, Cristiano, thank you for instilling me with the best things of your country. A big shoutout to the student room for providing the necessary entertainment, both intellectually and nonsensically: Stijn, Marco Post (continuing the entertainment as PhD candidates); Célina, Quincy, Léon, Jordan, Wieke, Danin, Max, Jelte, Bram, Lars, Boyd, Loek, Tim, Reint, Julie and Adriana. My time in MInT is surely marked with many hilarious lunch break conversations and eccentric food tastings often initiated by you.

It has been a great pleasure to be under the “High Tree Gang” umbrella. We had some excellent group outings (including the unexpected paint job of my new apartment in Rijswijk, for which I remain eternally grateful to you!). Ryan, you have been an incredible resource for the project. From teaching me SEM of thin sections to troubleshooting Render Web Services, your work really was at the basis of this dissertation. Sina, you were a nice buddy during the CPO course. Radim, I appreciate your attitude regarding life and love for your family. Mathijs, Yoram, thank you for your helpful feedback during the work discussions and the pleasant beer nights during COVID. Ernest, thank you for your wise words. Daan, your practical attitude and handiness have been incredibly helpful in

experiments, given my not so handiness. Célina, I'm sorry we had to go through so much troubleshooting with the FAST-EM, but at least we could do it together for a while; Stijn, I wish you all the best with future troubleshooting ;-). Monika, I'm sure you will see the open ends on OSTEM to a satisfactory conclusion! Ali, you taught me a lot about charged particle optics and FAST-EM. Mike, Martijn, Sarnia, I enjoyed your company and positive attitude towards your projects. Last but not least: Marc, Rayen, Luna, Wilco, although being around briefly, you have made a lasting impact on my PhD trajectory and in fact your projects are still being continued by others!

The support of certain amazing, hardworking people in MInT has been a key factor in the successful outcome of my project. Yvonne, thank you for your kindness and helping me with onboarding at TUD on short notice. This gratitude is also extended to Anjella, Malee, Anneloes and Hannah for keeping everything running smoothly in the background. Meg and Anne, thank you for doing incredible stuff in the cleanroom and being so supportive and kind. The same holds true for you, Carel. You are dearly missed by everyone at MInT, as a colleague and a friend. Dustin, it truly amazes me how much you know about SEM and FIB columns. Thank you for entertaining me with your company while fixing all my setups, it was great to complain together (with or without a beer at the TeePeeCafé). Han, thank you for fixing my detector multiple times and making sure we do not run out of the essential coffee life support. Tibbe, I am eternally grateful to you for saving our precious server and data from getting wiped. Your excellent Python coding skills have vastly improved our data processing workflows. It was nice getting stuck in your office for the occasional chitchat.

One of the most appealing and potentially far-reaching aspects of my PhD have been the many collaborations. Ben, it has been a pleasure to work with your group at the University Medical Center Groningen. You are an excellent host and an even more formidable researcher and group leader. Peter, thank you for all the work that we did together and the many lengthy and interesting discussions about multiple topics in my thesis. I appreciate your eye for detail and your creativity when explaining unseen phenomena. Although you may not admit it yourself, I think you are definitely a technical person ;-). Pascal, Ahmad, Anouk, Daan, Kim, Jeroen, Anusha, thank you for making me feel welcome on my trips to Groningen! Nalan, Cilia, I enjoyed our collaboration and my visits to Utrecht. Nalan, it was a pleasure to get introduced by you as speaker at several conferences (a coincidence?). Gao, Elize, I hope the collaboration between Erasmus MC and TUD will continue!

I would also like to acknowledge the people behind FAST-EM for their support. Andries, I appreciated your commitment towards the progress of implementing FAST-EM and solving problems together. Guido, Marre, Thera, Wilco, Marit, thank you for all the troubleshooting and software support, without you I might still be acquiring data right now... Marc, Gerard, Robert, I have enjoyed working together on the IMDAP project and I appreciate Technolution's interest in the FAST-EM.

As part of the PhD council I tried to make some incremental steps towards improving the life of the average PhD candidate at our faculty. It is impressive to write down such a long list of people that have contributed towards the same goal: Milan, Céline, Reza, Isabell, Tanja, Matteo, David, Alberto, Sarika, Siva, Martijn, Rohit, Rik, Pierfrancesco, Sagarika, Swareena, Sid, Jeffrey, Davide, Adarsh, Miriam, Héctor, Koushik, Sercan, Chris, Kalani, Tim, it was a pleasure discussing serious and less serious topics about the PhD trajectory with you! The same can be said about taking issues from the PhD council to the OdC: Karin, Heleen, Johan, Hylkje, Daan, Martin, Laura, Swapna, Harry, Leonie and of course Paulien and Annekee, thank you for your genuine interest and thinking along. I'm really happy to see that the interests of employees at our faculty are well represented.

Tijdens mijn promotietraject was het fijn om door vrienden en familie te worden gesteund. Niels, Dirk, Daniël, het is een genoegen om met jullie een vriendschap te delen vanaf het begin van de bachelor Nanobiologie. Daarnaast is het fijn om mijn andere grote passie, die van muziek, te kunnen blijven delen met zo veel gelijkgestemden en vrienden: Laurens, Stijn, Victor, Sabine, Sebastiaan en alle andere lieve mensen van Valerius; Donnie, Michael, Sandra, Daniël, Thorben en de rest van Open Studio, ontzettend bedankt hiervoor!

Ik heb een groot gedeelte van mijn studententijd en daarna mogen genieten van een ontzettend leuke vriendengroep: Sep, Nina, Florian, Walewijn, Koenraadt, Silvan, Matthijs, Anneriet, Maarten, Sarah, Pepijn, Siem, Anne, Stephan, Wietske, Robin, Tim, Roemer, Oxana, Rens, Alies, Jurjen, Hidde, Jelte, Micha, Sasha, Judith, Alexander, Luna, Dimitri, Justin, Tristan, Mark, Onno, Eline, Fu-Cui, Sven en Thomas, allen bedankt voor de vele gezellige uitjes, weekendjes weg, vakanties, reünies, mooie avonden en vergeten avonden. Op malckander! Matthijs, Anneriet, Robin, Anne, Tim, Sasha, het is mooi om net als jullie hetzelfde pad van de wetenschap te bewandelen. Zet hem op! Jelte, Koen, Siem, Rens, bedankt voor jullie inzet om mij (letterlijk) op de been te houden.

Het is ontzettend fijn om af en toe te ontsnappen naar de rust en stilte van Terschelling. Elke keer voelt het een beetje als thuiskomen. Sil, Mees, het is erg leuk om af en toe bijpraten, ook al zijn we zulke andere wegen ingeslagen. Gert, Carla en alle vrienden van de familie Kievits, bedankt voor jullie oprechte interesse en de gezelligheid bij elk wederzien.

Nienke, we kennen elkaar nog niet zo lang, maar het is tot nu toe al een onvergetelijk avontuur met jou gebleken. Pap, Mam, Meike, Brent, en natuurlijk Klaas & Nel, ontzettend bedankt voor jullie begrip en onvoorwaardelijke steun. Ik hou van jullie!

1

Introduction

1.1 Structure implies function

From a structural point of view, a living organism is a complex, hierarchical organization of biomolecules. This organization exhibits specific characteristics and processes essential to maintaining and replicating itself. A central aim in biological research fields such as neuroscience and cell biology is to understand the structure of organisms, from the organ level down to the molecular scale, in order learn more about their functioning. A change in function caused by a molecular (disease) mechanism may affect tissue organization on the large scale. For example, in IgA nephropathy or Berger's disease, an autoimmune response leads to inflammation of the glomeruli (kidney filtering units) and subsequent ultrastructural damage to the endothelial tissue [1]. This has disruptive effects on kidney function at the organ scale. To visualize the nanoscale structure in context of the full tissue, an imaging technique is required that captures all these scales at the same time. Microscopy is typically used for this type of purpose.

There exist several complementary microscopy techniques capable of imaging across length scales (Figure 1.1), with each having different resolving power and field-of-view. Electron microscopy (EM) is uniquely positioned in this landscape since it is capable of resolving the nanoscale structure of tissues and cells on millimeter length scales. Recently, EM techniques have emerged that resolve the three-dimensional structure with nanometer resolution, which are collectively referred to as volume electron microscopy (vEM) [2]. The unique capabilities of vEM have been utilized to generate comprehensive mappings of cell organelle interactions [3, 4]. On the other end, vEM can be used to trace the smallest, finest branches of neurons and their contact sites to generate wiring diagrams of the nervous systems of small organisms [5, 6, 7, 8, 9]. Whatever the objective, contemporary EM techniques are now capable of producing image datasets spanning millions of cubic micrometers with nanometer resolution that shed light on complex biological processes in 3D.

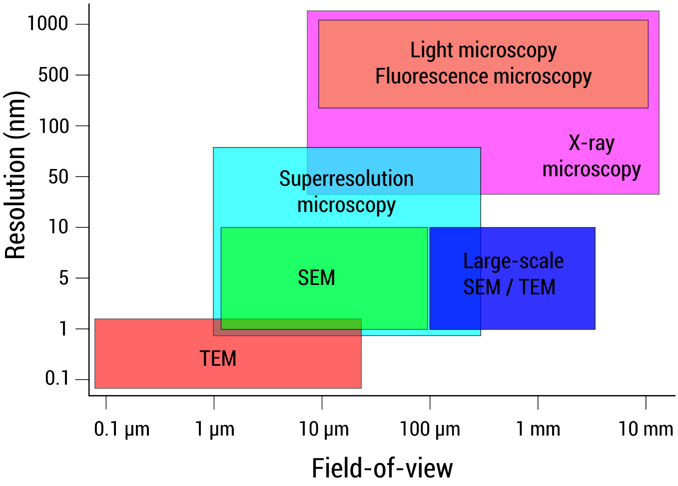

Figure 1.1: Resolution and field-of-view (FOV) of tools for imaging across scales. Light and x-ray microscopy are powerful techniques for imaging on a scale of (tens of) micrometers to millimeters, but they offer limited spatial resolution. Transmission electron microscopy (TEM) offers sub-nanometer resolution, albeit with limited FOV. Scanning electron microscopy (SEM) allows for larger FOVs, but at lower spatial resolution than TEM. Large-scale SEM and TEM extend the FOV to millimeters. Super-resolution microscopy bridges the gap between electron microscopy and light and x-ray microscopy, albeit based on selective labeling and localization of proteins. More recent techniques such as MINFLUX [10] have achieved 1 nm localization precision at FOVs of 10-15 μm or even Ångström resolution (at small FOVs) [11]. Figure based on illustrations from de Boer, Hoogenboom & Giepmans [12] and Peddie et al. [2].

.

1.2 The bottleneck in electron microscopy

In electron microscopes, electrons are emitted from a source, and accelerated towards a sample through a series of electromagnetic and electrostatic lenses. Upon impact with the sample, a plethora of physical interactions take place; electrons may collide with atoms and lose energy, generate additional electrons, cause emission of radiation or even transmit through the sample (if thin enough). Many of these interactions and their derivatives can be captured with detectors to yield information about the structural and elemental composition of the sample. Based on their mode of operation, two different types of electron microscopy can be distinguished, both of which are employed in vEM. In transmission electron microscopy (TEM), a thin (<200 nm) sample is irradiated and traversed by a coherent, parallel electron beam at high (>50 kV) acceleration voltages. In scanning electron microscopy (SEM), a focused electron beam (probe) is raster scanned over a sample at lower voltages (1-30 kV). In TEM, the image contrast is typically formed by the difference in amplitude or phase of the electron beam after interacting with the sample. In SEM, the contrast is formed by the intensity and energy distribution of electrons that are collected and detected from certain beam incident positions on the sample.

Although EM has very high resolving power (orders of magnitude better than light and X-ray microscopy), the technique inherently suffers from several limitations. The performance of EMs (in nanoscale imaging) can be defined in terms of spatial resolution and acquisition speed. There are several factors that limit resolution for both TEMs and SEMs: environmental influences such as vibrations, thermal fluctuations and external magnetic fields, interference from electronics and contributions from aberrations and alignment errors in electron optics [13]. Many of these factors can be controlled. In TEM, assuming perfect optical alignment, the resolution is largely determined by spherical aberration. This causes a point source to be imaged as a blurred spot with a minimum radius r_s, given by:

$$r_s = 0.5 C_s \alpha^3 \tag{1.1}$$

where C_s is the spherical aberration coefficient of the objective lens and α is the divergence semi-angle of electrons leaving the specimen. To compensate spherical aberrations in TEMs, quadrupole-octopole and sextupole correctors have been developed [14].

The resolution in SEM is governed by the probe size and shape. Electrons that are emitted from a source and accelerated by the extractor appear to come from an area with a finite diameter, which is called the virtual source size. The probe is essentially a demagnified image of the virtual source, blurred by diffraction and aberrations. Thus, it is a product of the contributions from the source image d_I, diffraction d_A and chromatic and spherical aberrations d_C and d_S. To quantitatively describe the probe size, it is necessary to define a common size measure for all contributions: in practice, the diameter that contains 50% of the total current (FW50) is the most consistent measure to use [15]. Using this definition, the different contributions to the probe size can be written as:

$$d_I = M d_v \tag{1.2}$$

where M and d_v are the magnification and virtual source size, respectively;

$$d_A = \frac{0.66e-9}{\sqrt{V_p}\alpha_p} \tag{1.3}$$

where V_p is the acceleration voltage and α_p the half-opening angle of the beam at the sample; and

$$d_C = 0.6 C_C \frac{\delta U}{V_p} \alpha_p \tag{1.4}$$

$$d_S = 0.18 C_S \alpha_p^3 \tag{1.5}$$

where C_C and C_S are the chromatic and spherical aberration coefficients of the objective lens, respectively, and δU is the FW50 of the energy distribution of the electrons. The difference between equation 1.5 and 1.1 comes from the definition of r_s, which is for the total beam width (FW100), instead of the FW50. The minimum probe size d_p can then be calculated using the expression derived by Barth and Kruit [16]:

$$d_p = (((d_I^{1.3} + ((d_A^4 + d_s^4)^{1/4})^{1.3})^{1/1.3})^2 + d_c^2)^{1/2} \tag{1.6}$$

One more parameter is required to characterize the probe size, which is the reduced brightness B_r. B_r is defined as the current dI passing through a surface dA within a solid angle $d\Omega$ at a voltage V:

$$B_r = \frac{dI}{dA d\Omega V} \tag{1.7}$$

It is an important quantity because it characterizes the electron source and is conserved throughout the optical system. The probe current I_p can then be calculated as follows:

$$I_p = B_r \frac{\pi}{4} (d_I)^2 \pi \alpha_p^2 V_p \tag{1.8}$$

Equation 1.6 and 1.8 summarize an important relation between the current and probe size. B_r is limited by the type of electron source that is used. V_p is set by the application. For imaging thin biological sections such as in vEM, a low voltage (<5 keV) is desired to achieve high contrast. This means that I_p can only be increased through α or d_I. However, according to equation 1.4 and 1.5, increasing α leads to larger contributions from chromatic and spherical aberrations. In both situations, it results in a larger probe size. In conclusion, a small probe can contain a limited amount of current.

By extent, the acquisition speed of a single-beam SEM is limited by the maximum probe current allowing for high resolution imaging (4 nm FW50 probe size), since the probe current determines the minimum dwell time that is needed. To illustrate this, let's assume an electron landing energy at the sample of 5 keV, an objective lens with C_c = 2 mm, C_s = 5 mm and a typical Schottky-type Field Emission Gun (FEG) source with d_v = 30 nm and δU = 1 eV. Equations 1.6 and 1.8 yield a minimum probe size of 2.3 nm with a current of 115 pA for the optimized half opening angle. When increasing the current to 1nA, the probe size becomes 7.8 nm. For a landing energy of 2 keV, the minimum probe size is 4.36 nm for a current of 28 pA. For a current of 1 nA, the probe size becomes 30.3 nm instead. This calculation further assumes that Coulomb interactions between electrons are negligible. However, at high probe currents and low landing energies, Coulomb interactions are not negligible and will in fact further increase the probe size. Thus, increasing the beam current in SEM at low landing energies goes at significant expense of resolution.

In TEM, beam current and resolution are indirectly related. Imaging modes such as high resolution TEM (HRTEM) rely on phase contrast, which requires high beam coherence. The coherence width is defined as:

$$X_c = \frac{\lambda}{2\alpha} \tag{1.9}$$

where λ is the wavelength of the electrons and α is the semi-angle from the source. Using equation 1.8, the beam current for which the beam is coherent over the coherence width X_c given by:

$$I_{coh} = B_r V \frac{\pi}{4} X_c^2 \pi \alpha^2 = B_r V \frac{\pi^2}{4} (\frac{\lambda^2}{2}) = 0.93 \times 10^{-18} \mathrm{B}_r \tag{1.10}$$

Thus, there is a maximum current for which the beam is coherent, depending on the brightness of the source. High coherence can be achieved with a high brightness source, such as a FEG source. In conventional bright-field and dark-field TEM, coherence is less important. This implies that beam current or brightness is not a limiting factor; in fact, in these applications typically lower brightness sources are used with a larger source size, which spread the current over a larger area. This may also be preferred when working at lower magnifications with a larger field-of-view. Bright-field TEM allows for nanometer resolution while exposure times per image in vEM applications can be as short as 40 ms [17]. The pixel dwell time equivalent in SEM, assuming similar pixel size, is only 1.1 ns.

An important factor when considering acquisition speed in TEM is the maximum field-of-view at high magnification, which is set by the size of the camera. This means that the imaging of larger regions-of-interest must be achieved by translating the sample, which introduces overhead. A similar limitation exists in SEM, where the maximum field-of-view is set by the scan resolution and the pixel dimensions of the image. Additionally, the maximum area that can be scanned without requiring a stage translation is limited by the beam shift that is allowed without affecting the probe size.

Apart from the limitations of electron microscopes (and their high operating costs), vEM techniques are typically laborious since they involve complex sample preparation and acquisition workflows. These factors imply that high resolution imaging goes at the cost of throughput; indeed, the limited acquisition speed of EMs restricts the number of samples or sample volume that can be analyzed [2].

1.3 Multibeam scanning electron microscopy

There exist several strategies to increase the acquisition speed of electron microscopes. One of these solutions is the central topic of this thesis: multibeam scanning electron microscopy (mSEM). The beam current limitation can be circumvented by using multiple beams scanning the sample in parallel at the same time. Each beam in mSEM carries roughly the same current as in a single-beam SEM. Multi-electron beam technology has several applications besides nanoscale imaging, including lithography [18], electron-beam induced deposition (EBID) [19], wafer defect inspection [20, 21] and metrology. The design criteria for multi-electron beam systems vary based on the desired application.

The development of mSEM at TU Delft was initiated in 2003 by Pieter Kruit and Martijn van Bruggen, who developed a multi-electron beam system for EBID [19]. It was theoretically demonstrated that it is possible to have 100 beams with sub-10 namometer resolution created within a multibeam source (MBS) in a single electron column [22]. Zhang [23] and Gheidari [24] improved upon the first MBS design and further showed experimentally that it is possible to create 196 beams from a single electron source with probe currents and resolution similar to a single-beam SEM. Ren [25] designed and built the first mSEM prototype system, showing that secondary electron detection of multiple beams in a standard SEM column is possible albeit with low detection efficiency. Therefore, for biological imaging, he proposed an alternative approach: a thin tissue section is deposited directly on a scintillator, to detect the transmitted electron signal with an optical detection system [26]. Zuidema [27] further researched and developed this optical detection (OSTEM) scheme for thin biological samples. He showed that it provides better image contrast than backscatter electron detection due to the high detection efficiency and better signal-to-noise values at short dwell times. He then designed the hardware and optical detection system for a mSEM dedicated to transmission imaging of thin biological samples.

1.4 FAST-EM

During the project of Zuidema, a consortium of TU Delft and three industry partners was started to realize a commercial mSEM system, FAST-EM. In this consortium, Thermo Fisher Scientific was responsible for the electron optics and MBS design, Technolution Advance for the electronics and signal processing and Delmic for the optical detection system, stage design and the final system integration. Starting from the initial idea to retrofit an existing SEM single column and convert it into a mSEM, two prototype systems (Functional Model Alpha and Beta) were developed. These models provided useful insights on the best scanning strategy, stage design, detector module layout and light optics. For the final prototype design, a TFS Nicole column (Apreo 2 SEM) was adopted, since the column on which all earlier prototypes were based (FEI Nova NanoSEM) was put out of production. With a variable landing energy of 2-10 keV, as found to be the optimal range for transmission imaging [28], the amount of beams was reduced to 64 with a pitch size of 3.2 µm.

FAST-EM entered the early adopter stage at the beginning of 2022. It was first acquired by the research groups of Ben Giepmans at University Medical Center Groningen and Jacob Hoogenboom at Imaging Physics, TU Delft, who both contributed to its development. The system was initially released with fixed settings for the landing energy, magnification and beam current, but allowed for a variable dwell time setting and had largely automated calibrations and acquisition. A graphical user interface for the microscopy software control was still under active development, but basic functionality was in place to start producing large-scale datasets.

1.5 Applying FAST-EM in large-scale biological EM

Up to this point, research has focused on the technological development of FAST-EM, with preliminary demonstrations of its biological applications restricted to 2D images of tissue. For any new microscopy technique with applications in biology, it is essential to prepare biological samples in such a way that guarantees representation of their native state. There may be different limitations or requirements on the sample and on the way contrast is obtained. Developing and benchmarking of novel microscopy techniques and sharing workflows for biological applications are thus essential steps. In this thesis, the benchmarking of FAST-EM as a tool for large-scale biological EM and subsequent adoption in a workflow for vEM is described.

There can be a significant time gap between the conception of a new technique and its wider adoption by the research community. The development of a dedicated mSEM and optical detection system for high-throughput imaging of thin biological samples spanned a time period of roughly 10 years. In the same time, multiple complementary approaches for faster electron microscopy have been introduced. Particularly in the field of vEM, there have been significant technological developments to circumvent the throughput bottleneck of EMs, and workflows have been developed to demonstrate their applications on large sample sizes. These developments are reviewed in Chapter 2. The preparation and imaging of millimeter-sized specimens with electron microscopy techniques is especially challenging and may result in additional artifacts. What is more, these vEM techniques typically yield very large datasets, which significantly complicates analysis.

OSTEM detection has been shown to produce high contrast images for thin biological sections [29]. However, an extensive characterization of this detection technique is still lacking, especially its performance in the context of other detection techniques commonly used in large-scale EM. Chapter 3 therefore covers a characterization study of OSTEM detection and comparison and subsequent benchmarking to other established SEM detection techniques for the imaging of thin biological samples.

The adoption of FAST-EM as a tool for vEM requires an extensive investigation into the compatibility of FAST-EM and OSTEM detection with EM sample preparation protocols, acquisition strategies and image processing tools. In fact, it necessitates the development and implementation of a novel workflow for vEM. For EM sample preparation alone, there exists many different approaches and protocols each tailored to specific research questions and samples. Similarly, the toolkit for image processing and analysis of vEM datasets is already comprehensive and expanding at a steady rate. To stay in line with addressing the acquisition speed bottleneck in large scale imaging, the research is focused on implementing a workflow for vEM with FAST-EM based on an established technique, array tomography (AT). Conventional AT covers the imaging of serial thin sections, arranged in ribbons, of resin-embedded biological samples collected on a solid substrate (for FAST-EM, the scintillator is the substrate). The implementation of this workflow, along with the development of software for 3D reconstructions and analysis of FAST-EM AT datasets, is described in Chapter 4.

The characterization and benchmarking of FAST-EM and OSTEM detection also necessitates a thorough description of its pitfalls and artifacts. Zuidema documented some considerations for imaging thin sections of heavy metal stained, resin-embedded tissue, but the implications for large scale imaging have not been fully explored. In particular, the combination of biological sample preparation, scintillator-based solid substrates and single-beam and multibeam OSTEM detection is accompanied by several types of image artifacts that would otherwise not appear in other detection techniques. These artifacts can severely affect the success rate of AT experiments and complicate the image interpretation. Chapter 5 describes these artifacts and their effect on the OSTEM image quality. The artifacts and their origin may not be new of nature. However, how they appear in FAST-EM and OSTEM detection is an important research question that needs to be addressed to find ways to mitigate artifacts and facilitate image interpretation.

2

How innovations in methodology offer new prospects for volume electron microscopy

Detailed knowledge of biological structure has been key in understanding biology at several levels of organization, from organs to cells and proteins. Volume electron microscopy (vEM) provides high resolution 3D structural information about tissues on the nanometer scale. However, the throughput rate of conventional electron microscopes has limited the volume size and number of samples that can be imaged. Recent improvements in methodology are currently driving a revolution in vEM, making possible the structural imaging of whole organs and small organisms. In turn, these recent developments in image acquisition have created or stressed bottlenecks in other parts of the pipeline, like sample preparation, image analysis and data management. While the progress in image analysis is stunning due to the advent of automatic segmentation and server-based annotation tools, several challenges remain. Here we discuss recent trends in vEM, emerging methods for increasing throughput and implications for sample preparation, image analysis and data management.

This chapter has been published as: Arent J Kievits, Ryan Lane, Elizabeth C Carroll, and Jacob P Hoogenboom. "How innovations in methodology offer new prospects for volume electron microscopy". *Journal of microscopy* 287.3 (2022), pp. 114–137.

2.1 Introduction

Method development is a key factor in accelerating biological discovery. Advances in imaging techniques have fulfilled the desire of biologists to unravel the structure and function of biological systems across a wide spectrum of spatial scales. Electron microscopy (EM) is especially suited for this goal. With its high resolving power, the structure of tissues can be revealed down to the nanoscale. This makes it a useful tool for determining the wiring patterns of neurons [30], but also the detailed investigation of cell organelles [3], such as microtubules [4], mitochondria [31], ER [32] and extracellular vesicles [33].

The imaging of tissues with EM has a long history of development. The protocols and techniques used to prepare the specimen, initially intended for transmission electron microscopy (TEM), were developed in the early 1940s [34]. Serial section transmission electron microscopy (ssTEM) was introduced in the 1950s to provide a three-dimensional context of the tissue [35, 36]. More than half a century later, resin-embedded tissue samples are still cut into thin sections (albeit much thinner than before) and subsequently imaged with TEM [37, 38]. Until the introduction of computer-assisted methods in the 1970s, 3D reconstructions of tissue had to be done entirely by hand. For this reason, and because of the extensive manual labour involved in cutting and handling sections, ssTEM applications remained quite limited [37].

Innovations in the 2000s led to more automated and routine EM techniques for 3D reconstructions of tissue (Table 2.1), thereby establishing a new research field: volume electron microscopy (vEM) [39]. As an alternative to ssTEM, serial section electron tomography (ET) was introduced [40, 41, 42], in which a tomographic reconstruction of each serial section is made. Scanning electron microscopes (SEM) allowed for the cutting device to be integrated into the microscope, leading to serial blockface scanning electron microscopy (SBF-SEM) [43] and focused-ion beam scanning electron microscopy (FIB-SEM) [44, 45]. While both offer better axial resolution than ssTEM, they lack the high lateral resolution of TEM and destroy the sample during acquisition. Combining serial sectioning with SEM led to the development of serial section SEM, also known as array tomography (AT) [46, 47]. Additionally, Automated Tape-collecting Lathe UltraMicrotome (ATLUM, later combined into ATUM-SEM) allows consistent collection and handling of thousands of serial sections [48, 49].

vEM techniques have been successfully applied in various fields, such as connectomics research (i.e. mapping the connections between neurons) [30], virology [53, 54] and cell biology [55]. However, when considering the imaging of 'large' volumes (>10^6 μm^3), the aforementioned EM approaches quickly run into their limits as the throughput of modern electron microscopes remains low. The imaging and reconstruction of larger volumes can take up to several months or years in some cases [7, 8, 56, 57]. Additional challenges include the increased risk of acquisition errors and loss of material during long acquisitions, generation of very large data sets (hundreds of terabytes) and enormous manual annotation efforts [58, 59]. As a consequence, every vEM study is a trade off between resolution, acquisition speed, long term system stability and the effort needed in annotation.

Despite these challenges, new light is shining on the vEM field. Powerful electron microscopes with unrivalled acquisition speeds have recently made their entrance [60, 26]. At the same time, the throughput of existing methods has increased significantly by advancements in software and hardware [61, 62, 63, 8, 57, 64]. Years of imaging with

Table 2.1: vEM methodology. The development and application of these methods is reviewed in [39, 50, 51, 52].
*: 2 nm for < 300 nm sections, 5 - 10 nm up to 1 µm

		Typical resolution			
Methodology	**Description**	**x, y [nm]**	**z [nm]**	**Volume [µm^3]**	**Reference**
Serial Section Transmission Electron Microscopy (**ssTEM**)	(Serial) sections are collected, (manually) transferred to a support grid and imaged with tranmission electron microscopy.	4	50	10^6 - 10^9	[37, 38]
Electron Tomography (**ET**)	Tomographic reconstruction of section by recording at multiple tilt angles. Limited to small volumes.	2 - 10*	2 - 10*	10^2 - 10^3	[41, 42]
Serial Blockface Scanning Electron Microscopy (**SBF-SEM**)	Automated method with microtome inside vacuum chamber. Iteratively a thin layer of material is removed from tissue the block, after which the surface of the block is imaged and the scattered electrons are recorded.	10	30	10^5 - 10^7	[43]
Focused Ion Beam Scanning Electron Microscopy (**FIB-SEM**)	Very thin layer of material is iteratively removed by a focused gallium ion beam, after which the top of the block is imaged.	5	5	10^2 - 10^5	[44, 45]
Automated Tape-Collecting Ultramicrotome SEM (**ATUM-SEM**)	Serial sections are automatically cut by an microtome and collected on tape by a computer-controlled reel-to-reel conveyer belt mechanism. Sections are consecutively imaged in SEM.	Flexible	60	10^7 - $10^1$0	[48, 49]
Array Tomography (**AT**)	Ribbons of serial sections are collected on solid surface (silicon wafer, glass) and imaged consecutively in an SEM.	4	30, 60	10^4 - 10^6	[46, 47]

conventional systems could now in principle be reduced to a few weeks. In this review, we analyze trends in vEM and focus on the specific improvements in methodology that relieve the bottleneck in throughput of electron microscopes. We then discuss the implications of these developments for sample preparation, image analysis and data management respectively.

2.2 Trends in volume electron microscopy

To distill general trends in vEM, we summarized relevant statistics from a pool of over 200 EM volumes from 115 unique studies (Figure 2.1) conducted between 2009-2021, including those covered in earlier reviews [39, 50, 65]. It is inevitable that certain statistics are missing from a number of studies as certain data set parameters such as volume size, voxel resolution and data set size are not consistently reported and have yet to be standardized (connectomics studies being an exception [65]).

We searched and grouped studies based on the used techniques: serial section transmission electron microscopy (ssTEM), serial blockface scanning electron microscopy (SBF-SEM), focused ion beam scanning electron microscopy (FIB-SEM) or automated tape-collecting ultramicrotome SEM (ATUM-SEM). The latter can be considered as a subset of array tomography, but whereas array tomography is also frequently associated with light microscopy, ATUM-SEM is a more dedicated vEM technique. Certain application regimes can be distinguished (Figure 2.1A-B). FIB-SEM is clearly in the high resolution but low volume regime, whereas ssTEM studies typically target large volumes with high lateral

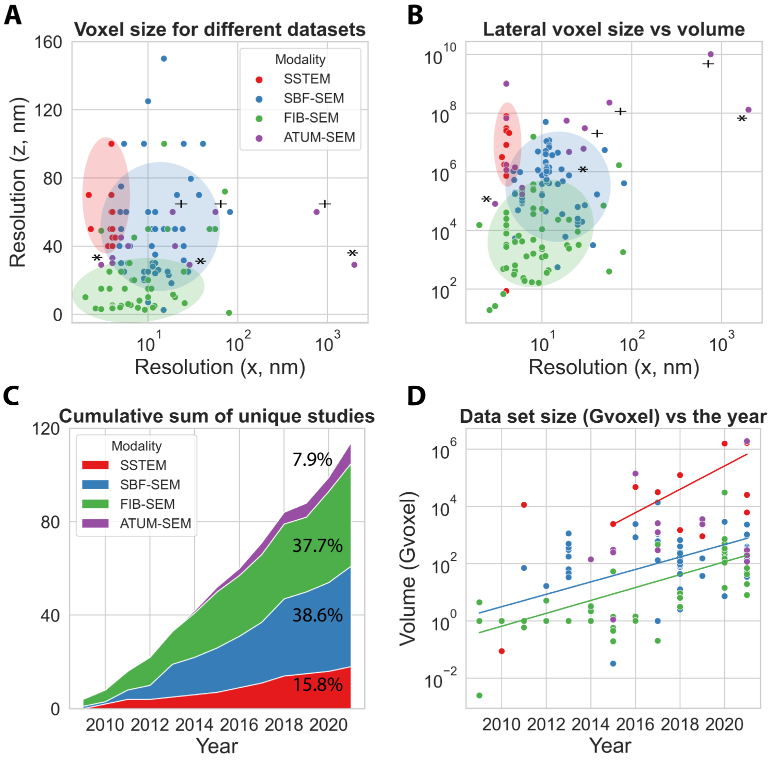

Figure 2.1: Overview of VEM studies from 2009-2021 reporting voxel resolution, method, volume and data set size. (a) Voxel size (x vs z) and (b) volume size for all data sets. Ellipses indicate application regimes. (c) Cumulative sum of studies per method. (d) Increase in dataset size per year. All data points represent a single data set, except those marked by $*$ and $+$ which are targeted re-acquisitions from [66] and [7] respectively.

resolution - suitable for use in connectomics. ATUM-SEM and ssTEM show great flexibility in the volume size and resolution, because they allow re-imaging of parts of the sample with different settings. SBF-SEM is a 'mid-range' method, covering a volume range from roughly 10^4 to 10^7 µm^3. Additionally, the number of vEM studies is increasing at a steady rate. The majority of studies has been conducted using SBF-SEM or FIB-SEM (Figure 2.1C). Although the number of studies per year varies quite a bit, there is a clear trend towards bigger data sets (Figure 2.1D).

The push towards larger volumes can be explained by connectomics research. Scientists have fully reconstructed the nervous systems and determined the connectomes of small organisms, and partially in bigger organisms (Table 2.2). From the smallest (*C. elegans* larval brain [67]) to the largest volume (Mouse visual cortex [68]) at full resolution, the size difference is more than five orders of magnitude. While connectomics research can be considered a driver for innovation in the field, the application of vEM is linked to several other research fields [69, 70, 71, 72, 73, 54]. We found over 110 distinct applications in 23 different organisms, including animals (and their larval stages), plants, bacteria and cell lines (Table A1). Some studies feature reconstructions of single-cell organisms and small organisms such as the budding yeast *S. cerevisiae* [74], parasite *Trypanosoma brucei* [75] or the ringed worm *Platynereis dumerilii* at 6 days post-fertilization [76]. Some of the larger samples are intersegmental vessels and dorsal-lateral lanastomotic vessels in zebrafish embyos [77] (FIB-SEM), root tips of the barrelclover *Medicago truncatula* [50] (SBF-SEM), human and mouse fibrous connective tissue [78] (SBF-SEM) and mouse liver tissue [79] (FIB-SEM).

Table 2.2: Relevant imaged volumes in connectomics research. L1, L2 and L3 are larval stages. CNS: Central nervous system. Hermaphr.: hermaphrodite. ATUM-SEM is further abbreviated to 'ssSEM'.

Species	**Stage**	**Tissue**	**vEM method**	**Analyzed**	**Volume size (µm^3)**	**Dataset size (TB)**	**Ref.**
C. elegans (Roundworm)	L3	Hermaphr. brain	SSTEM	Fully	15707	-	[67]
	L2	Hermaphr. brain	ssSEM	Fully	15351	-	[67]
	L1	Hermaphr. brain	ssSEM	Fully	5148	-	[67]
	L1	Hermaphr. brain	ssTEM	Fully	4251	-	[67]
	L1	Hermaphr. brain	ATUM-SEM	Fully	2989	-	[67]
	L1	Hermaphr. brain	ATUM-SEM	Fully	4536	-	[67]
	Adult	CNS	ssTEM	Fully	-	-	[5]
	Adult	Brain	ssTEM	Fully	52382	-	[67]
	Adult	Hermaphr. brain	ATUM-SEM	Fully	73850	-	[67]
	Adult	Male CNS	ssTEM	Fully	724776	-	[80]
C. intestinalis (Sea squirt)	Larva	CNS	SSTEM	Fully	-	-	[6]
D. melanogaster (Fruit fly)	Larva	CNS	SSTEM	Partly	1755837	-	[81]
	Adult	Central brain	FIB-SEM	Fully	15625000	26	[56]
	Adult	Full brain	ssTEM	Partly	79150500	106	[8, 82]
	Adult	Mushroom body	FIB-SEM	Fully	240000	3.8	[83]
	Adult	Olfactory system	ssTEM	Partly	250000000	50	[84]
	Adult	Ventral nerve cord	ssTEM	Partly	21000000	172.6	[64]
D. rerio (Zebrafish)	Larva	Brain	ATUM-SEM	Partly	10200000000	4.4	[7]
	Larva	Hindbrain	ATUM-SEM	Partly	1404480	-	[85]
	Adult	Spinal segment	SBF-SEM	Fully	11716726	-	[86]
H. Sapiens (Human)	Adult	Cerebral cortex	ATUM-SEM	Partly	1000000000	1400	[68]
M. musculus (Mouse)	Adult	Cochlea	SBF-SEM	Partly	6841300	0.194	[87]
	Adult	Cochlea	SBF-SEM	Partly	7796872	-	[87]
	Adult	Cortex layer 4	SBF-SEM	Fully	542510	-	[59]
	Adult	Neo cortex	ssTEM	-	1000000000	2000	[57]
	Adult	Neo cortex	ATUM-SEM	Partly	130000000	0.3	[66]
	Adult	Somatosensory cortex	ATUM-SEM	Partly	30500000	0.14	[88]
	Adult	Visual cortex	ssTEM	partly	30375000	100	[89]
	Adult	Visual cortex	ssTEM	Partly	8190000	-	[62]
	Adult	Visual cortex	ssTEM	Partly	1049022720	2000	[72]
	Adult	Visual thalamus	ATUM-SEM	Partly	67200000	100	[90]

The number of volumes with high isotropic resolution is also increasing. Abnormalities in cell organelle structure and function are implicated in the development of diseases, which can be studied in detail with FIB-SEM. vEM studies with FIB-SEM have resulted in high resolution 3D reconstructions including (but not limited to) HeLa cells, T-cells and macrophages [70, 3, 91], cancer cells [92], mouse primary beta cells [4] and COS-7 cells [93]. Moreover, studies have been performed on human cardiac telocytes [94], mouse liver tissue [79] and lung alveolar epithelium [95]. Studies of abnormal ultrastructure are emerging, including breast carcinoma and pancreatic adenocarcinoma [73].

In short, vEM applications have expanded well beyond the scope of connectomics, and the various techniques can be demarcated into distinct application regimes. Data sets are increasing in size and becoming more diverse. We will show later that some trends can be attributed to specific developments in hardware (Section 2.3), while others may be a result of the general increase in popularity of vEM and access to better equipment. We will now layout the new developments in methodology which have contributed to some of the trends that are described here.

2.3 Imaging of larger volumes

A major feat in vEM would be to routinely image volumes larger than 1 mm^3 at nanometer resolution in a few months. Achieving this is not only a matter of improving speed; instrumentation must be able to robustly image thousands of tissue sections or slices for extended periods with minimal intervention. Therefore, instrumentation development has focused not only on increasing imaging speed, but also robustness and automation. New developments can roughly be divided into four groups: (1) parallelization by multiple beams, (2) parallelization by multiple cameras, (3) parallel processing in block-face imaging and (4) re-imaging of volumes at different resolution scales (Figure 2.2).

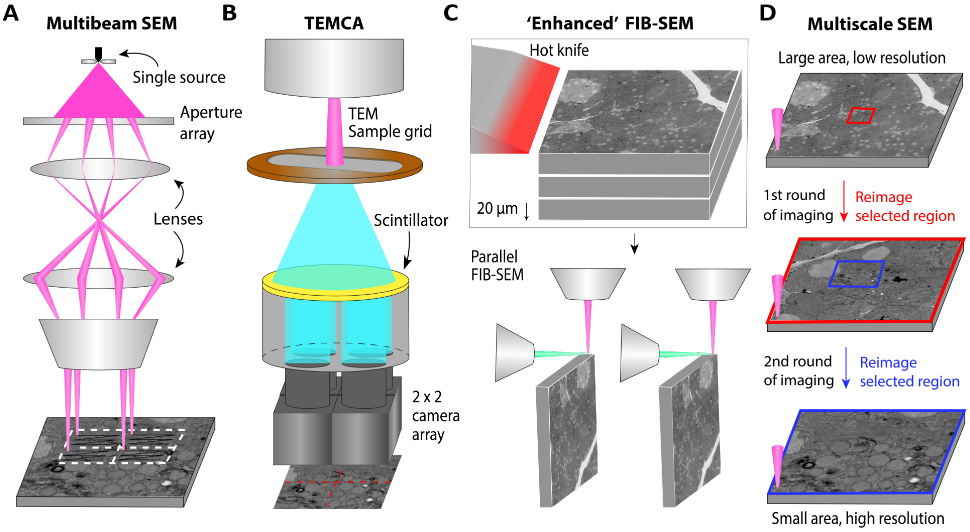

Figure 2.2: Four different methods for scaling up vEM studies: (a) Multibeam electron microscopy. Throughput is increased by using multiple beams in parallel. (b) TEMCA [62] and AutoTEM [57] principle. Throughput increase by multiple parallel cameras to enlarge the field of view of the microscope. (c) 'Enhanced FIB-SEM': ultrathick sectioning [61] is applied to a sample that is too thick to be handled by a single FIB-SEM. Throughput increase is achieved by higher system stability and using multiple FIB-SEMs in parallel. (d) Single-beam multiscale EM. 'Increased' throughput by scanning a large area at low magnification followed by multiple rounds of targeted acquisition at higher resolution.

2.3.1 Multiple scanning beams in parallel

The imaging speed in vEM is limited by the minimum signal-to-noise ratio (SNR) needed to make biological features sufficiently visible against a noisy background. The SNR is influenced by the exposure time, beam current, sample contrast and detection efficiency [60]. In order to achieve faster imaging, it seems straightforward to increase the beam current. However, this leads to lower resolution due to increased coulomb interactions and can go at the cost of sample charging, inducing sample drift and artifacts. A workaround would be to use multiple beams in parallel. This idea has led to the development of multibeam scanning electron microscopy (mSEM) [60, 26]. A mSEM scans the sample simultaneously with an array of beamlets produced by a single electron source, increasing the acquisition speed proportionally to the number of beamlets with theoretically no compromise on resolution compared to single-beam SEM. Multiple concepts have been developed for mSEM with different source and column configurations, beam array sizes and detector systems [96, 60, 97, 26].

The first commercially available mSEM (MultiSEM) was released in 2015 [60, 98], producing 61 or 91 beams in a hexagonal pattern (Figure 2.3A). The primary beams originate from a single source and go through a single column, where they are separated from secondary electron signals by a magnetic beam splitter. Each secondary electron signal is lead to a dedicated secondary electron detector (Figure 2.3A). The number of beams can be increased without changing the primary design; a 331 beam version has subsequently been developed [99], though it is not yet commercially available.

A single-source 196-beam mSEM was developed at Delft University of Technology [96]. This model employs transmission electron detection instead of secondary electron detection. The sample is placed on a luminescent material (scintillator) coated with a thin conductive layer which converts the electrons to photons. The light beams are then imaged onto a detector array [26, 29] (Figure 2.3B). A dedicated 64-beam mSEM system (FAST-EM) using this technology has recently been commercialized.

While mSEM is not yet widely applied in vEM, the first study results are impressive. A large-scale (2D) study of mouse and marmoset brain tissue was performed [100]. Another study revealed for the first time the complex structure of the chicken retina [101]. The latest result is a 1.4 petabyte data set of human cerebral cortex acquired in 326 days [68], which was fully segmented using automated methods discussed later (Section 2.5.3). These pioneering studies indicate great potential.

2.3.2 Multiple cameras: TEMCA and AutoTEM

Transmission electron microscopy is inherently parallel compared to scanning electron microscopy. However, it is slowed down significantly by sample stage movement, detector readout time and sample grid replacement. TEM camera array (TEMCA) was developed to improve the throughput of transmission electron microscopes [62, 89]. The field of view of the TEM is increased by using a 2x2 array of high-speed CCD (charge-coupled device) cameras coupled to lenses, connected to an extended vacuum column. To further improve throughput, Zheng *et al.* [8] built two second generation TEMCA systems (TEMCA2), equipped with four CMOS cameras, a custom piezo-driven fast stage and an automated transport and positioning system, which allow unsupervised sample loading and imaging for extended periods. Together, these innovations allow 40× faster imaging than conven-

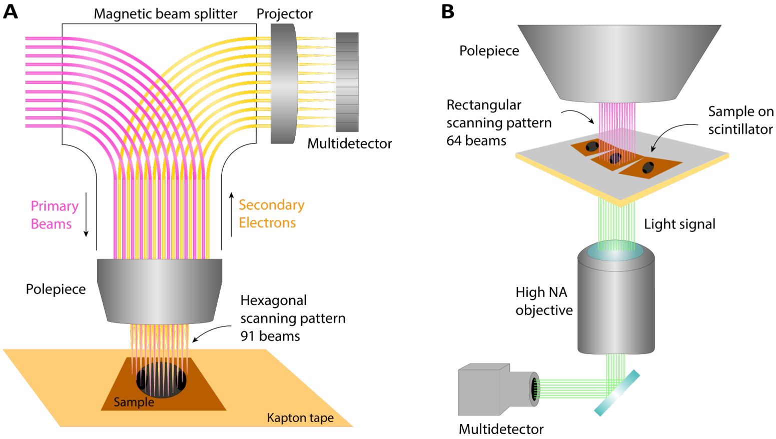

Figure 2.3: Different multibeam systems. (a) Zeiss MultiSEM [60], which makes use of secondary electron detection by a multidetector. The primary beams and detected electrons are separated by a magnetic beam splitter. (b) Delft Multibeam [26, 28]. Instead of secondary electron detection, this multibeam system detects transmitted electrons via conversion to a light signal by a scintillator located directly under the sample.

tional TEM. The TEMCA2 design was used to image a full adult fruit fly brain in 16 months [8].

The TEMCA2 has inspired the development of a further automated TEM system, autoTEM [57]. AutoTEM consists of 6 parallel TEMCA-inspired systems with a summed burst acquisition rate of 3 Gpixel/s and a net rate of 600 Mpixel/s. A new nano-positioning sample stage offers fast montaging of large areas [102, 64]. The sections are loaded onto a new aluminum-coated polyimide tape with regularly spaced TEM-grid-resembling holes (GridTape [64]), which enables section collection with ATUM. The implementation of a new reel-to-reel tape translation system allows loading and selection of 5500 sections per vacuum cycle. With AutoTEM, two 1 mm^3 volumes of mouse neocortex and primary visual cortex were imaged in about 6 months, resulting in two petabyte datasets [57, 72]. Additionally, a TEMCA system upgraded with GridTape was used to reconstruct the ventral nerve cord of a female fruit fly, resulting in a 172.6 terabyte data set [64].

2.3.3 Parallel processing in block-face imaging

While serial block-face methods are used in the majority of vEM studies (Figure 2.1C), increasing their throughput is not trivial. So far, block-face methods remain incompatible with mSEM. While acquisition in SBF-SEM is highly automated, the samples are prone to charging and sensitive to beam dose. Solutions to these problems are described later (Section 2.4). An even bigger challenge is increasing the low throughput of FIB-SEM, which is a result of slow FIB-milling speeds and limited robustness of FIB-SEM systems.

Parallel ’Enhanced’ FIB-SEM

To make FIB-SEM systems more suitable for large-scale vEM, Xu *et al.* [63] developed ’Enhanced FIB-SEM’. Enhanced FIB-SEM expands the scope of FIB-SEM from 1000 μm^3 to 3 x 10^7 μm^3; four orders of magnitude. FIB-milling limits the sample thickness to about 100 µm in the milling direction because it introduces streaks and waves of thickness variation. A solution was found in smooth 'ultrathick' partitioning of tissue volumes [61]. Resin embedded tissue is cut into multiple chunks of 20 µm with a hot ultrasonic vibrating diamond knife to reduce distortions and slips. The chunks can then be imaged separately and stitched together. Additionally, signal detection is improved by a small positive stage bias that filters out secondary electrons, allowing efficient backscatter detection by an in-column detector. The working distance is reduced by repositioning the FIB column to be 90 degrees from the SEM column. Lastly, a special closed loop control system is used to maintain ion beam stability and allow seamless restarts. Two 'enhanced' FIB-SEMs were employed in a study that reconstructed the connectome of the fruit fly central brain [56].

Alternative milling approaches

Other milling approaches could potentially offer higher throughput than conventional gallium ion FIB, including gas cluster ion beam (GCIB) [103], broad ion beam (BIB) [104] and plasma focused ion beam (PFIB) milling [105]. In GCIB-SEM, 500 nm - 1 µm thick sections are collected from the sample. These sections are pre-irradiated with the SEM to reduce charging, followed by milling at 30 degrees with clusters of low energy argon ions. Volumes with 10 nm isotropic resolution were acquired, but full integration with high-throughput SEM has yet to be demonstrated. With BIB, large areas (up to several mm) can be milled while simultaneously offering a sputter rate up to five times higher than in gallium ion FIB [106]. Milling and imaging of liver and mouse brain tissue has been demonstrated with an integrated BIB-SEM system, although not with high isotropic resolution as in FIB-SEM. Xenon ion PFIB offers low damage milling compared to gallium FIB with 20-60x faster rates [105], but has not been widely adopted for biological samples. Oxygen has also been proposed as an alternative ion species with greater resin compatibility and similar potential gains in throughput [107].

2.3.4 Targeted reimaging with multiscale EM

Unlike block-face methods, serial sectioning methods like ssTEM and ATUM-SEM allow re-imaging of tissue sections. This has inspired some researchers to use a multi-resolution approach when imaging large volumes with ATUM-SEM [66, 7], to limit acquisition time. After recording the complete volume at low magnification, targeted regions of interest can be re-imaged at higher magnification to reveal smaller features. In connectomics, this is convenient because most neuronal branches can be traced at lower resolutions while only some parts are needed in high resolution for completion [90]. Moreover, the different datasets can be registered and combined into a multi-resolution dataset.

Another multi-resolution approach combines ATUM with targeted high isotropic resolution FIB-SEM, a new method called 'multiscale ATUM-FIB microscopy' [108]. In ATUM-FIB, serial sectioning of tissue into 'semithick' 2-10 µm sections is done first to create a library by attaching them onto glass slides that can be imaged with light microscopy. Then, they are remounted onto silicon wafers for serial section SEM to identify regions of interest to target with high resolution FIB-SEM.

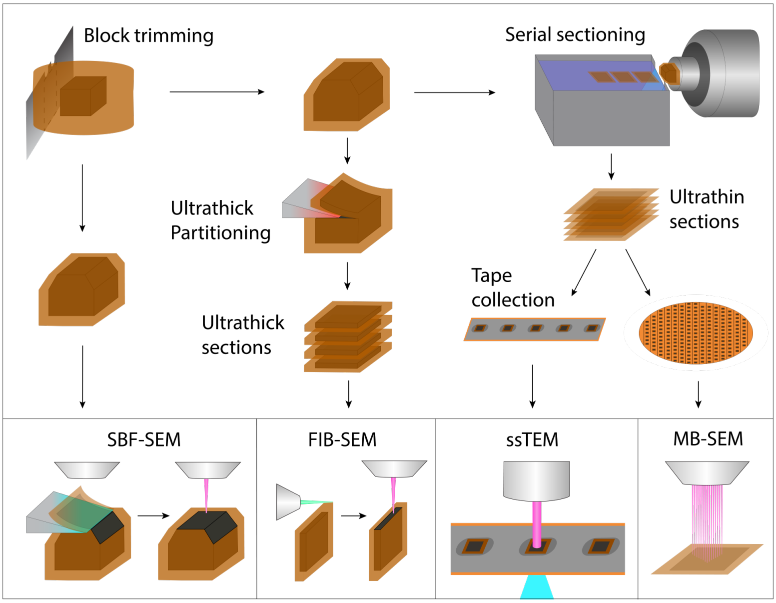

Figure 2.4: Sample preparation steps for high-throughput vEM. Next to improvements in *en bloc* staining, ultrathick partitioning was introduced in FIB-SEM and tape collection in ssTEM. Figure not to scale.

2.4 Sample preparation for large volumes

The success of a vEM study is ultimately determined by the quality of sample preparation. It is inherently difficult to prepare biological samples for electron microscopy; they should be compatible with staining and residing in vacuum, have sufficient and homogeneous contrast and be resistant to sectioning and beam irradiation. While sample preparation protocols are typically designed for a specific target species or tissue type, they follow roughly the same steps: (1) fixation with aldehydes, (2) staining with heavy metals such as osmium, uranium and lead, (3) tissue dehydration and (4) resin embedding, followed by sectioning. The whole procedure, including sectioning, can take up to a few weeks per sample [57, 72]. With acquisition times of large volumes being significantly reduced by emerging new methods (Section 2.3), further optimization of sample preparation protocols with respect to throughput becomes increasingly important. We describe next the implications of the throughput increase in acquisition on sample preparation.

2.4.1 Approaches in fixation and staining

Sample preparation protocols have been modified to allow for higher throughput acquisition methods (Figure 2.4) as well as for homogeneity of fixation and staining for larger than before sample volumes. To provide homogeneous preservation of the tissue, it is either dissected before fixation [84, 8, 56], or perfused with a fixative solution before dissection [66, 89, 90, 7, 109, 59, 57]. To further promote diffusion of the fixative into the sample, the surrounding skin can be removed [7]. Fixation is typically followed by *en bloc* staining, in which the sample is submerged into one or more solutions of (different) heavy metal compounds to increase electron scattering. In traditional serial section TEM, samples are typically treated twice: first *en bloc*, then by *post staining* the ultrathin sections to enhance the contrast. However, post-staining is laborious, prone to contamination, and incompatible with block-face techniques.

Hence, vEM sample preparation protocols have been designed to optimize *en bloc* staining. The traditional osmium-thiocarbohydrazide-osmium (OTO) protocol [110], in which thiocarbohydrazide acts as a bridging agent for osmium tetraoxide to crosslink and stain cell membranes, typically leads to inhomogeneous staining for larger volumes. By addition of potassium ferri- or ferrocyanide, the osmium can be reduced to make it more reactive (reduced OTO or rOTO [111]). While this improves contrast and thereby allows for lower dwell time, it still has a limited penetration depth (~200 µm) and weakens large tissue samples due to the formation of nitrogen bubbles. The OTO protocol was therefore modified further by separating the osmium and ferrocyanide treatment steps [112]. This allows the osmium to penetrate deeply into the tissue, after which it is reduced to allow for deeper staining. A variant on this protocol adds formamide during the reducing osmium step and replaces thiocarbohydrazide by pyrogallol, which prevents nitrogen bubble formation [113]. This protocol was further optimized to reduce the long incubation times [114] thus allowing both homogeneous, strong fixation and staining as well as faster sample preparation.

2.4.2 Sectioning of large volumes

Three out of four emerging vEM techniques discussed in Section 2.2 rely on serial sectioning, motivating the need for reliable sectioning approaches. Cutting and collecting (thousands of) ultrathin serial sections is a delicate process; many factors affect the consistency and continuity. An inherent issue is that interruptions are needed to resharpen or replace the knife, which impair sectioning quality as the knife needs to be repositioned. A closed-loop repositioning system as introduced in FIB-SEM may offer a solution. Another issue is section collection. Multiple tools have been developed that simplify the handling and collection of moderate amounts of sections [115, 116, 117], but for larger amounts automated collection (ATUM) is currently the only viable option. The collection tape of ATUM has a low packing density (~200 sections per meter) and needs to be carbon-coated for conductivity. Intrinsically conductive alternatives such as carbon-nanotube tape [118], on the contrary, need plasma treatment for hydrophilization and manual grounding. In order to increase the packing density of sections, Templier [119] introduced MagC, in which the tissue block is glued to a magnetic resin, which allows magnetic collection of the sections directly onto wafers.

2.4.3 Charge-compensation and artifact reduction

Artifacts created during sample preparation and acquisition increase the difficulty of reconstructing volumes with automated image processing methods [59, 56, 68]. There are several ways in which these artifacts can be reduced. One way is focal charge compensation, in which surface charges are neutralized by local injection and ionization of nitrogen gas onto the sample [120]. Additionally, the conductivity can be increased by coating the sample with a thin metallic film prior to each cycle of imaging [121]. The embedding material can also be made more conductive, either with a metallic particle filler [122] or adding carbon powder [123, 124]. New types of resins can also offer higher contrast with low stain concentrations, offering a way to reduce artifacts introduced by staining [125]. Lastly, the sample can be embedded within another biological sample [7] to improve stability of the tissue block and prevent shrinkage and deformation.

2.5 Image processing and analysis in vEM

Image processing and analysis of vEM data sets are nontrivial tasks due to their size and complex nature. Roughly speaking, the steps in image processing are intensity normalization, 2D stitching and 3D alignment, while image analysis concerns the annotation (labeling individual biological features in the data set) and segmentation (assigning every pixel or voxel to a class) of the reconstructed volume to extract biological information (Figure 2.5). The computer algorithms that handle these tasks have to overcome difficulties such as variable intensity and contrast, sample drift, missing or low-quality data, and imaging artifacts introduced by sample preparation, sectioning (shear, distortion), pickup, inhomogeneous staining, and beam damage. The throughput increase also poses additional challenges for image analysis. Manual segmentation of volumes, already a time-consuming process for small data sets, becomes impractical for large data sets. We will illustrate the steps in image processing and analysis while discussing the state of the art approaches and methods.

2.5.1 Stitching of large FOVs and 3D alignment

When a region of interest (ROI) is larger than the field-of-view (FOV) of the microscope at the desired magnification, multiple FOVs must be acquired with a small overlap and digitally stitched together to reconstruct the whole ROI (commonly referred to as a *montage* or *mosaic*). There are multiple algorithms for stitching which generally work for all EM techniques considered here. The simplest in terms of computational complexity is phase correlation, which computes the translation between two overlapping image tiles based on the normalized cross-correlation [126]. However, phase correlation does not take into account affine transformations and only allows for local optimization. A more robust approach is to find local point-pair correspondences between images with a feature detection algorithm, such as the scale-invariant feature transform (SIFT) [127] or speeded up robust features (SURF) [128]. Both algorithms use scale-space representations of images - consisting of increasingly downsampled versions of the image - to find scale-invariant features. Corresponding point-pair matches are selected using robust sampling methods (RANSAC) [129] and from these the affine transformations are determined to generate a globally optimized alignment.

The same algorithms can be used to align individual mosaics in 3D. First, each mosaic is downsampled and roughly aligned to its neighboring layers. This is then refined by extracting and matching point-pair correspondences between neighboring tiles in different layers. In serial block-face methods (FIB-SEM and SBF-SEM), only subtle refinement may be needed as the FOV is inherently highly similar between adjacent slices. Alignment of ssTEM and ATUM-SEM is more complicated as it requires significant corrections for rotation and non-linear distortion compared to block-face data sets.

There are several dedicated software packages for stitching and 3D alignment, includ-

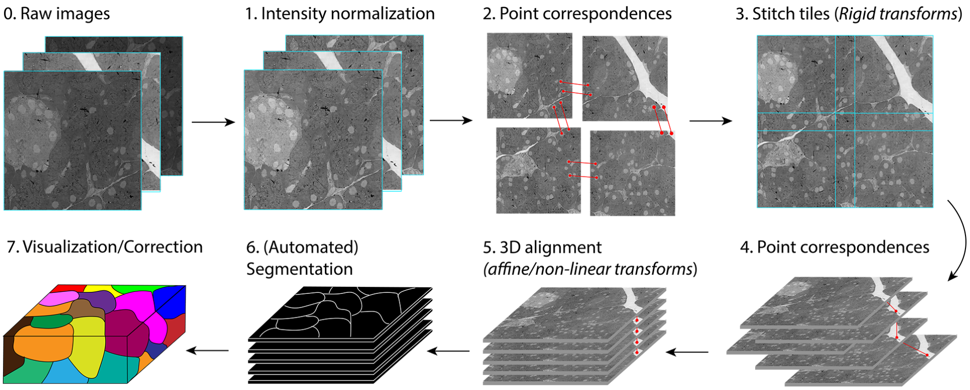

Figure 2.5: Image analysis workflow. First, the images are normalized. Next, images that belong to one section are stitched with help of point-pair matches and transformations. Similarly, the composite images of the sections are 3D aligned. When the 3D volume has been solved, the segmentation can be performed (automatically). Segmentation is followed by annotation and visualization. The data can then be interpreted and analyzed.

ing AlignTK [62, 89], NCR tools [130], StackReg [131] and Big Feature Aligner (BigFeta) [132]. Popular tools that can perform EM image registration are TrakEM2 [133] – implemented in Fiji (ImageJ), popular among bioimage analysts - IMOD [134] and Microscopy Image Browser (MIB) [135]. Lastly, a novel approach was developed for multiscale EM alignment, known as signal whitening Fourier transform (SWiFT-IR) [136], in which modulated Fourier transform amplitudes produce more robust image matching.

2.5.2 Manual annotation and segmentation

After the volume is reconstructed, the next step is to extract biological information from the data. To quantify the morphology of tissues, cells and cell organelles, their 3D structure has to be annotated and segmented. Successful interpretation of biological EM images is time consuming and requires training in anatomy. It was recently estimated that it would take up to 60 years to manually segment each organelle in a single cell by hand [3]. Nevertheless, vEM studies still rely on manual or semi-automatic segmentation and annotation. Usually, only a fraction of the entire volume is annotated by hand (*sparse annotation*) to reduce the workload. These annotations can be used as training data for machine learning algorithms to process the whole volume in an automated fashion (Section 2.5.3).

Voxel painting and neuron tracing

The most straightforward method is inspecting and labeling voxels with the help of (web-based) software. These applications allow browsing through a volume and facilitate tracing of cells, membranes, cell organelles or other features of interest. Groups of voxels can be assigned a label with brush or bucket tools. Neurons are frequently annotated by a center-line tracing (*skeleton*). Software tools often support multiple approaches. To get better accuracy, tracings can be proofread by an additional annotator. In large connectomics studies, typically a team of multiple annotators performs the tracing and proofreading, with assistance of anatomy experts [58, 7, 8, 59]. The exact segmentation approach depends on the complexity of the tissue and which type of annotation is desired (sparse or dense).

Tracing, annotation and segmentation software

Annotation tools combine segmentation, annotation and visualization into one interface. A distinction can be made between commercial and open-source software. Examples of commercial software are Amira (Thermo Fisher Scientific), Imaris (Oxford Instruments) and Vision4D (Arivis), whereas often used open-source programs are the Collaborative Annotation Toolkit for Massive Amounts of Image Data (CATMAID) [137], KNOSSOS [138] and its web version WebKnossos [139], Volume Annotation and Segmentation Tool (VAST) [140] and earlier mentioned tools, TrakEM2 [133], IMOD [134] and MIB [135]. Another distinction can be made between offline and web-based tools. VAST, TrakEM2, IMOD and MIB are offline tools, while CATMAID and webKnossos retrieve image data and annotations hosted on a remote server and work with databases to manage annotations. It can be accessed anywhere (with an internet connection) and multiple annotators can simultaneously work on different parts of the volume. A comprehensive list comparing various features of all tools has been published elsewhere [141].

2.5.3 Automated segmentation

The last 10 years have seen an increased usage and improvement of automated segmentation, made possible by developments in machine and deep learning. The choice for machine and/or deep learning seems obvious. vEM datasets are significantly growing in size, rendering complete manual segmentation impossible. Traditional segmentation methods most often fail or generalize poorly, because EM images are often noisy and characterized by variations in contrast and texture as well as artifacts introduced during sample preparation or imaging. Additionally, tissue structure can be very complex, such as the dense wiring patterns found in neural tissue. It has been shown that data driven models can cope with complex segmentation problems—convolutional neural networks (CNNs), from the domain of deep learning, outperformed traditional segmentation methods more than a decade ago [142]. CNNs are very popular for image segmentation because they efficiently extract and combine information from different hierarchical levels in the image. Automated segmentation using deep learning has become the predominant strategy in two different domains: connectomics and cell biology.

Automated segmentation in connectomics

In connectomics, the interest lies mainly in cell boundary segmentation and synapse detection. Many of the new developments can be attributed to several crowd-sourcing competitions for automated segmentation in 2D and 3D; the International Symposium on Biomedical Imaging (ISBI) [143], 3D segmentation of neurites in EM images (SNEMI3D)[1] and circuit reconstruction from EM images (CREMI)[2] challenges. State-of-the-art cell boundary segmentation approaches are typically either based on the popular U-Net CNN architecture [144, 145] or variants thereof. Variants based on U-Net have achieved near-human or even super-human segmentation performance on neural EM data [146, 147, 148, 149, 150, 151].

---

[1] http://brainiac2.mit.edu/SNEMI3D/home

[2] https://cremi.org/

Alternatively, flood-filling networks have been employed to increase segmentation accuracy at the expense of higher computational costs [152, 153]. A comprehensive overview of these approaches and their implementation has been described elsewhere [154].

Synaptic relations can be used to infer connectivity between neurons. Machine learning algorithms are therefore employed to find synaptic relations between neurons by classifying each voxel as 'synaptic' or 'non-synaptic'. Classical machine learning algorithms such as the random forest classifier are used [155, 156], but also here CNNs are gaining popularity [157, 158, 159, 160, 161, 162, 163, 164]. In short, these methods try to predict candidate synapses and their directionality, while some also distinguish the pre- and postsynaptic neurons [154]. Recent efforts in automated synapse detection resulted in a reliable connectivity graph in the whole brain fruit fly data set [82].

Cell organelle segmentation

In cell biology, the interest lies in segmentation of cell organelles to enable quantification of their morphology, distribution and size. A clear motive for this work is evidence that links alterations of organelle structure to neurodegenerative diseases and cancer [31, 33, 32, 165]. The high axial resolution of SBF-SEM and especially FIB-SEM data allows for accurate segmentation of cell organelles. Due to the diversity of organelles and cell types as well as a lack of publicly available training data, automated organelle segmentation has not experienced the same surge as in connectomics, which has benefited from years of substantial manual annotation effort [166, 58, 167, 66, 8, 168]. Nonetheless, there has been successful pioneering work within different types of vEM data (Table 2.3). Similar to dense reconstructions of neural tissue, several studies have now demonstrated (fully) automated multi-class segmentation of organelles in single cells [4, 3].

Examples of important yet difficult segmentation problems in EM data include mitochondria, nuclei and vesicles. Mitochondria vary greatly in shape and size. This variation is not well represented in commonly used training data sets [169, 170]. Nuclei segmentation is a common segmentation problem, also in light microscopy. Vesicles come in many forms and sizes. Automated mitochondria segmentation has been applied to FIB-SEM [171, 31, 32, 172] and ATUM-SEM data [31, 32, 173]. Despite the lower axial resolution of ATUM-SEM, it is still possible to segment mitochondria. While it is possible to segment plasma and nuclear membranes with traditional segmentation algorithms, [174, 175], two different groups approached nuclear envelope and nuclei segmentation with U-Net variants [165, 73]. To deal with the limited availability of expert manual annotations, the authors either aggregated multiple volunteer annotations [165] or utilized sparse labeling techniques [73]. Automated vesicle segmentation was developed for insulin granules [176] and small extracellular vesicles [33].

Challenges with convolutional nets

There are several problems associated with CNN-based segmentation. Generally, the performance is best on datasets with high isotropic resolution and proper alignment (SBF-SEM, FIB-SEM) [153]. Performance on serial section EM data, which is characterized by anisotropic resolution and slight defects in the alignment, can be improved by encouraging topologically correct segmentations obtained from the affinity graphs [179, 151]. A second problem is that several methods do not generalize well outside of their particular source and tissues [180]. To cope with this, domain adaption techniques can be used that

Table 2.3: Summary of studies on automatic organelle segmentation with machine learning and/or deep learning. The organelles, EM technique and neural network architecture are indicated. *NE*: Nuclear Envelope. *ER*: Endoplasmic Reticulum. *MTs*: Microtubules. *PM*: Plasma Membrane.

Application	Organelle(s)	Technique	Network architecture	Ref.
HeLa cells	NE	SBF-SEM	U-Net	[165]
HeLa cells, Jurkat cells, Macrophages	Chromatin, ER, Endosomal membranes, Lysosome, MTs, Mito, NE, PM, Vesicle membrane	FIB-SEM	U-Net	[3]
Rat hippocampus, mouse cortex	Mitochondria, ER	ATUM-SEM, FIB-SEM	ResNet, Region proposal Net, Recursive Net, Mask R-CNN	[32]
Rat hippocampus, mouse cortex	Mitochondria	ATUM-SEM, FIB-SEM	ResNet	[31]
Mouse primary beta cells	MTs, Golgi, Centrioles, Insulin granules	FIB-SEM	U-Net, Random-forest classifier	[4]
HeLa cells	ER, Mitochondria, PM	FIB-SEM	U-Net, EfficientUnet	[177]
Mouse Hippocampus	Vesicles, nuclei, mitochondria, membranes	SBF-SEM	DeepEM3D	[178]
Human breast carcinoma	Nuclei, nucleoli	FIB-SEM	ResNet, U-Net	[73]
Mouse Hippocampus	Mitochondria	FIB-SEM	'Conventional' CNN	[171]
Mouse urinary bladder urothelial cells	Mitochondria, endolysosomes	FIB-SEM	HighRes3DNet	[172]
Rat and human cortex	Mitochondria	ATUM-mSEM	U-Net	[173]
Pancreatic beta cells	Insulin granules	FIB-SEM	Multi-branch FCN	[176]
Ovarian cancer cells	Extracellular vesicles	ssTEM	Fully residual U-Net	[33]

transform the image content of different datasets to make them more similar to training dataset [181, 182]. On the other hand, training on data from various types of tissues may improve robustness [170]. Lastly, problems arise due to artifacts introduced during sample preparation and imaging, which are rare in commonly used training datasets (e.g. CREMI, SMEMI3D). Solutions include increasing the occurrence artificially using data augmentation [150], locally realigning image sub volumes before region agglomeration [153], or by supplementing these public datasets with manually segmented data from a portion of the imaging volume.

Deep learning for the masses

Although automatic segmentation methods are becoming more powerful, they are often difficult to adopt by those with limited programming skills. To leverage the power of automatic segmentation in a more user-friendly way, several state-of-the-art algorithms and architectures have been integrated into popular image analysis tools. Fiji contains plugins such as 'Trainable WEKA segmentation' for interactive training of machine learning algorithms [183] and 'DeepImageJ' [184] for straightforward importing and deployment of deep learning models. Similarly, ilastik [185] also supports simple and interactive training of machine learning algorithms and currently offers limited support for pre-trained CNNs. Microscopy Image Browser (MIB) has been extended with a user-friendly U-Net [186]. UNI-EM [187] is yet another user-friendly tool that integrates multiple top-performing 2D and 3D network architectures. Some tools work with cloud deployment to circumvent the need for local computational resources and software installation, such as DeepEM3D [178] and ZeroCostDL4Mic [188].

While these applications have reduced the barrier to entry for AI-based analysis, there are several potential drawbacks. These include the limited number of implemented models and the verification of performance, as users generally look at visual segmentation quality without employing quantitative performance statistics. Furthermore, computational expertise and resources remain necessary for the documentation and maintenance of these tools. Lastly, different implementations require a varying level of knowledge about machine learning.

2.6 Challenges in data storage, management and visualization

The output of vEM is very information dense, but there are several hurdles in maximizing its potential use. Currently, vEM data set sizes range from several gigabytes to hundreds of terabytes, with several studies already having reached the petabyte-scale [57, 72, 68]. This has big implications for data storage and management. Data formats should be clear, accessible and complete to make sure data can be reused and revisited. Visualization tools should offer fast terabyte scale data inspection. We will discuss the implications of the throughput increase and widened scope of vEM methods on data management and visualization.

2.6.1 Data storage

Where to store large vEM data sets and their annotations? Small data sets can be managed on individual PCs or workstations, but with the current trend (Figure 2.1D) it is evident that storage on institutional servers or in the cloud will become the standard.

Repositories and metadata

Systematic archiving of data and metadata in online repositories is not yet routine practice in the field of vEM, though several dedicated repositories have emerged. These include the Electron Microscopy Public Image Archive (EMPIAR) [189], Image Data Resource (IDR) [190] and the EMBL BioImage Archive[3] (BIA). EMPIAR is EM specific, whereas IDR and BIA are more broad. Currently, these repositories allow the download and upload of whole data sets, but it may be easier to interact with (a subset of) the data via application programming interfaces (APIs) or viewers. How data should be formatted and stored is an ongoing discussion in the EM community. While it is generally accepted that EM data should follow the FAIR format [191] to maximize reuse, it is difficult to standardize metadata because the needs vary greatly based on the application or imaging modality. Nonetheless, recently a set of guidelines for Recommended Metadata for Biological Images (REMBI) was published [192]. This will be incorporated as a standard for submission into IDR.

Data formats

How is vEM data stored? Different file formats are used depending on the application and storage location. During acquisition, data is often saved in proprietary microscopy data formats, which are optimized for writing. For visualization purposes, however, the optimal format is entirely different. Data with high lateral but low axial resolution (i.e. ssTEM,

---

[3] https://www.ebi.ac.uk/bioimage-archive/

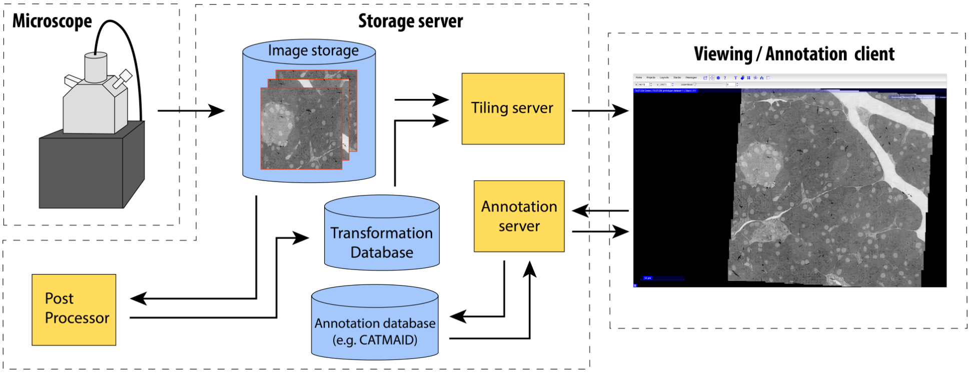

Figure 2.6: Example of data management structure. The image data is acquired by an electron microscope and stored within a central database. The database is connected to a post-processing service which performs image processing and computes the transformations between the images, which are contained in a separate database. The annotations are contained in a separate database (here, CATMAID). A client can send requests to the image, transformation and annotation database to view certain image data and corresponding annotations. The image data is tiled before it is sent. The arrows indicate the flow of information.

ATUM-SEM) is made possible by making use of pyramids of increasingly downsampled flat images (*tiles*), either remotely (CATMAID) or locally (TrakEM2). This is convenient because these images are usually viewed in 2D. Data with high axial resolution (FIB-SEM, SBF-SEM) is instead saved in a cube format (employed by KNOSSOS) which makes browsing or reslicing in the z direction faster and easier. In data archiving, flexible file extensions such as TIFF and HDF5 are used, which can store multidimensional pyramidal data with associated metadata. However, data from TIFFs can only be read as individual 2D tiles, while HDF5 and other 'next generation file formats' such as N5[4] and Zarr[5] allow reading and writing of three-dimensional chunks of images to separate, smaller files, which is much faster and better suited for cloud storage [193].

2.6.2 Data management

Client-server applications are becoming a popular tool to interact with vEM data [137, 139, 194, 76]. Plugins for processing, visualization and annotation can be remotely installed, and there is no need to download data or install software locally other than a web browser. Moreover, research data can be more easily shared as data can be made accessible to multiple users from different locations simultaneously. The data and metadata are stored in remote servers, while the user retrieves the data via a client (Figure 2.6).

'Local' data management

An open, flexible and scalable data management platform suitable for electron microscopy data is Open Microscopy Environment Remote Objects (OMERO) [195]. It was created with the idea of standardizing data access. Data can be imported using Bio-Formats, which

---

[4] https://github.com/saalfeldlab/n5

[5] https://github.com/zarr-developers

converts proprietary microscopy data formats into a common data model (currently, OME XML with OME-TIFF) [196].

Cloud data management

Apart from the costs, hosting EM data in the cloud offers several advantages in terms of convenience and accessibility. One such example is Neurodata.io[6] [197], a community-developed and maintained software ecosystem for neuroscience data deployed in the commercial cloud (AWS), containing TrakEM2 for registration, NeuroGlancer[7] for visualization and BossDB [198] for data management. Multiple datasets of different formats and imaging modalities can be combined. In addition, the hosted data can be accessed via annotation software (VAST / KNOSSOS). Another example is OpenOrganelle, a repository for cell biology data, created at the Janelia Research Campus and also hosted in the cloud [199]. The platform hosts 10 FIB-SEM data sets of various cell lines and tissues for online visualization and offline data mining, while at the same time providing the code and tutorials for all available tools. Separately, the entire EM volume of *Platynereis dumerilii* is hosted in N5 format in cloud object storage at EMBL and can be accessed using an N5 API. The data can be browsed using a specifically designed Fiji plugin ’PlatyBrowser’ in MoBIE [76]. These projects demonstrate the potential and conveniences of cloud data management of vEM data.

Developing scalable architectures

Apart from developing new tools, there is the challenge to make scalable architectures out of existing tools. Employing these tools on high performance computing (HPC) clusters allows large data sets to be processed in parallel. Vescovi *et al.* developed a scalable and modular pipeline which integrates multiple software modalities such as TrakEM2, NeuroGlancer and Flood-Filling networks to perform several tasks from registration to annotation and visualization [200]. These tools are made HPC deployable and wrapped in an operational database which can be used to create custom pipelines for image processing and annotation.

2.6.3 Terabyte data viewers

Some annotation tools have been designed with large datasets in mind. Examples are VAST [140] and NeuTu [194]. VAST is mainly a segmentation and annotation tool, and is able to handle very large datasets, which can be imported from a server or locally. Manual segmentation at different zoom levels is also supported, although simultaneous editing by multiple users is not. In contrast, NeuTu allows collective proofreading and correcting errors created by automated segmentation by manually merging or splitting segments. It is part of DVID [201], a distributed, versioned, image-orientated data service in which NeuTu acts as the data client. DVID works with 2D and 3D data and has a version control feature to manage different annotation states. Lastly, BigDataViewer [202] and Multimodal Big Image Data Exploration (MoBIE) [76], both Fiji plugins, make use of the convenient HDF5 format to interactively navigate and visualize large image sequences. MoBIE is additionally equipped with an object storage backend to load data from remote sources.

---

[6] https://neurodata.io/

[7] https://github.com/google/neuroglancer

2.6.4 Collective annotation

The last ten years have seen the emergence of projects in which researchers can collectively work on annotating vEM data. Some of these endeavors actively encourage non-scientists to participate through 'citizen science' initiatives. Non-scientists can help with proofreading annotations produced by automated segmentation algorithms (for example in the game Eyewire [167]) or they can assist in generating training data for deep learning applications (e.g. 'Etch a Cell', [165]). The fruit fly community has developed FlyWire [168], with the goal of collectively mapping the fruit fly connectome from whole brain data sets [8, 56]. It resembles EyeWire but is currently limited to researchers only.

2.7 Conclusion and outlook

Almost 10 years after the review of Briggman and Bock [30], there has not yet emerged a vEM technique that makes others obsolete. FIB-SEM and to some extent SBF-SEM remain the methods of choice in studies where high isotropic resolution is favored over throughput, for example in cell biology. The high isotropic resolution also provides the advantage of more precise automated segmentation. 'Enhanced FIB-SEM' allows the imaging of larger samples. The implementation of new milling approaches will hopefully speed up FIB-SEM even further. ssTEM has seen several innovations (TEMCA, GridTape, AutoTEM) that greatly improve the throughput. It offers the highest lateral resolution, but its limited axial resolution and artifacts hamper automated image analysis. For all techniques, a considerable amount of manual proofreading remains necessary after automated segmentation. This results in many studies still heavily relying on manual annotation efforts. Nevertheless, the performance of automated segmentation algorithms will likely improve further given their recent introduction in the field and the general interest in AI research.

Multibeam SEM should not be ignored. The possibility to increase the throughput of a single microscope by orders of magnitude is very cost-effective. However, both approaches are (for the moment) incompatible with block-face approaches, making them dependent on serial sectioning. Nevertheless, the speed of mSEM could be key in rapid diagnostics (digital pathology) [203] but also in studying brain development in multiple specimens [67, 204, 205]. The MultiSEM has demonstrated compatibility with ATUM. FAST-EM still has to demonstrate compatibility with a high-throughput sectioning approach.

Currently, the expertise in large vEM is limited to several research groups. Centralized imaging facilities (core facilities) could take a leading role in investing in high-throughput electron microscopes and the elaborate data infrastructure required for these machines. Will it be possible to image and annotate a full adult zebrafish in the near future, maybe even a mouse brain? Will the imaging and annotation of a small animal brain follow a path similar to the human genome project? An average adult mouse brain has a volume of 485-530 mm^3 [206]. It is clear that more automation is needed. Advancements in methodology will probably again play a key role, but it will also require extensive collaboration and sharing of resources.

Information from high-throughput studies, such as connectomes of animals or atlases of healthy and diseased tissue, will presumably give critical insights. It can lead to direct discoveries or provide a starting point to test hypotheses on the relation between structural changes and disease onset with functional studies. Novel data mining approaches and meta-analyses of various data sets could give new insights in ultrastructural differences between data sets of various tissues and animals, similar to microarray studies.

In conclusion, methodological improvements are making vEM more accessible and are alleviating the burden on throughput. Automated segmentation methods are reducing the workload of manual annotation, but considerable human effort remains necessary. In the field of data management, there is a need for a joint approach on how to manage large vEM data. The adoption of a common file format could improve collaboration and simplify training of automated segmentation methods. We see an opportunity for open hosting of data sets with corresponding annotations to maximize the profit to the community. The potential of vEM may be greater than ever before.

Acknowledgments

Elizabeth C. Carroll initiated the project and suggested the topic. Ryan Lane contributed to sections 4, 5 and 6. Jacob P. Hoogenboom and Elizabeth C. Carroll secured funding and supervised. All authors discussed and edited the manuscript for publication. We thank Ben Giepmans and Ahmad Alsahaf from the University Medical Centre Groningen for helpful discussions and a critical reading of the manuscript before publication.

Data availability

The data supporting Figure 2.1 is available through the 4TU.ResearchData repository (DOI: `https://doi.org/10.4121/01efed58-9427-478a-8687-50b35daf3d9c`).

2.8 Supplementary material

Table A1: List of vEM studies and their biological application(s).

Organism	**Species / tissue type / cell line**	**Reference(s)**
Alga	*M. denticulata*	[207]
Arabidopsis (*A. thaliana*)	Root tips	[50]
	Roots	[208]
	Sieve element cells	[209]
Ascidian tadpole (*C. intestinalis*)	Larval CNS	[6]
Bacteria	*M. xanthus*	[210]
	B. subtilus	[211]
Nematode (*C. elegans*)	Larval hermaphrodite brain	[67]
	Adult hermaphrodite brain	[67]
	Adult male CNS	[80]
	Adult hermaphrodite CNS	[5]
Chick	Cornea	[212]
	Collagen fibrils	[213]
	Myocardium, endocardium, cardiac jelly	[214]
	Retina	[101]
Fruit fly (*D. melanogaster*)	Central brain	[56]
	Optic lobe	[215]
	Mushroom body	[83]
	Olfactory system	[84]
	Entire brain	[8]
	Visual system	[216]
	Optic Medulla	[217]
	Ventral nerve cord	[64]
	Trachael cells	[218]
	Ovarian follicular epithelium	[218]
	Larval sensory areas	[219]
	Larval brain neuropile, ventral nerve cord	[220]
	Larval CNS	[81]
G. lamblia trophozoite	Whole organism	[221]
Human	Cardiac Telocytes	[94]
	Lung epithelial cells	[50]
	Retinal pigment epithelium	[222]
	Immortalized Breast Cancer cells	[70, 3]
	Immortalized T-Cell	[70, 3]
	Macrophage	[70, 3]
	Endothelial cells (HUVEC)	[223]
	Breast carcinoma	[73]
	Pancreatic adenocarcinoma	[73]
	Epidermal melanocytes	[224]
	Pancreatic carcinoid cells (BON)	[225]
	HeLa cells	[70, 3]
	Hepatoma cells (Huh-7)	[92]
	Lung Alveolar Epithelium	[95]
	Connective tissue	[78]
	HIV-infected Primary CD4+ T cells	[226]
	HIV-infected macrophages	[227]
	HIV-infected dentritic cells and T cells	[91]
	Primary fetal astrocytes	[226]
	Jurkat CL.E6-1 cells	[226]
	Macrophages and *B. burgdorferi*	[228]
	Cerebral cortex	[68]
Barrelclover (*M. truncatula*)	Root tips	[50]
Monkey	COS-7 cell line	[93, 3]
Mouse	Hippocampus	[229]
	Enteroendocrine cells	[230]
	Retinal starburst amacrine cells	[166, 231]
	Primary somatosensory cortex layer 1	[204]
	Choroid Plexus	[232, 3]
	Lateral parietal association cortex	[233, 234]
	Retina inner plexiform layer	[58]

	Cochlea (inner hair cells)	[87]
	Posterior parietal cortex	[234]
	Secondary visual cortex	[234]
	Anterior cingulate cortex	[234]
	Skin	[50]
	Corpus callosum	[50]
	Visual Thalamus	[90]
	Primary beta cells	[4]
	MD4 B cells	[235]
	Pancreatic Islets	[236, 237]
	3T3 fibroblast cells	[238]
	P. chabaudi infected erythrocytes	[239]
	Liver	[240, 79]
	Optic nerve	[211]
	Osteocyte lacuno-canalicular network	[241]
	Urinary bladder	[172]
	Visual cortex	[62, 89, 72]
	Lung tissue	[50]
	Cytotoxic T-Cell attacking cancer cell	[70]
	Primary somatosensory cortex	[88]
	Primary somatosensory cortex layer 4	[59, 205]
	Primary somatosensory cortex layer 2/3	[205]
	Medial nucleus of the trapezoid body	[242]
	Neocortex	[66, 57]
	Ventral Posteromedial Thalamic Nucleus	[243]
	Granule cells	[244]
	ventral tegmental area, Dopaminergic system	[245]
	Cerebellar cortex	[246]
Ringed worm (*Platynereis dumerilii*)	Whole organism	[76]
Rabbit	Amacrine cell network	[247]
	Carotid artery elastin	[248]
	Retina	[130]
Rat	Astrocytes	[249, 250]
	Cingulum	[251]
	Hepatocytes	[252]
	Corpus callosum	[251]
	Medial entorhinal cortex layer 2	[109]
	Perilesional cortex	[251]
	Podocytes	[253]
	Hippocampus	[254]
Sea urchin	Embryonic tissue	[255]
Sheep	Cardiomyocytes	[69]
Plankton	Thalassiosira pseudonana	[256]
Tobacco plant	Meiocytes	[257]
T. brucei	Full body	[75]
Yeast	Saccharomyces cerevisiae	[74]
Zebrafinch	High vocal center	[258]
Zebrafish (*D. rerio)*	Heart Junctional Region	[259]
	Entire larval brain	[7]
	Spinal segment	[86]
	Larval spinal cord	[260]
	Larval tail	[261]
	Larval dorsal-lateral lanastomotic vessels	[77]
	Larval intersegmental vessels	[77]
	Larval Neuromasts	[262]
	Larval olfactory bulb	[263, 122]
	Larval Hindbrain	[85]

3

Optical STEM detection for scanning electron microscopy

Recent advances in electron microscopy techniques have led to a significant scale up in volumetric imaging of biological tissue. The throughput of electron microscopes, however, remains a limiting factor for the volume that can be imaged in high resolution within reasonable time. Faster detection methods will improve throughput. Here, we have characterized and benchmarked a novel detection technique for scanning electron microscopy: optical scanning transmission electron microscopy (OSTEM). A qualitative and quantitative comparison was performed between OSTEM, secondary and backscattered electron detection and annular dark field detection in scanning transmission electron microscopy. Our analysis shows that OSTEM produces images similar to backscattered electron detection in terms of contrast, resolution and signal-to-noise ratio. OSTEM can complement large scale imaging with (scanning) transmission electron microscopy and has the potential to speed up imaging in single-beam and multibeam scanning electron microscopes.

This chapter has been published as: Arent J Kievits, B H Peter Duinkerken, Job Fermie, Ryan Lane, Ben N G Giepmans, and Jacob P Hoogenboom. “Optical STEM detection for scanning electron microscopy”. *Ultramicroscopy* 256 (2024), Article 113877.

3.1 Introduction

Electron microscopy (EM) of tissues and cells has gained a significant track record in the past twenty years due to improvements in methodology. Volumetric reconstructions with a resolution of several nanometers offer insight into biological function at different organizational scales. However, the low inherent throughput of electron microscopes still restricts the applications of most studies to volumes smaller than 10^6 µm^3 [39, 264]. Recent efforts have focused on improving the throughput by automating sample collection and loading [48, 8, 64], parallelization of sample processing and simultaneous acquisition on multiple instruments [61, 63, 56, 62, 89, 57] and reducing overhead and increasing the autonomy of acquisition platforms [62, 89, 8, 57, 265, 63]. Throughput can be increased by more than an order of magnitude with multibeam scanning electron microscopy (mSEM), in which the sample is scanned in parallel with an array of beams in a single instrument [96, 60, 26].

Still, the acquisition speed in every technique remains fundamentally limited by the theoretical minimum exposure time, electron beam current, magnification, and sample contrasting (i.e. staining) needed to obtain images that are suitable for biological interpretation. Electron collection and detector efficiencies further define the practical limit. The detector orientation determines to a large extent the collection efficiency, although immersive magnetic or electrostatic fields may further influence both factors [266]. The detector efficiency is determined by the internal layout of the detector. In segmented backscattered and transmission electron detectors, semiconductor materials form the active layer for conversion of the electron signal into a measurable current [267]. In such a setup, the detection efficiency is dependent on the electron energy. For biological SEM with beam energies optimized for contrast, both the electron yield and detection efficiency are typically low. This implies relatively long pixel dwell times (> 2 µs). Nevertheless, optimization of detection conditions of backscattered imaging in a scanning electron microscope (SEM) can reduce acquisition times up to 20-fold [268].

Transmission imaging may be preferred for imaging ultrathin biological samples in a conventional SEM [269, 28], as this can yield a higher signal-to-noise ratio (SNR) and improved dynamic range [28]. As an alternative to grid supports, the sample can instead be placed on a scintillator that directly converts the transmission signal into a photon signal. This photon signal can then be measured with a photon detector, as employed previously to image whole cells grown on a scintillator surface [270]. Development of a mSEM for imaging ultrathin biological specimens has further motivated transmission imaging with a scintillator. It allows for straightforward separation of the individual signals compared to secondary electron (SE) or backscattered electron detection (BSD) [26, 28]. The contrast in this imaging scheme depends on the transmission coefficient of the sample, providing a readout of the electron density of the specimen.

Here, we present a detailed investigation and benchmarking of this detection technique for SEM, which we name optical scanning transmission electron microscopy (OSTEM). Of particular interest for EM applications is the fastest imaging rate that can be achieved without compromising on image quality. We find that the signal-to-noise ratio of OSTEM images exceeds that from most conventional SEM detection techniques for short (< 1 µs) dwell times. Moreover, SEM imaging of zebrafish and rat pancreas tissue with OSTEM yields images with similar contrast and SNR as BSD.

3.2 Results and discussion

3.2.1 Single beam optical scanning transmission electron microscopy

In OSTEM, ultrathin biological sections are directly placed on a thin film-coated, cerium-doped single-crystal yttrium aluminium garnet (Ce:YAG) scintillator (Figure 1A). The thickness of the scintillator crystal (0.15 mm) ensures the objective lens correction collar can be used, while not making the scintillators too thin and thus too fragile for use during sample preparation.

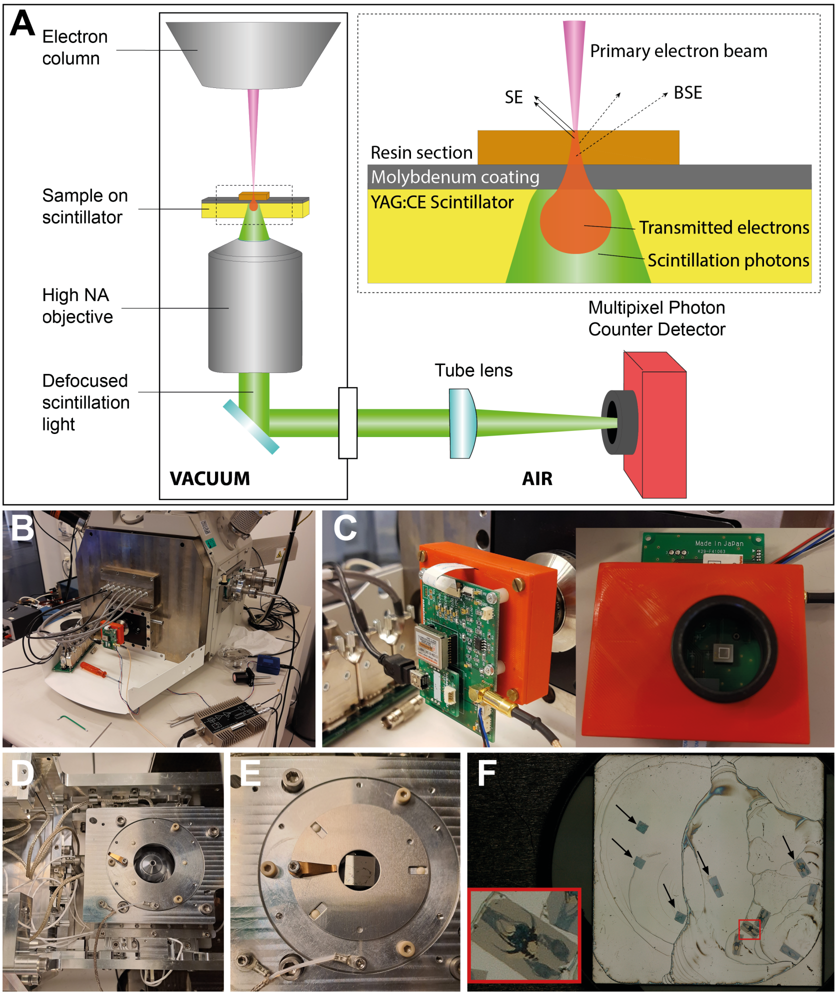

Figure 1: Optical scanning transmission electron microscopy (OSTEM). **A**: Schematic illustration of the imaging scheme and substrate. The electrons transmit through the sample and molybdenum layer, generate photons in the scintillator which are captured by the objective and projected onto a multipixel photon counter (MPPC, outside the vacuum). **B**: SECOM with emission filters removed for OSTEM detection. **C**: MPPC. **D**: Sample stage with top plate and objective. **E**: Sample ring holding the scintillator substrate with the sections. **F**: Reflected light microscopy image of zebrafish sections on scintillator.

OSTEM is implemented in a modified Scanning Electron Combined Optical Microscope (SECOM [271], Figure 1B); the impinging focused electron beam transmits through the sample and coating layer to reach the scintillator. The resulting photon signal from the scintillator is collected by an air objective and projected onto a multipixel photon counter situated outside of the vacuum (Figure 1C). The geometry of the SECOM, with the objective directly situated under the sample carrier (Figure 1D-E), allows for a high collection efficiency. Prior to EM, low magnification images are taken with a digital light microscope to guide navigation and region-of-interest selection inside the SEM (Figure 1F).

3.2.2 Optimizing OSTEM landing energy

Before comparing OSTEM to other detection techniques, we experimentally determined the optimal landing energy (LE) by acquiring images of zebrafish larval tissue at increasing landing energies (Figure 2A) and measuring the SNR and image histograms (Figure 2B-C). The SNR is expected to increase with the LE due to the generation of more signal photons per electron. Images under 2.5 keV were not recorded because the recorded photon signal was too low. The SNR rises with increasing landing energy until it peaks at 3.5 keV (Figure 2B). The trend in the histograms, towards a narrower spread in intensity values (Figure 2C), corresponds to the qualitative observation that the image contrast seems to visually deteriorate (Figure 2A) for landing energies higher than 4 keV. This is accompanied by a decrease in SNR. Based on these results and the fact that the resolution is expected to increase with the landing energy, we chose 4 keV as the landing energy for all subsequent experiments unless noted otherwise.

3.2.3 Qualitative comparison to backscattered electron imaging

After determining the optimal LE for OSTEM, we then acquired OSTEM and BSD images of rat pancreas and zebrafish larval tissue with different LEs and detectors but otherwise identical acquisition parameters. The image contrast for BSD was experimentally found to be best at 2 keV LE (rat pancreas) and 1.5keV (zebrafish) respectively. A comparison between inverted BSD images and OSTEM images shows apparent similar contrast (Figure 3). BSD and OSTEM resolve the same ultrastructural details, such as insulin granules in the islet of Langerhans of the rat (arrows in inset top row of Figure 3) and mitochondrial cristae in the zebrafish larval liver (arrows inset bottom row), demonstrating the qualitative similarity between images obtained with both detection methods.

3.2.4 Characterization of background texture in OSTEM

Of particular concern is the background texture in OSTEM resulting from a non-uniform detection efficiency of the scintillator across the field-of-view. To address differences in and between individual scintillator plates, images were acquired simultaneously using OSTEM, BSD, and secondary electron detection (SE, Figure A1). To isolate the background texture, the substrate without tissue was imaged. For three different scintillator plates, each using similar detection settings, images were acquired 50 µm apart to illustrate large-scale spatial differences in the scintillator efficiency. A Gaussian filter with a large sigma was then applied to blur out smaller scale variations caused by surface defects. Subsequently, the remaining intensity variations were measured (Table A1).

Within every scintillator plate, the difference between the minimum and maximum

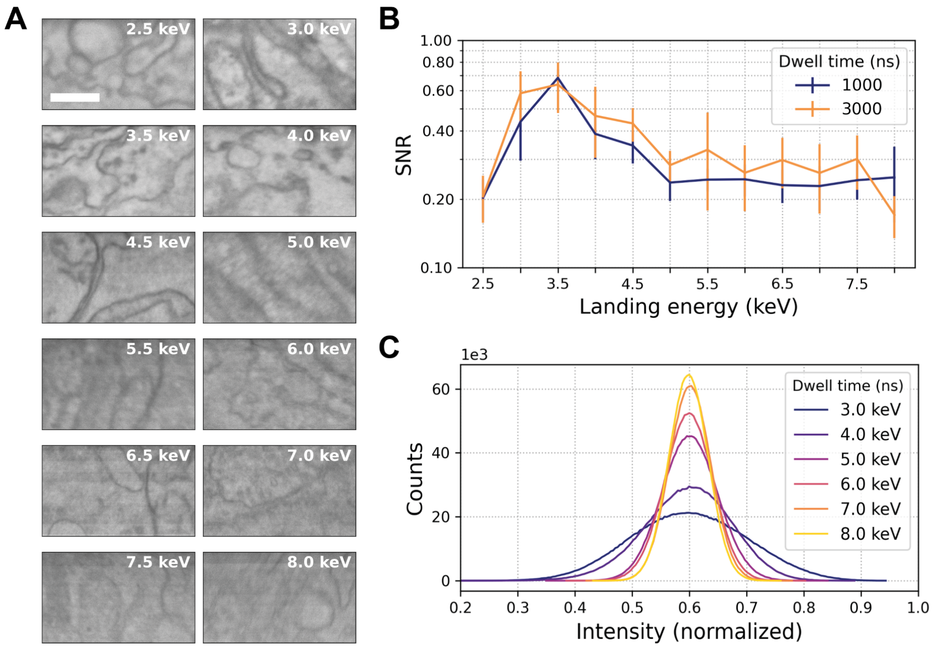

Figure 2: Landing energy optimization of OSTEM. **A:** Images taken with increasing landing energy (increments of 0.5 keV) but fixed 3 µs dwell time and 0.4 nA beam current. Scale bar: 500 nm. **B:** Mean SNR with standard deviation of images per landing energy, showing a peak at 3.5 keV. A single SNR value is calculated for each image by averaging the SSNR over the full frequency spectrum [272]. **C:** Intensity histograms of images in **A** (median corrected), illustrating a decrease in contrast for higher landing energies.

image intensity was not larger than 12% of the mean, with two scintillator plates exhibiting differences below 5%. To account for outliers, the standard deviation over the mean intensity was calculated, which yielded a maximum intensity spread of 2.6%, 1.5%, and 0.80%, respectively. Thus, the background texture caused by variations in detection efficiency within the scintillator is low. Notably, we observed that one scintillator exhibited a mean intensity approximately 20% higher than the other two, despite the use of nearly identical detection settings.

3.2.5 Quantitative comparison to other detection methods

We then performed a systematic comparison to other detection methods: BSD with and without the use of a negative stage bias potential (BSD-SB and BSD respectively) and secondary electron detection (SE). Additionally, the results were compared with annular dark field detection in a scanning transmission electron microscope (ADF-STEM). The performance was quantified by acquiring images of zebrafish tissue with increasing dwell times (Figure 4A) and evaluating the SNR (Figure 4B) in both field-free and immersion modes of the SEM.

It was found that the short dwell time (<1 µs) images from OSTEM, SE and ADF-STEM are characterized by streaking. Streaking appears at fast scan rates and can originate from

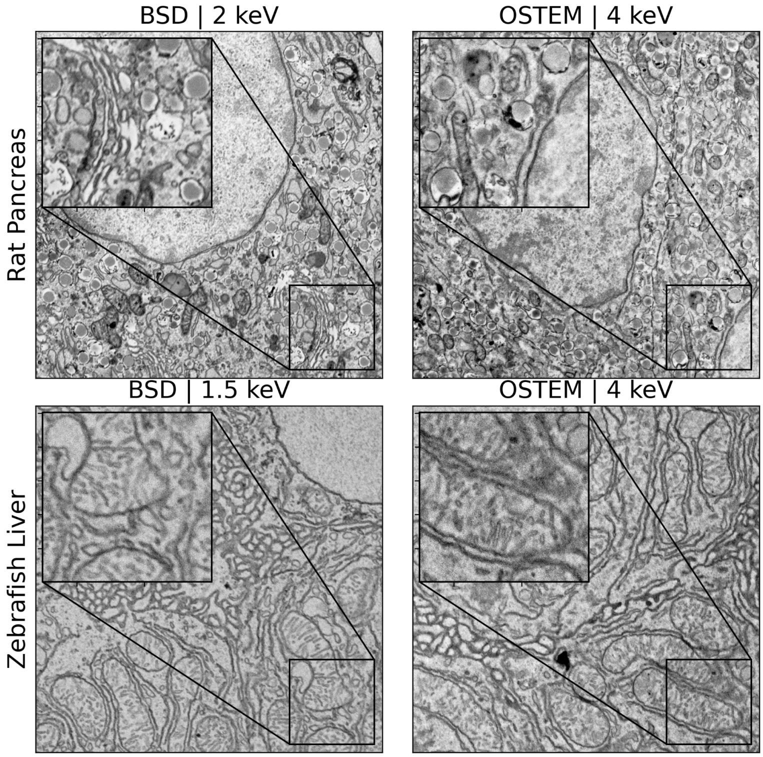

Figure 3: Qualitative comparison of OSTEM versus BSD imaging (inverted contrast). The data were acquired from rat pancreas (top row) prepared with rOTO protocol and zebrafish larval liver tissue (bottom row) prepared with reduced osmium and *en bloc* NdAc staining. Images were acquired with 4 nm pixel size, 10 µs dwell (top row), 5.1 µs dwell (bottom row), and 0.4 nA beam current. Scale bar: 2 µm.

both the detector or readout electronics response and scintillator afterglow [273, 274]. Signal from the previous scan position is carried on to the next, which results in artifacts parallel to the scan direction. This translates to a vertical band in the Fourier transform of the image (Figure A3). The method for calculating the SNR by [268] is sensitive to streaking as it uses adjacent lines (which have correlated signal) parallel to the scan direction. Streaking artificially increases the correlated signal, therefore leading to a false SNR value (Figure A4). To circumvent this, only adjacent image lines orthogonal to the scan direction were compared.

The SNR values of OSTEM, BSD and SE images were found to be comparable. Moreover, the SNR for images with short (<1 µs) dwell times is higher for OSTEM than for all other detection methods except ADF-STEM. At longer dwell times, however, the SNR of BSD-SB images increases significantly, outperforming BSD, SE as well as OSTEM. Overall, ADF-STEM yielded images with the highest SNR. The trends and relative differences for the immmersion mode were similar (Figure A2).

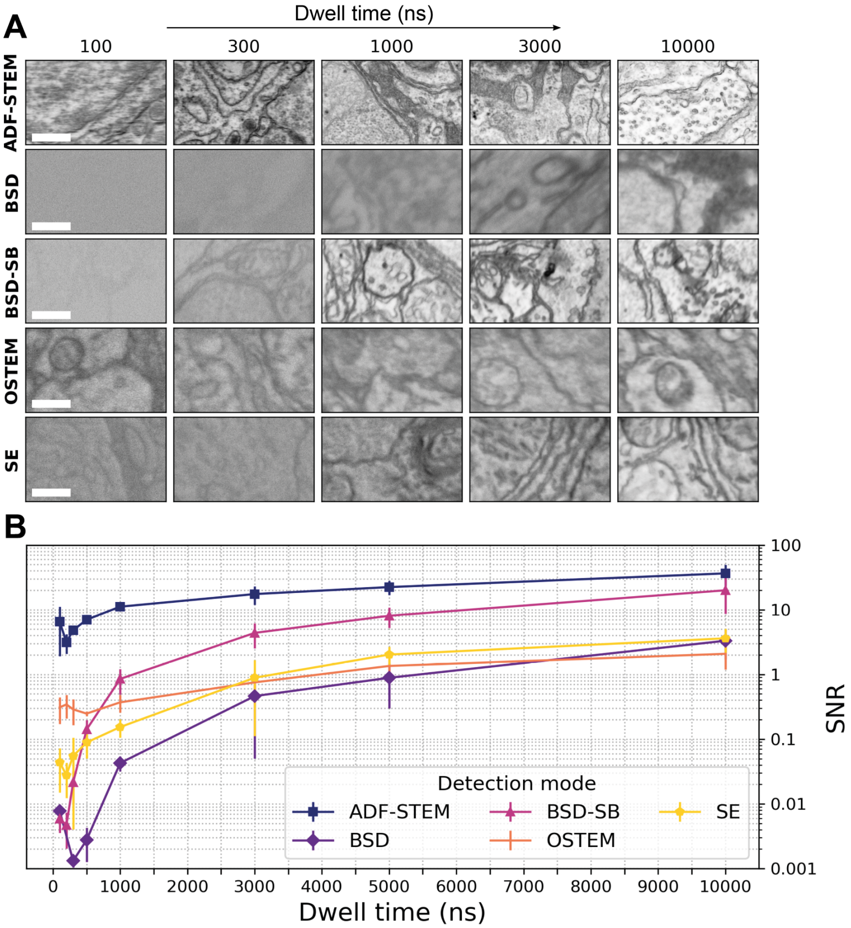

Figure 4: Quantitative comparison of OSTEM to other detection methods. **A**: Representative high magnification images taken with different detectors at increasing dwell times. Scale bars: 500 nm. Intensity values of all images are min-max normalized from the original 16-bit range (8-bit for ADF-STEM). **B**: Mean SNR and standard deviation of images in **A**. BSD: Backscattered electron imaging (1.5 keV LE). BSD-SB: Backscattered electron imaging with a −1 kV negative stage bias (1.5 keV keV LE). OSTEM: optical scanning transmission electron imaging (4 keV LE). SE: secondary electron imaging (1.5 keV LE). ADF-STEM: annular dark field scanning transmission detection, performed in a separate microscope (25 keV LE). Contrast was inverted for BSD, SE and BSD-SB. All images were acquired with a 400 pA beam current, except for ADF-STEM (385 pA).

While the trends of the SNR curves appear similar between the different detectors, there are subtle differences. The SNR curves for OSTEM and SE remain constant at short dwell times (<1 μs) and then start to gradually increase for longer dwell times (>1 μs), while the SNR for BSD, BSD-SB and ADF-STEM consistently increases with dwell time. Only for dwell times longer than (1 μs) do the SNR curves follow a similar trend, albeit with different absolute values.

Following the SNR measurements, the image resolution of OSTEM was measured and compared to the other detection methods considered. Factors that determine the image resolution are the probe size of the SEM, the electron-sample interaction, SNR and pixel size [275]. By choosing a pixel size smaller than the probe size and a long dwell time, the image resolution should only depend on the probe size and electron-sample interaction. Popular methods by which the resolution can be determined are measuring the separation between two adjacent objects and recording a line profile of the signal across a sharp (knife) edge. Traditionally this is done on a high contrast sample such as gold-on-carbon. Because an electron-transparent sample is required for OSTEM, 20 nm gold colloid particles were used instead. A knife edge experiment was then approximated by determining the distance between two percentiles of a line intensity profile over these particles, also called the edge width. To minimize the effect of their spherical shape, the 35% and 65% percentiles were chosen. The edge width was calculated for various detection methods and landing energies in immersion mode (Figure 5), as this yields the smallest probe size and thus the best resolution possible. It was found that OSTEM provides slightly higher image resolution than BSD (4 keV vs 1.5 keV LE). Indeed, OSTEM provides nearly identical image resolution to BSD at 4 keV LE. SE images yielded lower image resolution than OSTEM and BSD.

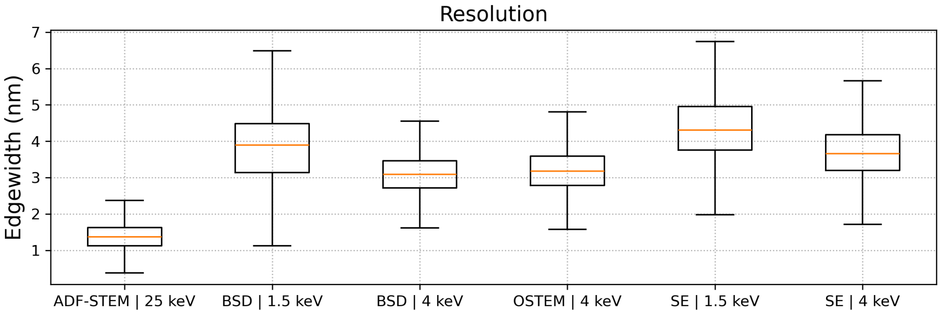

Figure 5: Comparison of measured 35%-65% edge width distributions of detection methods on 20 nm gold nanoparticles. Box plots depict the median value (in orange), 1st and 3rd quartile (vertical box edges) and the first and 3rd quartile minus 1.5 times the inter-quartile range (whiskers). OSTEM has a higher image resolution than BSD with 1.5 keV landing energy.

3.2.6 Local saturation in the OSTEM scintillator

In OSTEM, the transmitted electron beam directly generates a photon signal by electron scattering in the scintillator. Signal generation thus occurs in a tightly confined volume in the scintillator approximately equal to the electron interaction volume of a focused electron beam. In fact, the focused electron beam interaction volume extends from the ultrathin tissue sample through the conductive coating layer into the scintillator. Signal generation in the scintillator thus occurs in the lower part of the interaction volume (see also inset in Figure 1A). A higher density of electron scattering events may possibly lead to local saturation of the scintillator, thus the signal generation could be sensitive to the beam current.

The current and dwell time dependence of the OSTEM signal was therefore assessed as reflected by the SNR (Figure 6). Series of images were acquired with either increasing beam currents and a fixed dwell time (Figure 6A), or increasing dwell times and a fixed current (Figure 6B). By definition, the SNR is expected to increase by $\sqrt{N}$ for an N-fold increase in either beam current or dwell time. The signal generation is proportional to the total number of scattering events, which increases with both the beam current and dwell time. The relationship between the SNR and dwell time or beam current is therefore expected to be similar. However, with an increasing beam current but fixed dwell time, the experimental SNR consistently stagnates for currents of 0.4 nA and larger (Figure 6C). When increasing the dwell time and keeping the beam current constant, the SNR keeps increasing, following the expected trend for the theoretical SNR (Figure 6D). Thus, increasing the beam current does not have the same effect on the SNR as increasing the dwell time.

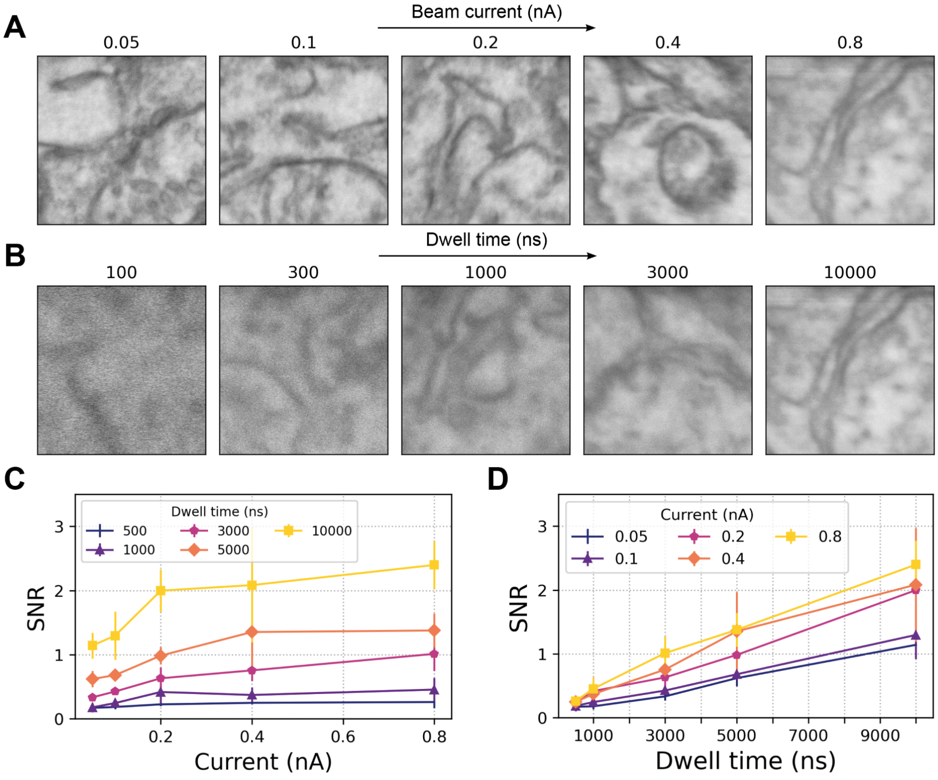

Figure 6: Relationship between dwell time, beam current and SNR in OSTEM. **A**: OSTEM images with increasing beam current and fixed dwell time (10 µs). **B**: OSTEM images with increasing dwell time and fixed beam current (0.8 nA). **C**: Mean SNR and standard deviation showing a stagnation of the SNR.**D**: Mean SNR and standard deviation, showing that the SNR keeps increasing. The used landing energy is 4 keV.

3.3 Discussion

The deposition of ultrathin sections directly onto a scintillator substrate is a viable alternative to placing tissue on thin foil spanned across grid, as traditionally performed in (S)TEM. The TEM grid bars obscure parts of the sample potentially leading to missing data, though a single slot grid can be used to circumvent this. Nevertheless, the scintillator provides a much larger unobstructed area of view in comparison to a single slot grid. This allows the collection and imaging of more sections on a single substrate. Thus, placing ultrathin sections on a scintillator substrate for OSTEM is suitable for high throughput applications.

The determined optimal landing energy of 4 keV is the same energy at which the product of the simulated SNR and contrast-to-noise ratio (CNR) was previously found to be maximized [28]. It should be noted that this optimum may shift somewhat depending on the specific sample composition, staining, section and coating thickness. The relation between the landing energy and the SNR and image contrast is not trivial. Similar to [28], a stabilization of the SNR beyond 5 keV is observed. While we report a lower absolute SNR, shorter dwell times, a lower beam current and a different tissue with less heavy metal staining were used. The sample from [28] consists of tissue on a TEM grid fixed onto a different type of scintillator and coating. These factors all have an effect on the final SNR and contrast.

We addressed to what extent the added background texture of the scintillator influences OSTEM image quality. The contribution from the non-uniform detection efficiency of the scintillators is acceptably low, but notable differences in mean intensity may exist between individual scintillator plates. The latter observation implies a variance in total photon yield, possibly attributable to differences in crystal growth conditions. In BSD and SE imaging schemes, electron energy is chosen such that most of the scattering events take place in the biological section and thus the substrate's underlying surface topography is not revealed. In ADF-STEM, the biological section lies on a formvar layer, which is electron-transparent at 25 keV beam energy. While the SE images reveal some surface defects, these are less pronounced in OSTEM. We attribute this to the different contrast mechanism in OSTEM, which is less sensitive to surface roughness than SE. Furthermore, the electron beam will spread in the biological section, thereby blurring out defects in the underlying substrate. Thus, the contribution of the substrate surface to the total background texture is minimal. Nonetheless, the polishing quality of the scintillator is important in minimizing the background texture.

In our experiment, the SNR of BSD-SB outperformed OSTEM for dwell times longer than 1 µs. At shorter dwell times, however, OSTEM outperforms BSD with and without a bias potential. This suggests that transmission imaging is the preferred option when biasing the sample (or alternatively the detector) is not an option. Similarly, ADF-STEM outperforms OSTEM as its 25 keV energy electrons generate more signal. Furthermore, it was established that streaking leads to a false signal-to-noise value for short dwell time images. In practice, the dwell time should be several times the scintillator decay constant to minimize the streaking contribution to the signal. Scintillators with shorter decay times are available, but the luminescence wavelength must be compatible with the optical components and detector.

It was found that OSTEM provides slightly higher resolution than BSD. This is attributed to decreased chromatic aberration due to the higher primary beam energy. We attribute the lower resolution of SE compared to OSTEM mainly to the contribution of so called SE2s, i.e. SEs generated by backscattered electrons, which are emitted from a larger area around the primary beam incident point. Furthermore, SEs may diffuse through the material before being emitted. Therefore, the position where the SEs originate from may be slightly different from the primary beam position, which for BSD has a more direct relation.

The image quality in SEM is not only determined by the SNR and resolution, but also the contrast-to-noise ratio (CNR). However, no reliable method exists to estimate the CNR from tissue since no two positions in the sample will have the same composition. Furthermore, the detector gain has to be adjusted between landing energies, further influencing the CNR. It is therefore impossible to compare the CNR between images acquired at different landing energies.

The image quality in OSTEM can be further improved. The main limiting factors are possible local saturation of the scintillator and the high backscattered electron coefficient of the molybdenum coating layer. In the interaction volume, energy is deposited very inhomogeneously with most electron scattering occurring below the electron beam focus. Thus, for the scintillator, most electron scattering events are expected just below the coating layer, which may in turn lead to strongly localized energy deposition. In the scintillator material, the photon signal is generated by energy transfer to the active Ce dopants [276], which for high local energy density may be prone to additional energy loss. We found indirect evidence that this leads to a sub-linear increase of the photon signal and hence a partial saturation of the light output. Also, the finite doping concentration and decay time of the Ce atoms may limit the transfer of electron energy into photon signal leading to signal saturation. The degree of saturation is not only influenced by the beam current, but also by the beam energy and the coating layer composition and thickness. The latter influences how much the electrons spread out before hitting the scintillator, thus determining the extent of saturation. Lastly, charging below the coating layer may play a role since the scintillator itself is non-conductive.

A full explanation and prediction of the expected SNR as a function of the dwell time, beam current, landing energy and other experimental parameters such as the coating thickness would be beneficial for finding optimized conditions. However, this requires an extensive physical model of the signal generation process, including electron scattering, transport of excited energy, conversion, quenching and saturation. This is a subject of future research. A thorough understanding of the signal and noise contributions in OSTEM and subsequent optimization may further improve throughput and lead to faster possible scanning speeds in single-beam and multibeam scanning electron microscopes.

3.4 Materials & methods

3.4.1 Biological sample preparation

4 dpf to 4.5 dpf zebrafish larva were fixed overnight in 2% glutaraldehyde (GA) and 2% paraformaldehyde (PFA) in 0.1 M sodium cacodylate buffer (SCB) at 4 °C. Subsequently, the fish were post-fixed in 1% osmium tetroxide and 1.5% potassium ferrocyanide for 2 hr in 0.1M SCB. Next, *en bloc* staining was performed with 4% neodymium acetate in MilliQ for 30 min at RT. The neodymium acetate was pre-spun at 21.000 g for 5 min [277]. Be-

tween each step, the samples were washed 3 times for 5 minutes each using MilliQ at RT. Afterwards, the tissue was dehydrated in 30%, 50%, 70% ethanol (10 min per step at RT), followed by dehydration in absolute ethanol (10 min, 20 min, 2 × 30 min), acetone (dried at MgSo4), 2 × 10 min, RT. The sample was then incubated with EPON:acetone mix (1:1) overnight at RT, followed by incubation with fresh EPON at 3 hr minimum at RT on the next day, then 15 min at 58 °C, followed lastly by 1 hr at 200 mbar. The fish in EPON were then oriented in moulds and left overnight at 58 °C to polymerize.

Rat pancreas was prepared according to the reduced osmium-thiocarbohydrazide-osmium (rOTO) protocol [242]. Rat pancreas was isolated, fixed overnight in 2% GA and 2% PFA in 0.1 M SCB at 4 °C and subsequently embedded in 4% agarose (in 0.1M SCB), after which 60 µm vibratome sections were cut and washed with 0.1 M SCB. The vibratome sections were post-fixed in 2% osmium tetroxide, 1.5% potassium ferrocyanide and 4 mM calcium chloride in 0.1 M SCB for 1 hr at 4 °C. Subsequently, the tissue was exposed to 0.22 µm-filtered thiocarbohydrazide for 20 min at RT followed by 2% osmium tetroxide for 30 min at RT. The tissue was further contrasted by submerging it in 2% uranyl acetate in MilliQ overnight at 4 °C. The following day, a solution of lead aspartate was made by combining 10 mL of 3 mM aspartic acid (pH 3.8) with 0.066 g of lead nitrate and adjusting the pH to 5.5 with 1N KOH. After removing the uranyl acetate, the sample was *en bloc* stained with the Walton's lead aspartate solution for 30 min at 58 °C. Between each step, the tissue was washed 3 times for 5 minutes each using MilliQ at RT [278]. Finally, the sample was dehydrated and embedded in EPON as described above.

3.4.2 Specimen preparation

80 nm ultrathin sections were cut from the embedded zebrafish larvae and rat pancreas tissue using a UC7 ultramicrotome (Leica) with a diamond knife connected to a water bath (Diatome Ltd). The sections were transferred directly onto the surface of the scintillator crystal with the help of Perfect Loop (Diatome Ltd), after which the sample was dried on a hot plate. The scintillators were stuck to a SECOM ring holder (Delmic B.V.) with a piece of carbon tape. No further coating was performed before loading the samples in the microscope. Overview images of the scintillator were taken prior to EM using a VHX-6000 digital light microscope (Keyence) operated in reflection mode.

3.4.3 Experimental setup

We have made several modifications to the sample substrate used by [28]. In this protocol, sections are transferred to a regular TEM grid which is then stuck to a boron-coated CRY-18 scintillator. In this work, cerium-doped yttrium aluminum garnet (ce:YAG) scintillator screens (Delmic B.V.) were sputter coated with a 30 nm layer of molybdenum to reduce charging and saturation. To detect scintillation photons, we use the same setup from [28] by modifying a SECOM integrated fluorescence microscope (Delmic B.V.) retrofitted into a Verios 460 SEM (FEI) (Figure 1A-B) with a fixed 6 mm working distance. The emission filters of the fluorescence microscope were removed and the cMOS camera was replaced with a Hamamatsu multi-pixel photon counter (MPPC, model s13360-3050CS). A 0.95 NA air objective (Nikon) was used for photon collection. The signal from the MPPC was amplified by a DHPVA-101 voltage amplifier (Femto) with a 20-30dB gain and 100 MHz filter before feeding it into the external detector port of the SEM.

3.4.4 Imaging

For OSTEM imaging, the SECOM objective was aligned to the detector with x- and y-translations using its dedicated stage. This was performed while scanning the electron beam at low magnification until the cathodoluminescence signal from the scintillator was in the center of the screen. Subsequently, the emission light was defocused on the MPPC to prevent saturation of the detector by a z-translation of the objective stage. The operating voltage of the detector, which controls the sensitivity, was set to a value between 52 and 54 V to achieve a mean intensity approximately half the bit-depth to prevent histogram clipping. BSD was performed with the retractable concentric backscattered detector (FEI), employing a 1.5 keV or 2 keV landing energy (experimentally found to produce the best images). BSD with stage bias was performed with the setup as described in [268], applying a -1 keV stage bias and a 2.5 keV beam energy resulting in a 1.5 keV landing energy. SE detection was performed with the Everhart-Thornley detector (FEI) in field-free mode or the through-the-lens detector (FEI, operated in SE mode) in immersion mode. SE and BSD images were acquired simultaneously for convenience.

ADF-STEM images were acquired with an annular darkfield quadrant detector, mounted in a Supra 55 SEM (Zeiss), at a fixed landing energy of 25 keV and a measured probe current of 380 pA. To prepare the sample for imaging, ultrathin sections were picked up from the water bath after sectioning with a 2 × 1 mm slot grid and placed on a metal plate with holes covered by a thin layer of formvar.

3.4.5 Quantitative measurements

The signal-to-noise ratio of the images was quantified by averaging the spectral signal-to-noise ratio (SSNR) [272] over the full frequency space of every electron micrograph [268]. Additionally, the SSNR was validated using a method based on cross-correlation [275]. Both methods require the pixel size to be smaller than the probe size such that successive scan lines have a high amount of overlap in signal. A pixel size of 1 nm was used for all SEM-based detection techniques and 0.5 nm for ADF-STEM. This is several times smaller than the highest measured image resolution (3 nm for OSTEM and 1.3 nm for STEM respectively). For every measurement, the stage was moved to a fresh region in the sample. The average SNR value was taken of at least 4 images. The SSNR is calculated using the following formula:

$$\text{SSNR (R)} = \frac{\sum_{r \epsilon R} |\sum_k F_k(r)|^2}{\frac{K}{K-1} \sum_{r \epsilon R} \sum_k |F_k(r) - \overline{F}(r)|^2} - 1 \tag{3.1}$$

where $F_{k(r)}$ is the Fourier transform of the k'th image (alternating scan line), with K images (scan lines) in total. $\overline{F}(r) = \frac{1}{K} \sum_k (r)$ is the mean of the Fourier transformed images and R is the region of interest. If R is the full image, a single SNR value is obtained. R can also be a ring in Fourier space.

Images with artificial streaking (to mimick a short dwell time condition) were created by flattening a long dwell time image (with high SNR) into a 1D array, followed by a discrete 1D convolution with a kernel K containing the intensity contributions from the previous i scanning positions (pixels), i.e.

$$I_s = (I * K)[n] = \sum_{m=-\infty}^{\infty} I_m K_{n-m}, K = [1, w_0, w_1, ..., w_n] \tag{3.2}$$

where I_s is the artificially streaked image, I is the original image and the weights w_n are computed as the integral over a single dwell time t_d (of the short dwell time image) of a single exponential decay function with decay constant τ,

$$w_i = \int_{it_d}^{(i+1)t_d} e^{-\frac{t}{\tau}} dt, i \geq 1 \tag{3.3}$$

The image resolution of the detection techniques was estimated from 20 nm gold colloid nanoparticles (Sigma Aaldrich) directly deposited on a molybdenum-coated Ce:YAG single crystal. To approximate a knife-edge measurement, the 35%-65% edge width was determined using the software 'FEI Image' from images taken in the immersion mode of the SEM. The histogram of edge widths as produced by FEI image was exported and combined for all images acquired with a single detection technique. A pixel size 0.5 nm was used for SEM and 0.2 nm for ADF-STEM, which is several times smaller than the measured resolution. A 10 µs dwell time was used for SEM and and 3 µs for ADF-STEM to obtain images with a high SNR.

3.4.6 Large-scale imaging

Large-scale OSTEM imaging as presented in Chapter 5 was performed with the ODEMIS software (Delmic B.V.). The signal from the MPPC was rerouted into the SEM signal port of the SECOM hardware. We typically used a landing energy of 4 keV, a dwell time of 5 µs and pixel size of 4 nm (25900× magnification, 16.1 µm horizontal field width) for the large scale acquisitions. The scan rotation angle was set in a way that the ROI in the ultrathin section of interest was aligned with the FOV movement (a snake pattern, alternating movements right and left, downwards). Beam alignment, focusing and astigmatism correction were performed in the middle of the ROI prior to acquisition. Next, a tiled acquisition was performed in ODEMIS with 10% overlap between neighboring tiles. The tiles were computationally stitched using SIFT [127] and RANSAC [129] to generate a *mosaic* that covers the whole region of interest. The 2D reconstructions were rendered using Render [1] and exported to a local instance of CATMAID ([137]) using custom Jupyter notebooks.

Acknowledgements

Job Fermie and Jacob P. Hoogenboom conceived of the study. B. H. Peter Duinkerken performed the sample and specimen preparation and the ADF-STEM imaging. Ryan Lane provided the code for the SNR analysis and assisted with the OSTEM experiments. Jacob P. Hoogenboom and Ben N. G. Giepmans secured funding and supervised. All authors discussed the results and edited the manuscript for publication. We thank Anouk Wolters from the UMC Groningen for preparing the rat pancreas sample used in this research.

---

[1] https://github.com/saalfeldlab/render.git

Data and software availability

The raw microscopy data, code and analysis scripts are available through the 4TU.ResearchData repository (DOI: `https://doi.org/10.4121/9c98aee1-608e-4c71-8b89-dcb1e8eb3e5e.v2`).

3.5 Supplementary material

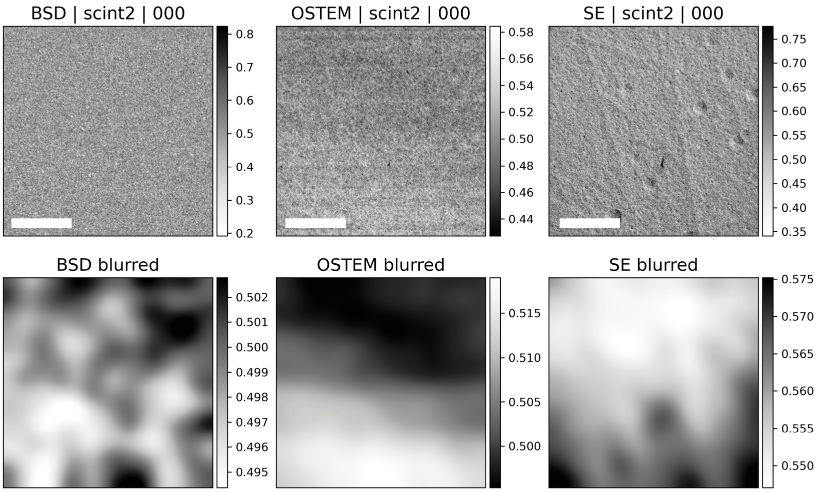

Figure A1: Background texture characterization of ce:YAG substrates. Images from the susbtrate surface without biological sample were acquired with backscatter electron detection (BSD), secondary electron detection (SE) and OSTEM with a HFW of 8.192 µm, 0.4 nA beam current, 4 keV landing energy, 10 µs dwell time and identical operating voltage. Images were convolved with a Gaussian filter with σ of 100 to blur out surface defects. Intensities are scaled between the 1st and 99th percentile of the data. Scale bar: 2 µm. The OSTEM image shows an intensity gradient from the non-uniform detection efficiency of the scintillator.

Table A1: Statistics on intensity distributions of Gaussian filtered OSTEM images. The measurement from Figure A1 was repeated for 3 different scintillators with 4 different images per scintillator, with a 50 µm spacing. **Imax**: Maximum image intensity. **Imin**: Minimum image intensity. **Imean**: Mean image intensity, **Istd**: standard deviation of image intensity.

scintillator	area	Imax	Imin	Imean	Istd	Imax-Imin/Imean (%)	Isdt / Imean (%)
scint1	000	0.5321	0.4821	0.5068	0.0101	9.87	1.99
scint1	001	0.5309	0.4898	0.5084	0.0096	8.09	1.89
scint1	002	0.5253	0.4811	0.5007	0.0105	8.81	2.09
scint1	003	0.5342	0.477	0.5064	0.0133	11.29	2.63
scint2	000	0.5196	0.495	0.5051	0.0074	4.86	1.47
scint2	001	0.513	0.4934	0.5031	0.0058	3.89	1.15
scint2	002	0.5124	0.4905	0.5001	0.0061	4.38	1.22
scint2	003	0.5157	0.4877	0.5008	0.0065	5.59	1.30
scint3	000	0.6148	0.587	0.6033	0.0042	4.60	0.70
scint3	001	0.6109	0.5963	0.6034	0.0027	2.43	0.45
scint3	002	0.6056	0.5904	0.597	0.0033	2.55	0.55
scint3	003	0.6012	0.5834	0.5922	0.0048	3.01	0.80

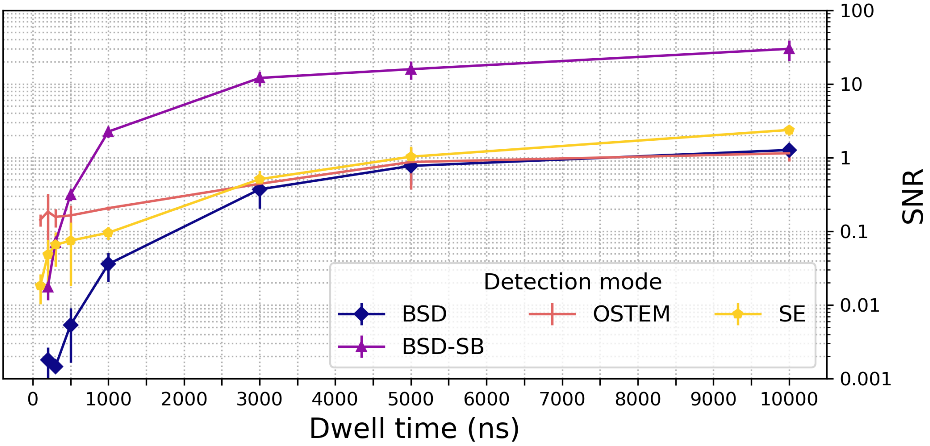

Figure A2: **A**: Mean SNR and standard deviation of images taken with different detection techniques and increasing dwell time in the immersion mode of the SEM. BSD: Backscattered electron imaging (1.5 keV LE). BSD-SB: Backscattered electron imaging with a −1 kV negative stage bias (1.5 keV keV LE). OSTEM: optical scanning transmission electron imaging (4 keV LE). SE: secondary electron imaging (1.5 keV LE). Annular dark field scanning transmission detection (ADF-STEM) was not evaluated as there is no immersion mode available on the scanning transmission electron microscope. All images were acquired with a 400 pA beam current.

The short dwell time images of OSTEM and STEM are affected by streaking. In order to validate the SNR measurements, the images were split into either horizontally or vertically alternating scan lines and the corresponding SNR values were computed. Additionally, an alternative method by Joy [275] was used to compute the SNR. A deviation in SNR when comparing horizontal instead of vertically split lines is evident up to 1 µs (Figure A4). The SNR values from both methods agree closely when only vertically split lines are used. To mitigate the effect of streaking, the SNR as reported in the main figures is therefore calculated using only alternating vertically split lines.

Interestingly, it was found that artificial streaking generated by a single exponential function with a decay constant of 500 ns produced images that most resembled the short dwell time images as judged by the Fourier transform (Figure A5). This is several times longer than the decay constant previously reported for Ce:YAG (90 ns) under electron beam irradiation [279]. We attribute the streaking at short dwell times due to a slow detector response; experiments with a photon multiplier tube demonstrated a significantly faster decay compared to the MPPC detector (data not shown). Streaking can thus be minimized by using faster electronics.

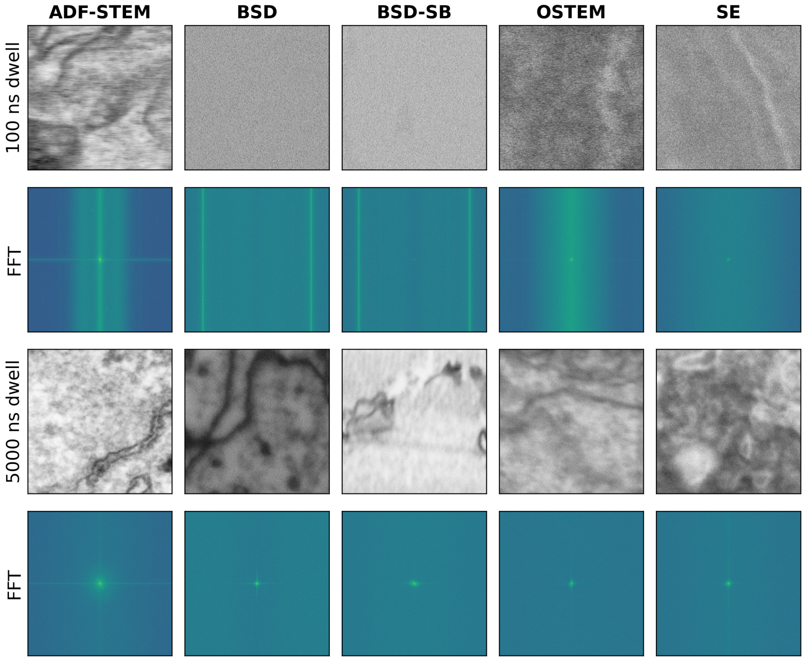

Figure A3: Comparison of images with a short and long dwell time acquired with different detection methods, along with the power spectrum of said images. Short dwell time images of OSTEM and ADF-STEM show distinct streaking.

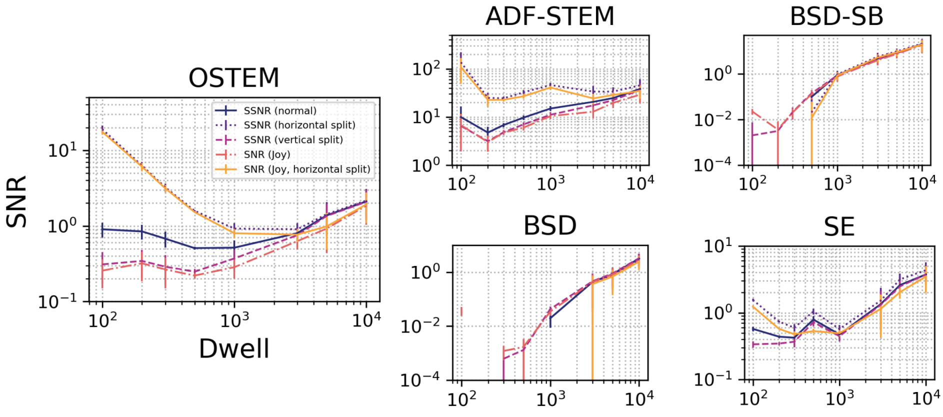

Figure A4: Averaged spectral signal-to-noise ratio (SSNR) and SNR by [275] as calculated from differently split input images taken for all detection techniques. A horizontal split indicates separating an image into alternating vertical scan lines, whereas a vertical split is along the horizontal direction. The default split in the Joy method is vertically, whereas for the SSNR the image is by default split along alternating horizontal and vertical scan lines. A horizontal split leads to a false SNR value for dwell times lower than 3 µs.

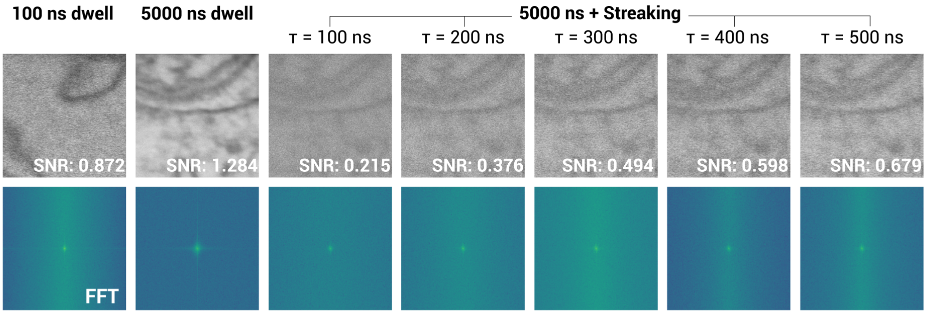

Figure A5: Artificially streaked OSTEM images. The first two columns show a short (100ns) and a long (5000ns) image with their 2D Fourier transforms, respectively. The 100ns image shows clearly a streaking effect. The remaining columns show 5000ns dwell time images with Gaussian noise where streaking is artificially added (see methods), with a decay constant t that is increased progressively. A decay constant of 500 ns resembles mostly the 100ns dwell time image.

4

FAST-EM array tomography: a workflow for multibeam volume electron microscopy

Elucidating the 3D nanoscale structure of tissues and cells is essential for understanding the complexity of biological processes. Electron microscopy (EM) offers the resolution needed for reliable interpretation, but the limited throughput of electron microscopes has hindered its ability to effectively image large volumes. We report a workflow for volume EM with FAST-EM, a novel multibeam scanning transmission electron microscope that speeds up acquisition by scanning the sample in parallel with 64 electron beams. FAST-EM makes use of optical detection to separate the signals of the individual beams. The acquisition and 3D reconstruction of ultrastructural data from multiple biological samples is demonstrated. The results show that the workflow is capable of producing large reconstructed volumes with high resolution and contrast to address biological research questions within feasible acquisition time frames.

This chapter has been published as: Arent J Kievits, B H Peter Duinkerken, Ryan Lane, Cecilia de Heus, Daan van Beijeren Bergen en Henegouwen, Tibbe Höppener, Anouk H G Wolters, Nalan Liv, Ben N G Giepmans, and Jacob P Hoogenboom. "FAST-EM array tomography: a workflow for multibeam volume electron microscopy". *Methods in Microscopy* 1.1 (2024), pp. 49–64.

4.1 Introduction

Unraveling the complexities of biology across various scales, from organs down to cells and biomolecules needs a full understanding of biological (ultra)structure. Traditionally, electron microscopy (EM) has been used to decipher tissue and cellular ultrastructure, using mainly 2D micrographs of selected areas. However, conventional EM fails to provide the context needed for reliable biological interpretation. In recent years, EM techniques collectively known as large-scale and volume electron microscopy (vEM) have emerged, offering unprecedented insights into the 3D structures of biological specimens at the nanoscale [2]. While these techniques have proven their value, the limited sustained throughput has hindered their ability to handle large volumes of samples effectively, thus restricting the scope of vEM [264].

To address the throughput limitations of electron microscopes, multiple approaches have been developed. Traditionally, vEM techniques can be divided into scanning EM (SEM) and transmission EM (TEM) techniques. vEM with TEM is based on imaging of serial ultrathin sections. The main throughput-limiting factors are the field-of-view (FOV) as set by the detector, slow stage movements and limited observable sample area as determined by the sample grids. The limited FOV of the camera and stage movements have been addressed by TEM camera array (TEMCA, [62, 89, 8]). The FOV that can be imaged with a single stage movement has further increased with beam-deflection TEM (bd-TEM, [17]). Multiple systems can be used in parallel to further boosts acquisition speeds [57]. Additionally, an electron-transparent tape-based reel system (GridTape) can be used that significantly reduces the number of necessary vacuum cycles [64]. These developments have addressed the most important throughput limiting factors of TEM.

The main focus in vEM techniques that utilize SEM has been to improve the scanning speed, which is limited by the maximum probe current allowing for high resolution imaging. Approaches have been developed that circumvent the probe current limitation using multiple parallel scanning beams, effectively boosting the scanning speed by orders of magnitude. A few implementations of multibeam SEM (mSEM) exist, including MultiSEM based on secondary electron imaging [60] and FAST-EM based on transmission imaging [26, 280].

The throughput increase achieved by TEMCA, bd-TEM and mSEM, in combination with an approach for generating large amounts of sections such as automated tape-collecting ultramicrotomy (ATUM, [49]), has made it possible to image millimeter-sized samples [57, 72, 17, 281]. However, these techniques have thus far been accessible only to a limited number of research groups and used in a narrow scope of applications. While mSEMs and GridTape have recently become commercially available, additional requirements may create new challenges for sample preparation and possible applications. The reliance of bd-TEM on electron-transparent tape complicates the section collection and handling with added risks of support film breakage and off-slot collection. In MultiSEM, the combination of a high applied bias voltage and secondary electron detection may impose restrictions on sample staining, conductivity and height tolerances.

We demonstrate mSEM imaging with the FAST-EM (Fast, Automated Scanning Transmission Electron Microscopy). FAST-EM uses a recently introduced optical transmission detection technique to separate the electron beam signals, referred to as optical STEM or OSTEM [28, 282]. In OSTEM, ultrathin sections are mounted on a scintillator that converts electrons transmitted through the section into photons, which are then collected by an objective lens below the scintillator and guided to a detector array (Figure 1). This signal generation and detection principle was recently characterized and shown comparable to commonly used backscattered electron detection in terms of contrast, resolution, and signal-to-noise ratio (SNR) [282]. Here, we report an array tomography workflow for vEM with an early adopter FAST-EM system. We performed acquisitions on cultured cells as well as tissue samples and demonstrated the wide applicability of FAST-EM. As an example, FAST-EM array tomography was applied to cultured cells, reconstructing a 265 000 μm^3 volume from 72 thin serial sections with 4 x 4 x 100 nm^3 voxel size and resolving the mitochondrial cristae and membrane structures. Our results show that FAST-EM is capable of imaging large unobstructed regions of interest with feasible acquisition times, while providing images with high resolution and contrast to address biological research questions.

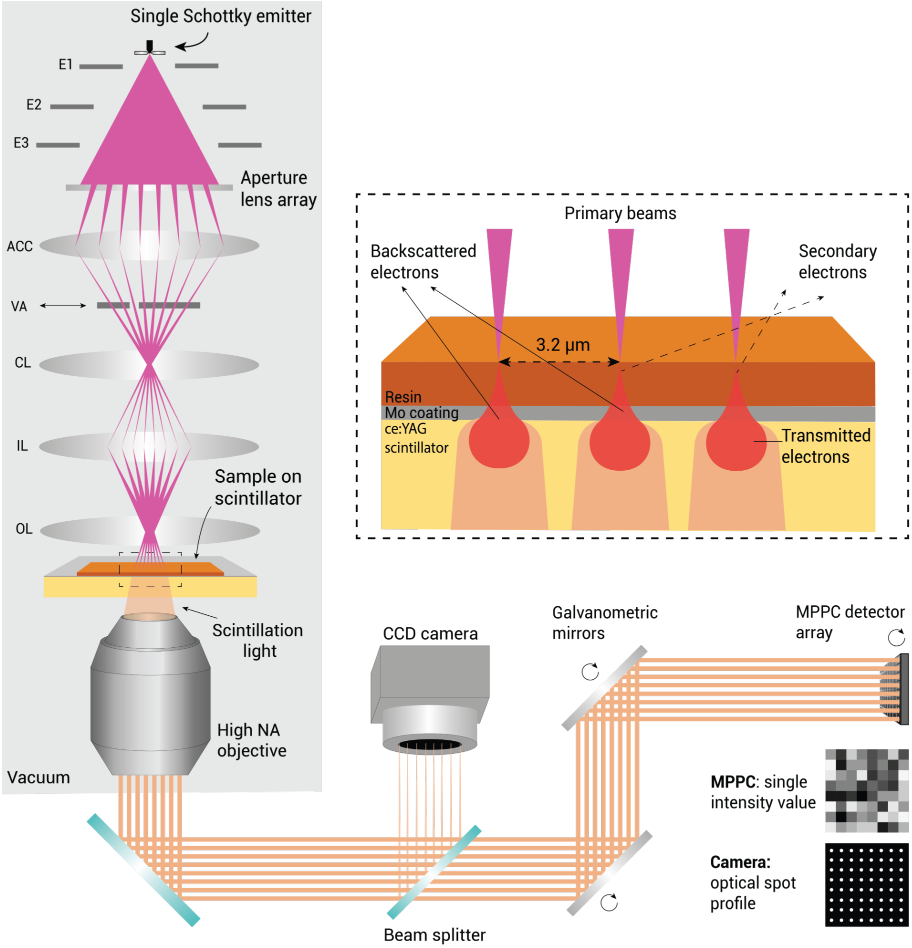

Figure 1: Caption on next page.

Figure 1: (Previous page.) FAST-EM principle. An aperture lens array splits the emission cone of a single high brightness Schottky source into an array of 8 by 8 electron beams (implementation is described in [24]). The beams scan the sample in parallel with a 3.2 µm pitch. A single beam can be selected with a variable aperture (VA). The transmitted electrons are converted into photons by a scintillator substrate and collected by a high NA objective lens. An optical system outside of the vacuum chamber (shown simplified) then descans and magnifies the optical spots and projects them onto a multipixel photon counter (MPPC) array. A CCD camera situated outside the main optical path monitors the spot profile. E1/E2/E3: Source electrodes; ACC: Accelerator lens, VA: Variable aperture, CL: Condenser lens, IL: Intermediate lens, OL: Objective lens.

4.2 Results

4.2.1 FAST-EM array tomography

In FAST-EM array tomography, serial sections are cut from resin-embedded tissue or cells and collected onto scintillator substrates (Figure 2), similar to conventional approaches [46, 47]. Serial sections are imaged sequentially, incrementing the stage and sample at fixed intervals to acquire areas larger than the multibeam field-of-view with overlap between individual images. A continuous volume is reconstructed from the 2D images using point correspondences sought in the overlap region between images in 2D and 3D. The aligned volume can then be segmented and analysed.

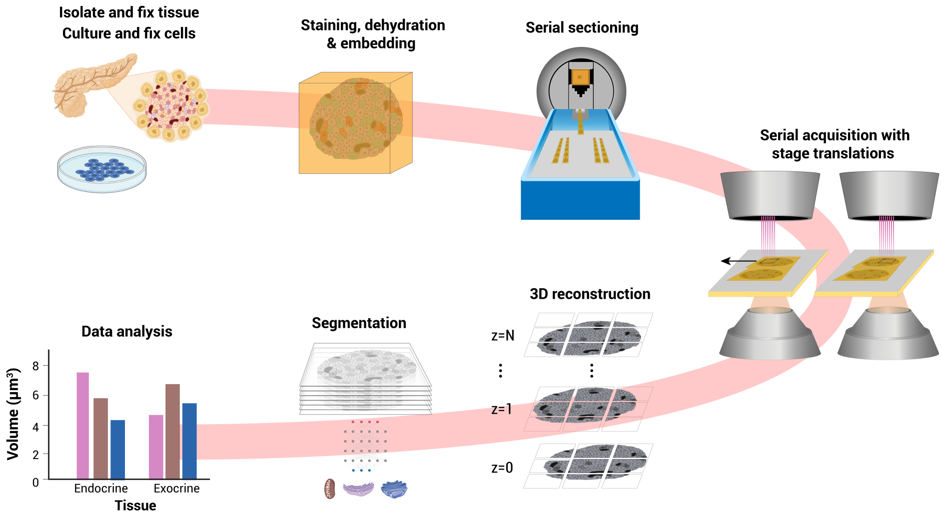

Figure 2: FAST-EM array tomography. Tissue or cultured cells are fixed, contrasted with heavy metals, dehydrated and embedded in epoxy resin. Ultrathin sections are deposited on a molybdenum-coated, cerium-doped yttrium aluminum garnet (ce:YAG) scintillator crystal in the knife bath. The sections are imaged using mosaicking with stage increments. The 3D volume is reconstructed from 2D images. Features of interest are (semi-)automatically segmented. Data analysis is performed on the segmentation results. Figure partially created with BioRender.com.

FAST-EM employs a light optical system to collect, descan, and detect scintillation photons that are produced when the electron beams scan the sample (Figure 1). The electron beams are arranged in an 8 by 8 square pattern (also referred to as *multiprobe*), created by an aperature array in the electron source module. They scan at a pitch of 3.2 µm to ensure sufficient separation on the detector array of the optical spots produced by each beamlet. The photons generated in the scintillator from the 64 beamlets are collected by a high NA in-air objective lens situated directly under the sample holder in the vacuum chamber, and projected onto a set of galvonometric mirrors that perform a descanning in both x and y directions. Approximately 5% of the photon intensity is split to a CCD camera outside of the main optical path to monitor the optical spot profile during acquisition. The remaining photons are directed onto a multipixel photon counter (MPPC) array which produces a single intensity readout for each beamlet at each scan position, building up the transmission electron image. The optical system ensures rapid electron detection and stable image quality over a prolonged acquisition time.

4.2.2 FAST-EM image acquisition

Acquisitions are preceded by an overview image acquisition (Figure A1). Low magnification images are acquired in single-beam mode (a single beam is selected through the variable aperture (Figure 1)), mapping the locations of the sections (Figure 3A). The overview images also help define the location for FAST-EM calibrations, which are run before every acquisition. The sample must first be brought into both optical and e-beam focus. An optical autofocus routine is performed (Figure 3B), which moves the sample stage in z to position the sample in the focal plane of the optical objective lens, while recording the spot profile on the diagnostic camera. The optical focus is subsequently monitored during image acquisition. After the optical focus is determined, the system is again switched to single-beam mode and the electron beam lens and stigmator alignment, focusing and astigmatism correction are performed by the user. Because the common crossovers of all beams are positioned in the objective lens and stigmator, the alignments for the single beam directly apply to all other 63 beams.

After the correct settings are found for the electron optics, three additional optical calibration steps must be performed in multibeam-mode prior to imaging to ensure that seamless, homogeneous multibeam field-of-views (*fields*) are produced from the individual 64 beamlet images (*cells*). The calibration steps are fully automated in the microscope acquisition software, but the location on the sample where these are performed must be defined by the user (Figure A2). The first calibration step aligns the multiprobe to the MPPC detector array and determines the scan orientation (not shown). The second calibration determines a digital dark offset and gain value for each MPPC to homogenize the intensities between individual beamlets (Figure 3C). This is necessary because individual MPPCs have slightly different gain factors. The last calibrations step then determines the translation between individual cells in order to produce a seamless image from 64 beams. The microscope scans a 900x900 pixel area per beamlet (100 pixel overlap) on the biological sample. The stitching is then determined by finding point matches in the overlap area and minimizing the distance between them in adjacent beam images.

Finally, regions of acquisition (*ROAs*) are defined by the user on the overview images with the ROA tool (Figure 3D, Figure A1). When the acquisition is initiated by the user, the microscope software determines the amount of fields required (with some overlap between fields) to fully image an ROA, and all defined ROAs are then automatically acquired by *mosaicking* with stage increments of 24 µm (Figure 3D-E). This produces a set of 2D images for all ROAs in the specimen (a single acquired ROA is referred to as a *megafield*). The raw images (900x900 pixel per beamlet) are real-time processed into seamless images of 6400x6400 pixels and transferred to a local storage server. On user request, the unprocessed raw images (7200x7200 pixels) can be saved instead.

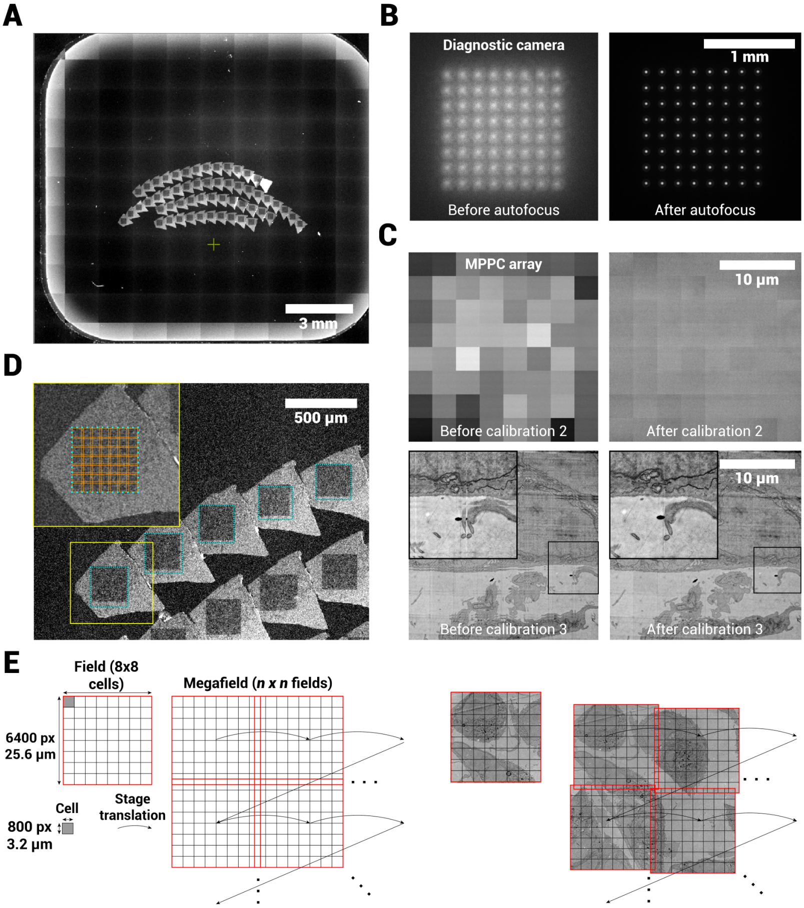

Figure 3: Acquisition workflow for FAST-EM. **A**: Overview images are acquired to guide ROA definition and calibration region selection. **B**: Diagnostic camera images of spot profile before and after optical focus calibration. **C**: Single field image (MPPC detector) before and after digital offset and gain calibration. **D**: Zoom in on overview image showing the ROAs on the sample, and the approximate division of a ROA into fields. **E**: Terminology and acquisition order of a single ROA as shown in **D**.

4.2.3 Image processing of large-scale FAST-EM datasets

We implemented an image processing workflow for FAST-EM datasets based on published software libraries for large volume reconstructions. The workflow is designed to be flexible, since acquisitions on large areas may lead to inconsistencies in data quality due to local variation of the sample and specimen preparation. Acquisition and image processing can be performed on individual sections in case reacquisition is needed because of errors. Additionally, visualization of intermediate image processing steps is incorporated to identify problems and perform qualitative assessment of the results. This also allows for reprocessing with optimized parameters.

Images are first post-corrected to remove intensity differences remaining after calibration and produced from the overscan (Figure 4). Per ROA, the average of all images is calculated and then subtracted from all images in the specific ROA. Fields that contain artifacts are detected by an outlier detection algorithm and are excluded from the average image (see methods for implementation details).

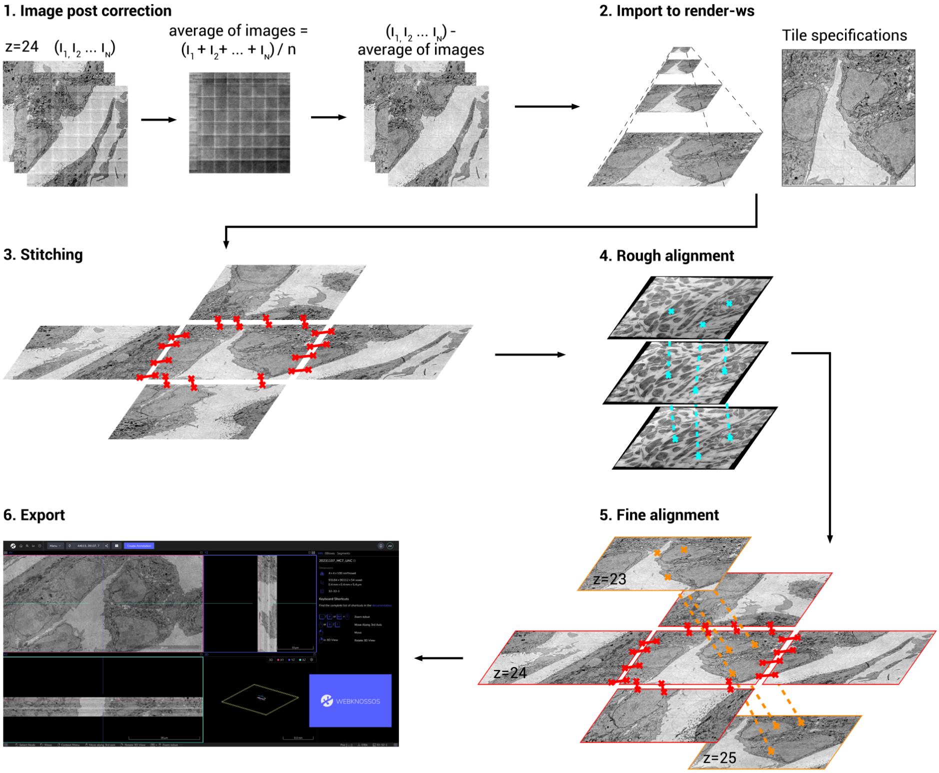

Figure 4: Image processing workflow. Images are first post-corrected for beam artifacts using an average correction image. Images are then imported into render-ws, which generates an image pyramid (Mipmap) and sets the tile specifications from the metadata. Tile pairs (neighbors in xy) are determined in the same ROA and stitched. The stitched megafields are downscaled and and point-correspondences are computed to roughly align the stack in 3D. Tile pairs determined from the roughly aligned stack (neighbors in z) are fine aligned in 3D. Finally, the aligned stack is exported to WebKnossos for viewing in 3D.

The postcorrection is designed to fail when a ROA contains many artifacts such as caused by dirt particles on the section, as this would produce a correction image that is biased by high-contrast features. In this case, the correction is performed using the correction image from the nearest section in z where post-correction succeeded.

The resulting post-corrected images and their metadata are imported to a local instance of render-ws[1], which assigns a unique identifier to every image and keeps track of its individual transformations during downstream post-processing [283]. Render-ws also saves the point-match correspondences found for each image during stitching and alignment. Tile pairs (neighboring fields) in the same ROA are then defined based on the metadata, and stitched into a montage based on point-correspondences sought in the overlap region. The images are then aligned in 3D using a two-step approach, where first an approximate rough alignment is determined from downsampled montages to find neighboring images in z, followed by a tile-to-tile fine alignment. The final result is then exported to disk and uploaded to WebKnossos [139] to be processed or analysed further.

4.2.4 Large-scale and volume acquisitions with FAST-EM

We prepared several samples for array tomography with 100 nm section thickness, including tissues and cell cultures, imaged them with FAST-EM, and reconstructed the volumes using the implemented image processing workflow (Figure 5A, Figure A3A and Table 1). Samples prepared with the ferrocyanide-reduced osmium-thiocarbohydrazide-osmium (rOTO) protocol [284] resulted in images with decent contrast. Cells stained with neodymium acetate [277] as opposed to uranyl acetate demonstrated remarkably similar contrast, indicating that the rOTO protocol is a suitable basis for preparing samples for FAST-EM.

Little residual intensity variations can be seen in the xy plane of the data, indicating that the image post-correction procedure is consistent. The effect of residual intensity differences after calibration and beam overscan is seen mainly in empty resin, where no biological features are found. The intensities and resolution are also consistent throughout the image stack.

The proportion and resolution of the data sets make it possible to trace a large number of subcellular structures and cell organelles throughout the volume (Figure 5B-C, Figure A3B-C). The axial resolution allows identification of some organelles in the xz and yz planes (Figure A4A). Nuclear membranes, mitochondrial membranes and cristae, ER, Golgi stacks and lysosomes can be reliably identified at full data resolution (Figure A4B).

By default, the alignment is solved for a set of similarity transformations (rotation, translation and scaling) on the joint set of point-correspondences between images in the same z-layer and between z-layers. This produced consistent global results, but would not always produce accurate local alignment. More elaborate transformations (i.e. full affine, polynomial transforms) lead to a higher local alignment precision, but would not always yield a globally consistent result. The initial fine alignment was therefore refined with optical flow [68], which is able to determine the fine alignment using elastic deformations while maintaining the original geometry of the biological sample [285]. This improved the local alignment, supposedly due to the algorithm being able to compensate non-linear deformations introduced during sectioning which cannot be accounted for by rigid and

---

[1] https://github.com/saalfeldlab/render

scaling transformations alone. A single misalignment can be seen (Figure 5B-C); on closer inspection of the data, however, this misalignment appears to originate from a discontinuity in the dataset which coincides with a transition between ribbons. This type of misalignment was not observed in other datasets (Figure A3, Figure A4). Therefore, this result is attributed to section loss during the preparation of the ribbons.

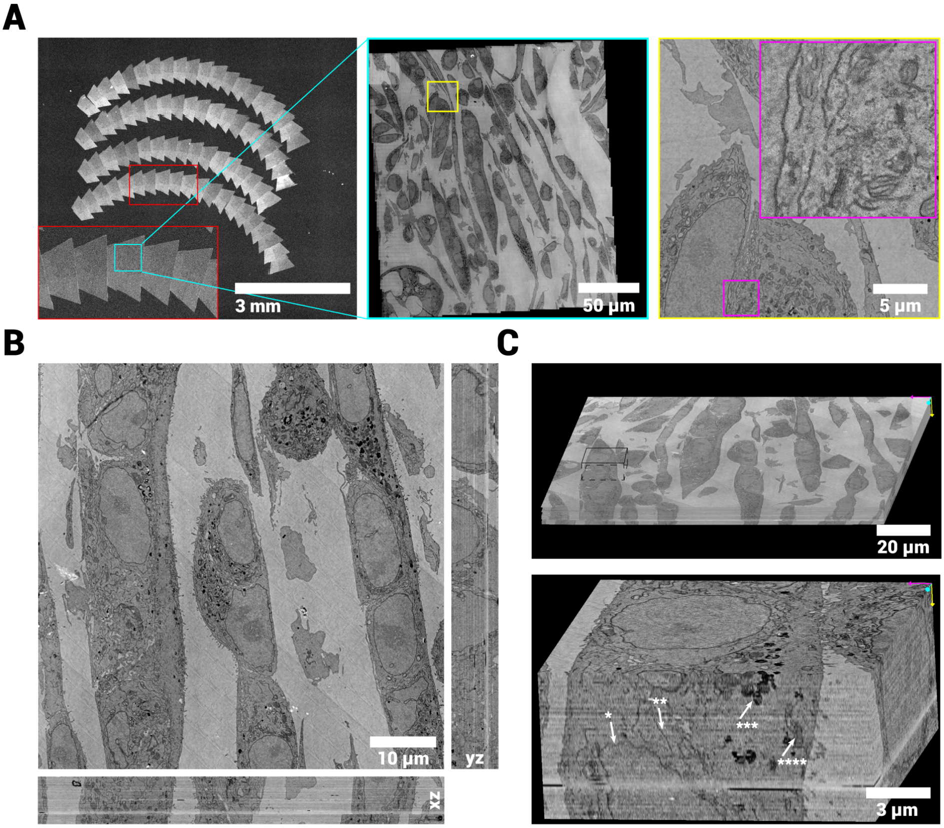

Figure 5: vEM reconstruction of cultured MCF-7 cells. **A**: Overview images of sections, showing a zoom in on a single ROA, a single field and a single cell respectively. **B**: Aligned volume reconstruction from 72 100nm serial sections showing the orthogonal reslices through the center of the stack (xz and yz). **C**: Volume rendering of the full (continuous) stack. Inset shows smaller subvolume at 8nm/pixel resolution with arrows pointing at structures of interest (Star indicators: *=Nuclear membrane, **=Endoplasmatic reticulum, ***=Lysosome, ****=Mitochondrium). The data quality and alignment is consistent throughout the stack. The complete 3D dataset at full resolution is available via Nanotomy.org.

4.2.5 Automated segmentation of FAST-EM AT data

FAST-EM data can be streamed efficiently in 3D using the WebKnossos viewer. Using WebKnossos' Python API, it is possible to access and load arbitrary views of the data at different zoom levels, which can be directly visualized and annotated in tools like FIJI or Napari [286] or further processed using popular tools for image analysis [185, 188].

Table 1: Datasets presented in this publication. The voxel size and field size are 4x4x100 nm and 6400 x 6400 pixels respectively for all datasets. The tile overlap was increased for several ROAs in the MCF-7 NdAc dataset to ensure sufficient overlap.

Dataset	**Fig.**	**Dwell time (µs)**	**No. of sections**	**Acquisition time (hours)**	**Effective throughput (MPx/s)**	**Tile overlap (pixels)**	**Raw data size (GB)**	**ROA size (µm)**
MCF-7 NdAc	5	10	72	16.7	2.75	400, 640	489.6	192 x 192
MCF-7 UAc	6, S4	20	54	29.7	1.82	400	573.8	240 x 240
Rat pancreas	S3, S5	10	44	-	-	400	74.8	96 x 96

All mitochondria were automatically segmented with MitoNet [287] (available as the Empanada plugin in Napari) to demonstrate the usability and applicability of analysis tools developed for other vEM modalities and datasets to OSTEM-detection based FAST-EM data. MitoNet is a generalist convolutional neural network architecture for segmenting mitochondria trained on a diverse training dataset. Notably without retraining nor fine-tuning the network architecture on FAST-EM data, 3D inference with MitoNet produced qualitative agreeable results, where it would recognize a large portion of the ground truth annotated mitochondria in MCF-7 cells prepared with a modified FIB-SEM staining protocol (Figure 6A). MitoNet was also applied to rat pancreas tissue, which yielded similar agreeable results (Figure A5A). Mitochondria in the MCF-7 cells appeared to have complex, elongated ultrastructure, whereas the rat pancreas datasets presented mitochondria with a more diverse collection of elongated as well as spherical mitochondria.

Several hundreds of mitochondria were manually annotated in a subset of the MCF-7 cell and rat pancreas datasets to assess the quantitative performance of MitoNet on FAST-EM data (Figure 6B and Figure A5B). The semantic IoU (intersection over union), F1 and AP (average precision) scores were then determined on both the originally aligned data and the realigned data with optical flow, to investigate the effect of alignment precision on the segmentation quality (Table 2). MitoNet demonstrated IoU scores comparable to benchmark datasets obtained using vEM modalities based on other electron detection techniques (e.g., HeLa with IoU: 0.791, F1@50: 0.728 and AP@50: 0.573 and C. elegans with IoU: 0.60, F1@50: 0.483 and AP@50: 0.318, both FIB-SEM datasets), but overal lower F1 and AP scores. Notably, the IoU scores on the rat pancreas dataset were lower (0.136 point) than for the MCF-7 cell dataset, but the F1@50 and AP@50 scores were higher (0.129 and 0.11 point respectively). The realignment of the data with optical flow did not overall influence the IoU scores, indicating no effect on semantic segmentation performance of the model. However, it did have a noticeable positive effect on F1 and AP scores (F1@50 0.266 and 0.159 point increase, AP@50 0.178 and 0.124 point increase for MCF-7 and rat pancreas, respectively). This indicates that the network is able to predict complete mitochondria more effectively on the data realigned with optical flow than on the original fine aligned data. This suggestion was substantiated by a reduced amount of false positives for both realigned datasets. A slightly larger improvement in F1 and AP scores was noted for the cell dataset than for the rat pancreas tissue.

4.2.6 Scaling up acquisitions

FAST-EM has been designed for large volume acquisitions of tissues and cells. Of interest therefore are the scalability of the acquisition and image processing to a large volume

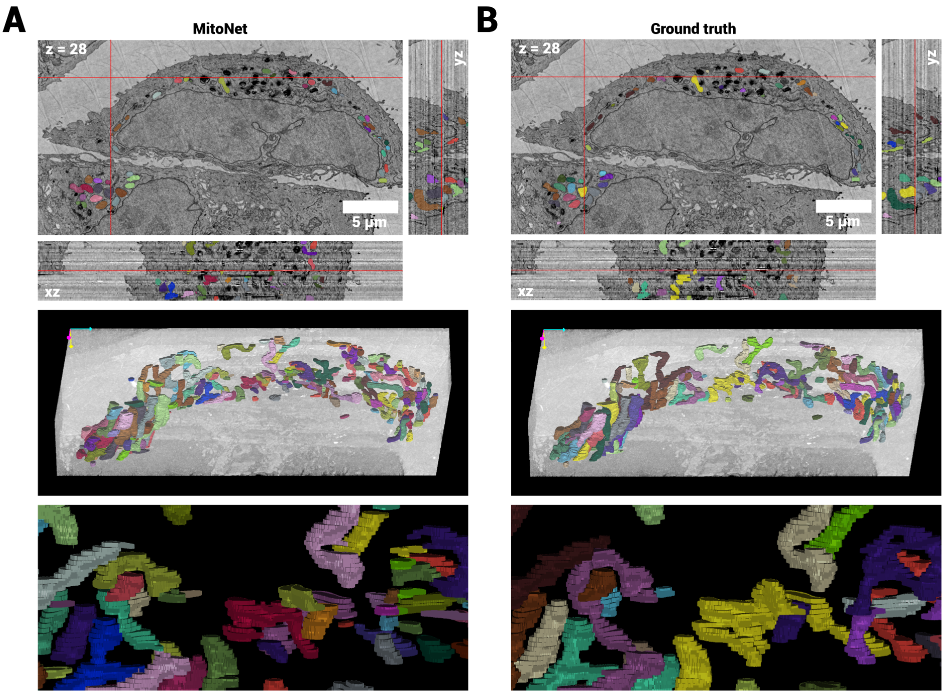

Figure 6: Automatic instance segmentation of mitochondria in FAST-EM data using MitoNet [287]. **A**: MitoNet predictions on subset of data, showing the orthogonal slices at the locations indicated by the red cross, and 3D renderings in Napari. **B**: Ground truth annotations of mitochondria from the same volume. The predictions show qualitative agreement with the ground truth, although some split errors can be observed. The complete 3D dataset at full resolution is available via Nanotomy.org.

and the expected acquisition and reconstruction times. The recent introduction of high-throughput vEM modalities has in turn required the development of image processing workflows capable of handling petabyte scale datasets [283, 288, 289]. Such data sets are not yet available from FAST-EM, but the tools that are implemented in the image processing workflow have been demonstrated on millimeter-sized volume datasets. Therefore, the workflow should be scalable to larger volumes, provided that the necessary computational infrastructure is available.

The maximum volume for FAST-EM array tomography is restricted to the number of serial sections that fits on a single 14 x 14 mm scintillator. The sample can be divided over multiple scintillators, but this requires interruption of the sectioning process and therefore involves a significant risk of section loss. A sample area of 1 mm^2 (typical in bd-TEM and MultiSEM combined with ATUM) would lead to a very limited number of sections on a single scintillator; a section size of 500 x 500 µm^2 allows for a larger z dimension. An estimated 500 sections of this size can fit on a single scintillator with a high packing density, which would also be close to the practical number of sections possible with array tomography. Assuming a section thickness of 100 nm, this yields a volume of 500 x 500 x 50 µm^3. The total estimated FAST-EM acquisition time is then computed for this sample

Table 2: Performance metrics for MitoNet 3D instance segmentation on FAST-EM data. **IoU**: Intersection over union (Jaccard index). **F1@50/75**: F1 score at 0.5/0.75 IoU threshold. **AP@50/75**: Average Precision at 0.5/0.75 IoU threshold.

Dataset	**# GT mitos**	**IoU**	**F1@50**	**F1@75**	**AP@50**	**AP@75**
MCF-7 UAC fine aligned	97	0.778	0.133	0.078	0.071	0.041
MCF-7 UAC realigned	97	0.770	0.399	0.196	0.249	0.109
Rat pancreas fine aligned	217	0.615	0.379	0.080	0.235	0.042
Rat pancreas realigned	217	0.644	0.528	0.142	0.359	0.076

Table 3: Estimated acquisition times for FAST-EM of a 500 x 500 x $50\,\mu m^3$ volume from 500 serial sections, compared to a single-beam SEM [268], beam-deflection GridTape TEM (bd-TEM, [265]) and automated tape-collecting ultramicrotomy combined with MuliSEM imaging (ATUM-MultiSEM, [290]). For FAST-EM, with the ROA placement precision of approximately one field, a padding of one row or column of fields on each ROA edge is assumed. Numbers indicated for FAST-EM are based on 10 µs dwell time as used in this study, and in brackets for 2 µs, which is feasible for brain tissues (data not shown) or when the beam current limitation in the current early adopter system is lifted. FoV: Field-of-view.

	SEM	**FAST-EM**	**bd-TEM**	**ATUM-MultiSEM**	**Unit**
Dwell time	1	10 (2)		0.05	µs
Pixel size	4	4	3.6	4	nm
FoV acquisition time	16.78	8.10 (1.62)	0.040	0.6	s
Stage overlap	10	6.25	10	6	%
Stage time per FoV	2	0.52	0.055	1	s
Per section overhead	-	52	132	36	s
FoVs per section	1156	529	81	50	
Time per section	21706	4842 (1414)	171	116	s
Total time	3015	672.5 (196.4)	23.7	16.3	h
Sustained throughput	0.72	3.23 (11.05)	91.48	133.55	MPx/s

volume and for other vEM modalities (single-beam SEM, bd-TEM and ATUM-MultiSEM, Table 3) using the reported acquisition and overhead times for a single FoV and section (if needed, corrected for the section size). The sustained throughput is then defined as the number of pixels in the volume divided by the expected acquisition time. Overhead for sample exchange, setting up the acquisition (Figure A6A) and reacquisitions are not included in this calculation. Additionally, the reconstruction time was calculated assuming the resources available on the dedicated storage server of FAST-EM (Table A1).

The calculation yields a sustained throughput for FAST-EM of 3.23 MPx/s at a 10 µs dwell time, and 11.05 MPx/s at a 2 µs dwell time. This shows that the early-adopter FAST-EM is already significantly faster than a single-beam setup (0.72 MPx/s), but the throughput is still an order of magnitude lower than bd-TEM and ATUM-MultiSEM (91.48, 133.55 MPx/s respectively). Notably, for a dwell time of 2 µs and 10 µs, the majority of the acquisition time is spent on scanning (Figure A6B). The estimated reconstruction time (54.8 days) is longer than the acquisition time (28 days at 10 µs dwell, 8.2 days at 2 µs dwell).

4.3 Discussion

FAST-EM is compatible with the existing rOTO protocol, as exemplified by both the cellular and tissue samples that were imaged and reconstructed here. Our results also show that substitution of uranyl acetate by neodymium acetate [277] yields images with similar contrast for cells. A thorough investigation and comparison of different sample preparation protocols and their effects on image contrast obtained with the OSTEM detector in FAST-EM is a subject of ongoing research.

Scintillator substrates designed for FAST-EM are demonstrated to support conventional serial-section array tomography approaches [46, 47]. The substrates provide a large unobstructed area for imaging similar to silicon wafers or ITO-coated coverslips. If a single substrate is not sufficient, multiple substrates can be used for a single sample. This, however, requires interruption in sectioning and thus may not be feasible in practice. The substrates are in principle compatible with alternative section collection techniques for volume EM, such as tape-based collection (ATUM) and magnet-based collection (MagC [119] and GAUSS-EM [291]). In practice, however, the compatibility with ATUM seems limited by the low fill factor and the transparency of the tape (we note that electron-transparent tape is available [64] but would need to be tested for compatibility with OSTEM detection in FAST-EM). The production and future use of larger scintillator wafers to accommodate more sections is likely possible, which would favour the combination with magnet-based collection, in which the sections are deposited directly on the substrate in random order and orientation as opposed to ordered ribbons.

Recently, nanoscale light microscopy-based imaging has been achieved with effective throughput rates comparable to vEM, in combination with molecular labeling [292]. Indeed, the use of correlative (light) microscopy in combination with volume electron microscopy (vCLEM) can yield biological specificity or facilitate region-of-interest selection for FAST-EM. The substrates used currently in FAST-EM, ce:YAG, are incompatible with integrated CLEM [293] or in-resin CLEM [294] as they are luminescent at commonly used excitation wavelengths for fluorescence microscopy, thus generating significant background noise. However, transparent scintillator materials can be used instead, provided that they yield sufficient light output for EM.

Overview images produced in single-beam mode provide sufficient guidance for defining ROAs and pave the way for future automatic identification of sections. While the definition of ROAs is currently still manual and limited to rectangles, we expect future software updates to be compliant with arbitrary ROA shapes or even automatic mapping. With incorporation of focus and astigmatism routines, the image acquisition procedure could be fully automated.

The post-correction of the images is a necessary but effective method for removing intensity differences caused by overscan or parking of the beams, and residual intensity differences remaining after digital offset and gain calibration and imperfect alignment of the multiprobe. The post-correction reduces or completely removes intensity differences that appear for each cell position in every field. However, there are some inconsistencies in the data that cannot be corrected for with this procedure: beam exposure artifacts in re-acquisitions of ROAs; differences in intensity distributions between sections (since the correction is performed in-plane); errors in the stitching of adjacent beamlets and sample tilts which cause large deviations from the calibration settings. Note that the latter two can be avoided by bypassing calibration step 3 through saving the raw images (at the cost of extra post-processing), and careful placement of the sample on the holder to prevent tilts. Notably, the post-correction failed to remove certain diagonal stripe artifacts appearing for each cell image in the dataset presented in Figure 6. The artifacts are proportionally more expressed in empty resin than in tissue or cells, and thus do not appear homogeneously through the dataset, which explains why they are not fully removed. The exact cause of the artifacts is a topic of investigation, but is currently attributed to sample damage from e-beam exposure.

Segmentation of mitochondria with MitoNet demonstrated similar IoU scores to benchmark datasets from other vEM modalities. This shows that MitoNet is capable of generalizing to FAST-EM datasets, and further establishes that FAST-EM data resembles data from other vEM modalities, both to a microscopist's eye and a neural network. Instance segmentation scores were overall lower than for the MitoNet benchmark datasets. This can be explained by the anisotropic voxel size; whereas the data reported here has a z resolution of 100 nm, most MitoNet benchmark datasets have higher z resolution, with several having isotropic voxels. Therefore, decreasing the section thickness is expected to lead to higher instance segmentation performance. Furthermore, Empanada offers tools to fine-tune MitoNet on images of specific datasets, which may improve semantic and instance segmentation scores on FAST-EM data.

The effective throughput for the datasets reported in this publication includes the total time spent on acquisition set-up, reaquisitions and monitoring image quality. It is difficult to calculate these numbers for other vEM modalities, especially since these would depend on the specific sample that is imaged. Therefore, we used the sustained per-section throughput of FAST-EM at both 2 µs and 10 µs dwell time (11.05 and 3.23 Mpixel/s respectively, including overhead from stage translations and calibrations) in the comparison with other vEM modalities. The per-section throughput of FAST-EM array tomography and z resolution are lower than for bd-TEM and ATUM-MultiSEM. However, the early adopter FAST-EM system still has several restrictions. The beam current is fixed at 0.4 nA. Future updates will allow a larger beamlet current without significant compromise on resolution (up to 1 nA per beamlet is possible), allowing for similar contrast and SNR at shorter dwell times. Likewise, the landing energy is fixed at 5 keV, which is a suboptimal energy for sections thinner than 100 nm. For a specific sample composition and section thickness, there exists an optimal landing energy [282]. Furthermore, the landing energy affects the crosstalk between optical signals and the image resolution; at higher keVs, the crosstalk is bigger due to the larger interaction volume of the e-beam and hence more intensity in the long-range tails of the optical spot profile of each beamlet. At lower keVs, the image resolution may be compromised due to increased chromatic aberrations. Future updates will allow tuning of the landing energy with respect to the sample composition and preparation, leading to the best possible contrast and SNR.

Pixel dwell times will be further reduced through optimization of the optical system and scintillator supply. Optimization of calibration procedure times and stage settling times has not been performed and can lead to signification reduction of overhead times. Future instrumentation development will focus on modeling and subsequent optimization of the OSTEM detector, leading to shorter possible dwell times. Another point of improvement is the beam pitch. To increase the pitch, a redesign of the electron-optical column is required. The pixel size is set by the magnification of the optical system; larger pixel sizes subsequently change the pitch and therefore the distance between spots on the detector. Currently, the magnification of the optical system is fixed. To reach an optimal dwell time for an aimed-for resolution in FAST-EM, all aforementioned factors should be considered in subsequent design improvements.

We have demonstrated a workflow implementation for volume electron microscopy using a commercially available multibeam scanning transmission electron microscope, FAST-EM. The applicability of FAST-EM to several diverse biological samples is shown. Multibeam OSTEM detection is shown to be compatible with community tools for volume alignment, reconstruction and segmentation, even when these algorithms have been developed using data obtained with other EM modalities. The data is released to the community as benchmark for future projects or for further analysis. Cellular organelles have major roles in regulating cellular metabolism and homeostasis, and it is crucial to understand their structure and function relationships. Overall, FAST-EM proves itself as a promising tool for analysis of cellular as well as subcellular organelle ultrastructure in 3D by providing high-throughput quantitative measurements. We envision FAST-EM will be further utilized in the future to systematically address how organelle ultrastructure is altered in relation to certain mutations, oncogenes, drugs and other environmental factors.

4.4 Materials & methods

4.4.1 Sample preparation

Rat pancreas samples were prepared as previously described [282], where uranyl acetate was replaced with spun-down 4% neodymium acetate [277]. Briefly, tissue was aldehyde fixed, vibratome sectioned, subjected to reduced osmium-thiocarbohydrazide-osmium (rOTO) post-fixation (1% osmium tetroxide, 1.5% potassium ferrocyanide and 4 mM calcium chloride in 0.1 M sodium cacodylate buffer, [242]), *en bloc* stained with neodymium acetate followed by lead aspartate, dehydrated and flat embedded in EPON between ACLAR sheets.

Sample fixation, staining and embedding of MCF7 cells was achieved similar to as reported before [295, 296]. In short, samples were fixed with 2.5% glutaraldehyde and 2% paraformaldehyde in 1× PHEM buffer, and poststained with 1% osmium tetroxide, 1.5% potassium ferrocyanide in 0.065M PHEM for 2h at 4 °C, followed by 1% thiocarbohydrazide (Sigma) for 20 min at RT, 1% OsO4 in ddH2O 30 min at 4 °C, 1% uranyl acetate (or 4% neodymium acetate) at 4 °C overnight, and Walton's lead aspartate (pH 5.6) for 30 min min at 58 °C. Samples were then dehydrated and infiltrated with EPON resin.

4.4.2 Specimen preparation

For the rat pancreas sample, molybdenum thin-film coated yttrium aluminum garnet scintillator (ce:YAG) plates were received from Delmic B.V. For the MCF-7 cells, ce:YAG was ordered from Surface Preparation Laboratory (SPL). RF magnetron sputter coating was performed on the SPL scintillators in-house with an AC450 (Alliance Concept) with 150 W RF at 3 µbar for 32 s to achieve a layer of 30 nm molybdenum.

The scintillator substrates were submersed in the water bath before sectioning. The tissue block was first trimmed to a trapezoidal block face. The presence of tissue or cells in the surface of the block face was verified by cutting a semithick section and staining this with toluene blue. Glue was then applied at the top and bottom of the block face to ensure the serial sections would stick, facilitating the formation of long ribbons. A single long ribbon of ultrathin sections (100nm) was then cut using a Leica UC7 (MCF-7 cells) or Leica ARTOS 3D (rat pancreas). The ribbons were split into 3 or 4 smaller ribbons. The water level was then gently lowered to deposit the ribbons on the substrate. No additional coating was performed before imaging.

4.4.3 Electron microscopy

The sample was mounted on the FAST-EM sample holder using 60 μm-thick Kapton tape on two sides opposite of the sample. The sample was then pumped to high vacuum and acclimatized for at least 12 hours. An optical focus calibration was then performed near the middle of the scintillator. Overview images were made of the sample in single-beam mode using the T1 detector (backscattered electrons) at 1.5 mm horizontal field width to facilitate the selection of ROAs. Electron beam alignment was performed in single-beam mode at 60000x magnification, and the beam was focused and corrected for astigmatism. This was followed by the FAST-EM specific calibrations, which were performed once per volume acquisition, as close to the middle of the scintillator as possible. Calibrations 1 (multiprobe alignment) and 2 (digital gain and offset) were run on a part of the scintillator where no sample was present. Calibration 3 (cell translation) was performed on a region of the sample not part of the final ROA, with continuous features (i.e. biological structures) throughout a region approximately the size of a single field. All acquisitions were performed with a 5 keV beam energy, 0.4 nA beam current and 4 nm pixel resolution. A dwell time of 10 μs was used for both the rat pancreas and MCF-7 cell specimens stained with neodymium acetate, and 20 μs for the MCF-7 cell specimen stained with uranyl acetate. All procedures except for the electron beam focusing are implemented in ODEMIS[2], which is open source software. The source code for the calibrations is closed source.

4.4.4 Serial data acquisition

ROAs were defined on adjacent sections. Each ROA position was manually verified and corrected if necessary using the single beam mode, centering the ROA position on features continuous in serial sections such as outlines of cells or contours of tissue. This ensured that the ROAs would be aligned with an accuracy of roughly a single field (25.6 μm). No scan rotation was applied to correct for the ribbon rotation, as this is not available in the early adopter model. Focus and astigmatism were manually corrected every 5 or 10 sections, or at the start of a new ribbon, which was performed in the middle section.

4.4.5 Image processing

The image processing workflow was developed based on earlier work by [293]. After post-correction, the image data and metadata are imported into render-ws[3]. The server has 128GB of RAM and 40 CPU cores for processing, but the software can take advantage of the full number of cores that is available on any system. The images (*tiles*) and

---

[2] https://github.com/delmic/odemis

[3] https://github.com/saalfeldlab/render

their respective metadata (transformations) are organized into stacks, configured as entries in a MongoDB database. Per image tile, a single geometric transformation is saved (rigid, affine, etc). Copies of the raw and post-corrected data exists on disk; only the final 3D alignment is additionally rendered to disk, whereas intermediate versions in the processing workflow are defined only by their transformations. The workflow is written in Python and JuPyter Notebook, using the render-python[4] API to interact with render-ws, which is written in Java. Stitching and 3D alignment of the images is based on finding matching image features in the overlap region between pairs of neighboring images with the Scale-Invariant Feature Transform (SIFT) [127]. Candidate matches detected by SIFT are filtered by random sampling consensus algorithm (RANSAC) [129], based on whether they adhere to a common geometric transformation. This produces a set of matched point coordinates (point matches). Using the set of point matches for all image pairs, and after deciding on a transformation model, image transformation parameters are estimated by BigFeta[5]. BigFeta solves for a set of transformations (e.g. rigid, affine) that minimizes the sum of squared distances between all point matches [132].

Image post-correction

Image post-correction was performed prior to import into by averaging all images in a single ROA and then subtracting the average image from every other image. This effectively removes residual intensity differences that are a result of scan overlap, beam flybacks and calibration errors. Outlier fields (i.e. with a deviating histogram) were excluded from the averaging. Outliers are detected using the Median Absolute Deviation, i.e.:

$$\mathrm{MAD} = \mathrm{median}(|\mathrm{X}_i - \widetilde{X}|) \tag{4.1}$$

where $\widetilde{X}$ is the median of the 1st percentile of selected images. Images are flagged as containing artifacts if their histogram 1st percentile deviates from the median percentile:

$$\mathrm{corrupted} = \mathrm{p1} < \widetilde{X} - a * \mathrm{MAD} \quad or \quad \mathrm{p1} > \widetilde{X} + a * \mathrm{MAD} \tag{4.2}$$

where a is a scaling factor that can be varied to allow for larger or smaller deviations. This effectively removes fields with an abnormal histogram from the averaging, producing an artifact-free correction image. The MED and MAD values are computed from a sample of N images from every ROA, and a correction image is not produced when the number of artifact-free fields falls below 20. The correction image from the nearest ROA is used to correct problematic ROAs.

Stitching

Tile pairs in 2D are identified based on the corresponding row and column indices in the file name. Point matches are then sought in the overlap region between tiles. Alignment using a translation model in BigFeta then produces a *montage*, i.e. a stitched full image of a ROA.

---

[4] https://github.com/AllenInstitute/render-python

[5] https://github.com/AllenInstitute/BigFeta

3D rough alignment

Montages of adjacent sections were first roughly aligned to find tile pairs in neighboring ROAs. Point matches are found in Gaussian downsampled single images of montages that are rendered to disk at 5% of the original image scale. A filtering step is then performed to remove false point matches that are found on the border of the ROA. The alignment between downsampled montages is then solved, which produces a roughly aligned stack in render-ws. The transformations from this stack are then applied to the full-scale data, creating a montaged, roughly-aligned stack.

Fine alignment

Alignment proceeds by iterating through the z-levels, and looking at the first neighboring ROAs, sampling a cone with a fixed radius to find overlapping tiles in z. Point matches are then sought in z for every tile pair. Since tiles are likely to overlap only partially, each tile has multiple neighbors in z. By visual inspection, we found that typically the rough alignment has an accuracy higher than a single field. With perfect alignment, the maximum number of overlapping neighboring tiles is 6 for any possible rotation and translation of the section. For any finite precision the search radius has to be increased to find all neighbors, but with the accuracy of the rough alignment it is expected to be 9 tiles. A cone radius of 0.1 times the tile size Table 1 yields a number of potential image pairs approximately 2 to 2.5 times the total amount of tiles. A larger cone radius will increase the amount of possible tile pairs and therefore will yield more matches, but this significantly increases the computation power needed (4x for a cone size of 1). Nonetheless, a 0.1 cone radius was sufficient to find a large number of point matches. For instance, in the MCF-7 cell datasets, approximately 40-50% of image pairs yielded matches, being roughly equal to the total amount of tiles. The alignment is then solved on the full set of intra-ROA and inter-ROA point matches, for an affine similarity transformation model, with weights given to the intra-ROA and inter-ROA matches, respectively. Regularization parameters for the transformation model were determined empirically.

Export

The aligned data is exported to a self-managed instance of WebKnossos [139] using the render-ws client. The data format is reduced to unsigned 8-bit and saved in .wkw format (WebKnossos data format). Segmentations are saved as 16-bit or 32-bit layers.

Realignment with SOFIMA

Fine aligned datasets in WebKnossos were realigned with optical flow following the approach by [68] on a single NVIDIA Tesla P100 GPU with 12 GB memory, using customized scripts [6]. Optical flow is implemented as Scalable Optical Flow-based Image Montaging and Alignment (SOFIMA) [7]. The data sets were first cropped to a continuous volume in WebKnossos by applying a minimum projection to the full stack followed by an Otsu threshold operation. Flows were then computed from patches of 160 pixels and stride 40 on 16 nm, 32 nm and optionally 64 nm / pixel downsampled resolutions of the data. Flow fields were filtered to remove outliers. The filtered flow fields were reconciled for

---

[6] 10.5281/zenodo.12733905

[7] https://github.com/google-research/sofima

each position using the highest resolution flow estimate available, and the final flow was upsampled to the original resolution of the data (4 nm / pixel). A deformable mesh with Hookean springs was then fitted to the upsampled flow field. Finally, the full resolution data was warped according to the optimized mesh and exported to WebKnossos.

4.4.6 Mitochondria segmentation

Ground truth (GT) annotations of individual mitochondria were generated for the rat pancreas and MCF-7 cell dataset using the annotation tools in WebKnossos, on the originally aligned data. Mitochondria were identified based on their characteristic shape and presence of cristae, and were annotated if they were present in multiple z slices. Annotations were proofread by a second annotator. The GT for the SOFIMA alignment was obtained by warping the original annotations according to the deformable mesh optimized to the flow field of the data. Mitochondria instance segmentation was performed with MitoNet [287] on data downsampled to 16 nm / pixel resolution. First, optimal MitoNet parameters for 3D instance segmentation were determined using the 2D inference tool in the empanada-napari plugin. The model was neither finetuned nor retrained using ground truth annotations of FAST-EM data. For evaluation, the MitoNet predictions were first filtered to remove all mitochondria instance predictions for which no GT equivalent existed (in case of sparse annotations), while retaining all predicted pixels for the instances for which a GT equivalent existed to properly determine the IoU scores. Predicted and ground truth instances were matched using the Hungarian algorithm. IoU, F1, F1@50, F1@75, AP@50 and AP@75 scores were then calculated. For the rat pancreas, annotations consisted of two subvolumes, for which a weighted average was computed based on the number of predicted pixels in each volume.

Author contributions

B. H. Peter Duinkerken, Daan van Beijeren Bergen en Henegouwen, Cecilia de Heus, Anouk H. G. Wolters prepared the samples for array tomography. Daan van Beijeren Bergen en Henegouwen assisted the acquisitions with FAST-EM. The software for 3D reconstruction was co-developed with Ryan Lane and Tibbe Höppener. Cecilia de Heus and B. H. Peter Duinkerken helped with generating and proofreading the ground truth annotations of mitochondria. Nalan Liv, Ben N. G. Giepmans, and Jacob P. Hoogenboom supervised the research and secured funding. We also thank Michal Januszewski from Google for his help with the implementation of SOFIMA.

Data and software availability

The full 3D datasets as presented in this article can be viewed through Nanotomomy.org (`http://www.nanotomy.org/OA/Kievits2024MIM/index.html`). The full raw datasets are available for download through EMPIAR (entries EMPIAR-12174, EMPIAR-12190 and EMPIAR-12193). The code to generate the 3D reconstructions presented in this article and a sample dataset are available through the 4TU.ResearchData repository (doi: `https://doi.org/10.4121/bf3f2b23-2328-4d81-a0f4-05fdb33117d7`). The scripts used to analyze the MitoNet results (Table 2) and generate the views in Figure 6 and Figure A5 are available on Github: `https://github.com/hoogenboom-group/Kievits-FASTEM-array-tomography-2024`.

4.5 Supplementary material

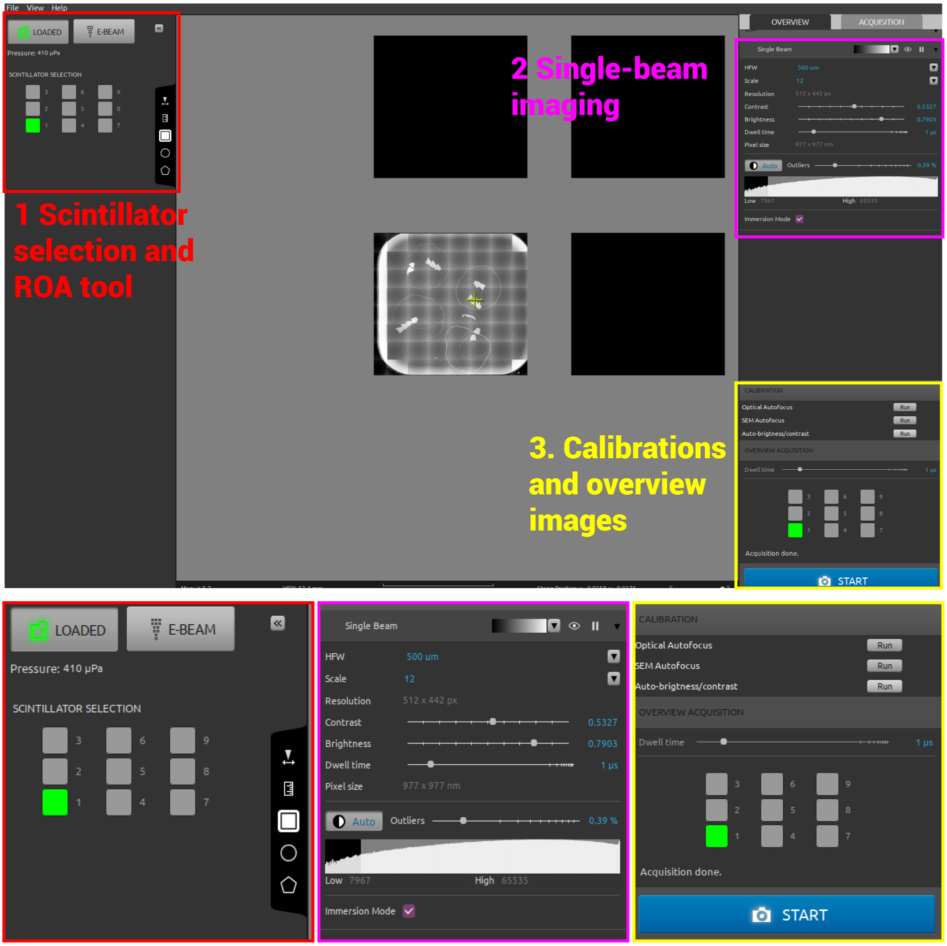

1 Scintillator selection and ROA tool

2 Single-beam imaging

3. Calibrations and overview images

Pressure: 410 µPa

HFW 500 um

Scale 12

Resolution 512 x 442 px

Contrast 0.5327

Brightness 0.7903

Dwell time 1 µs

Pixel size 977 x 977 nm

Outliers 0.39 %

Low 7967 High 65535

Immersion Mode ☑

OVERVIEW ACQUISITION Dwell time 1 µs

Acquisition done.

Figure A1: ODEMIS FAST-EM graphical user interface, overview tab. 1: Scintillator selection and ROA definition tools. 2. Single-beam tool. 3. Optical calibration, detector (single-beam) settings, overview image settings.

Table A1: Estimated reconstruction times for FAST-EM of a 500 x 500 x 50 μm^3 volume from 500 serial sections.

Post-processing step	Compute time	Unit
Post-correction	90.05	h
Import	50.88	h
Stitching	139.60	h
Rough alignment	0.19	h
Fine alignment	734.72	h
Export	300.18	h
Total	1315.63	h
	54.82	days

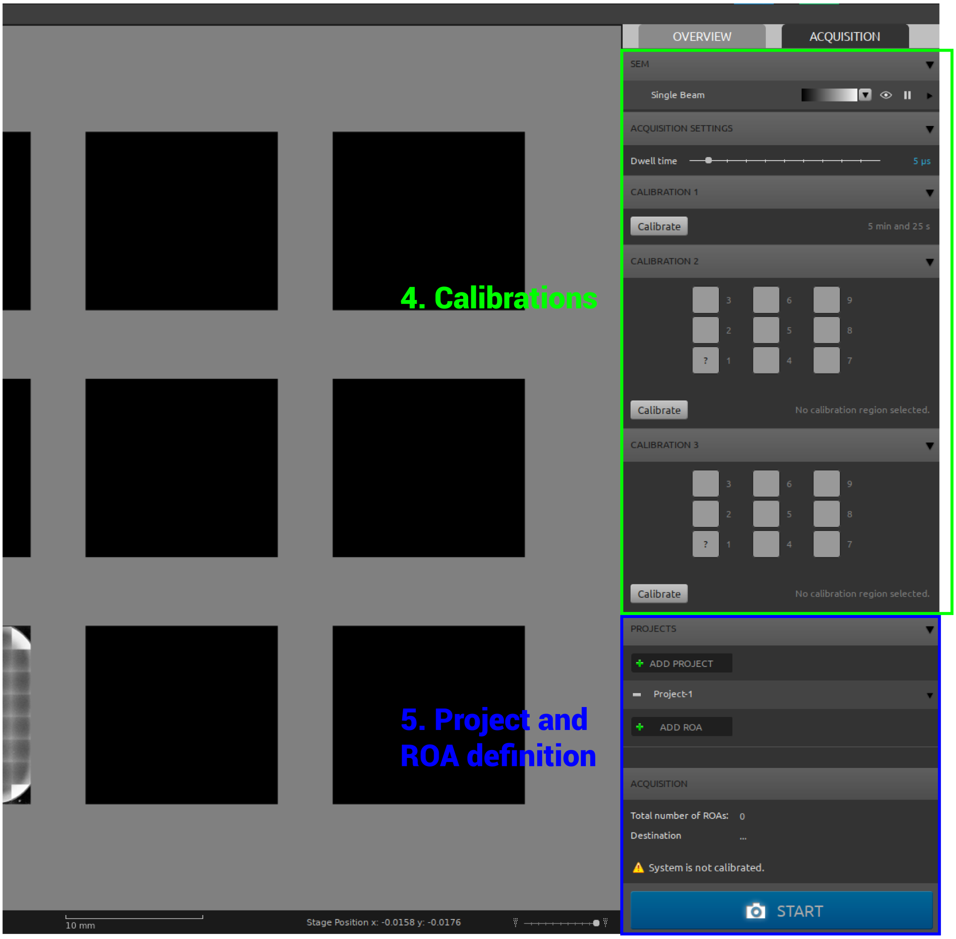

Dwell time 5 µs

Calibrate 5 min and 25 s

Calibrate No calibration region selected.

Calibrate No calibration region selected.

Total number of ROAs: 0

Destination ...

System is not calibrated.

Stage Position x: -0.0158 y: -0.0176

Figure A2: ODEMIS FAST-EM graphical user interface, acquisition tab. 4. Calibration step settings. 5. Project and ROA settings.

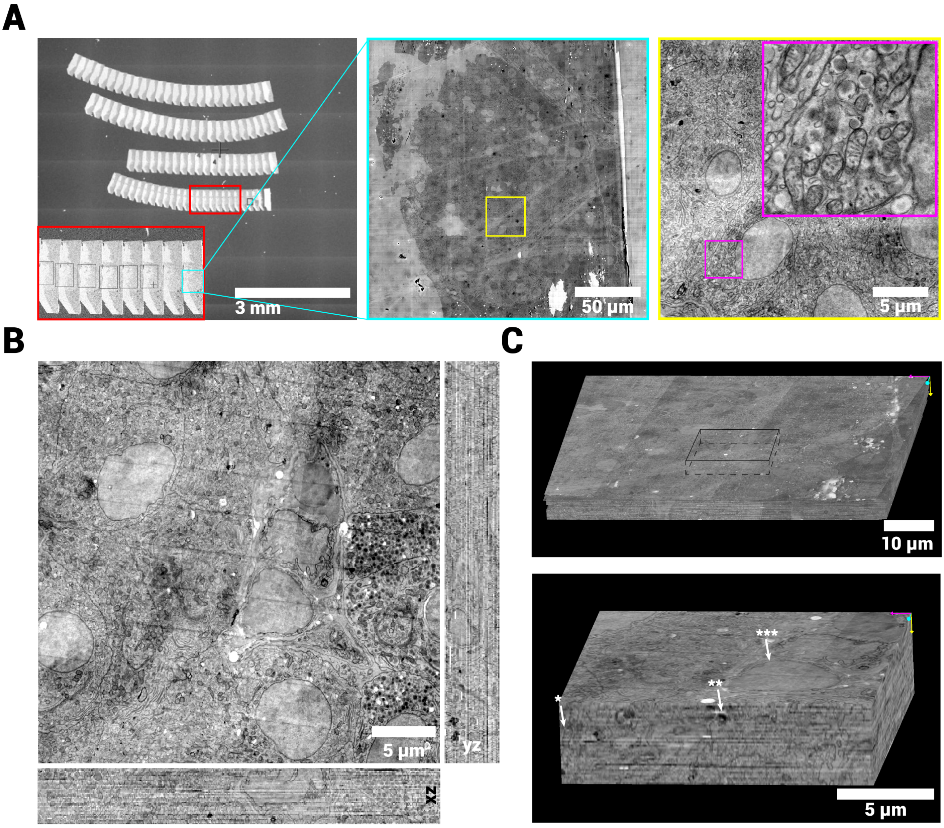

Figure A3: vEM reconstruction of an islet of Langerhans in rat pancreas tissue. **A**: Overview images of sections, showing a zoom in on a single ROA, a single field and a single cell respectively. **B**: Aligned volume reconstruction from 44 100nm serial sections showing the orthogonal reslices through the center of the stack (xz and yz). **C**: Volume rendering of the full (continuous) stack. Inset shows smaller subvolume at 8nm/pixel resolution with arrows pointing at structures of interest (Star indicators: *=Mitochondrium, **=Lysosome, ***=Nuclear membrane). The data quality and alignment is consistent throughout the stack. The full dataset is available via Nanotomy.org

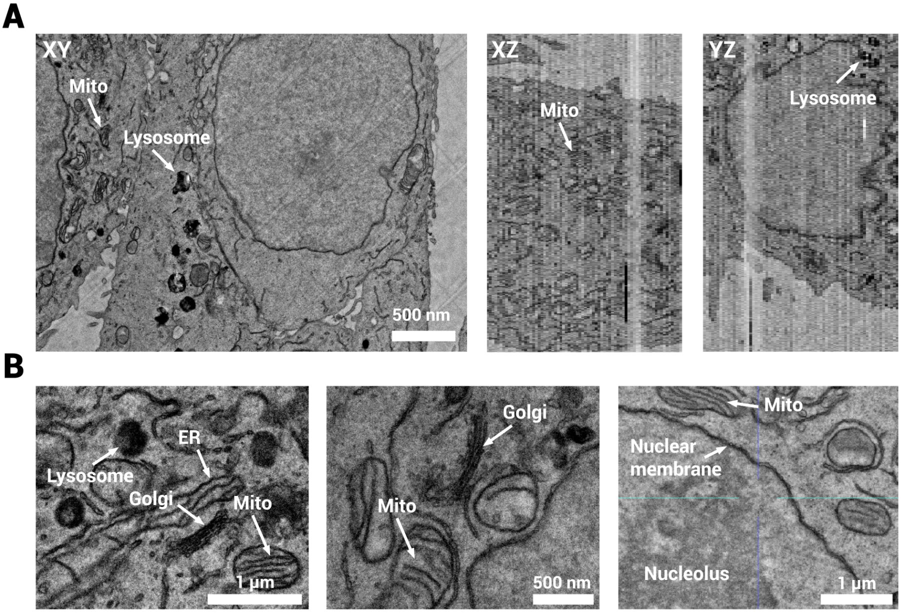

Figure A4: FAST-EM resolves organelle structures. **A**: xy, xz and yz planes of data in Figure 5C at 8nm/pixel resolution. The axial resolution (100nm) and fine alignment allow identification of organelles in xz and yz planes. **B**: High resolution crops of MCF-7 cells stained with uranyl acetate (see Table 1 for details). Several organelles are indicated with arrows. FAST-EM resolves the detailed structure of several organelles, including mitochondria cristae, stacked golgi membranes, double membranes. The full dataset is available via Nanotomy.org

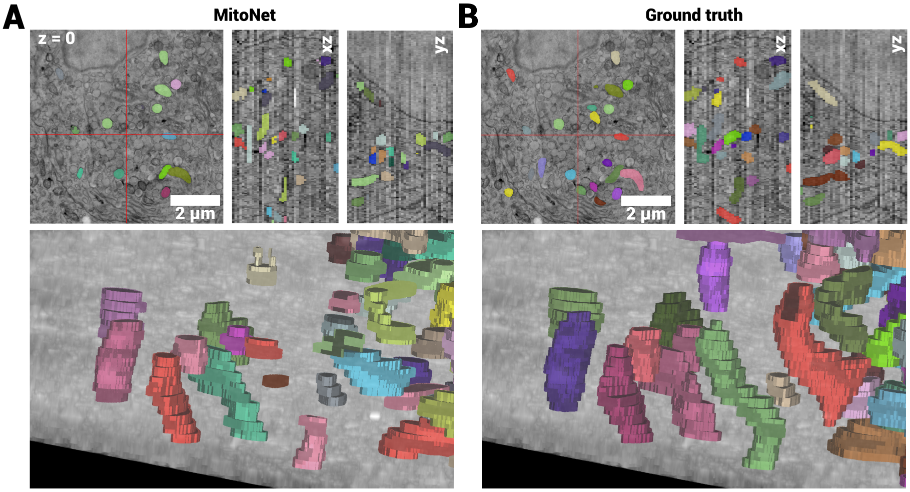

Figure A5: Automatic instance segmentation of mitochondria in FAST-EM data of rat pancreas using MitoNet. **A**: MitoNet predictions on subset of data, showing the orthogonal slices at the locations indicated by the red cross, and 3D renderings in Napari. **B**: Ground truth annotations of mitochondria from the same volume. The predictions show qualitative reasonable overlap with the ground truth. The full dataset is available via Nanotomy.org

A

Fixed overhead time - acquisition set up	**Time (s)**
Optical calibrations (2x)	80
Overview images (500ns)	333
Focusing / correcting astigmatism SEM	90
Determining calibration locations	90
Calibration step 1	240
Calibration step 2	108
Calibration step 3	300
Defining first ROA	120
Total	**1361**
Overhead per field	
Stage translation	0,52
Other overhead	0,45
Overhead time per section / acquisition	
Optical calibration	52
Defining additional ROAs, manual verification (per section)	68
Focusing per run (5-10 sections)	90

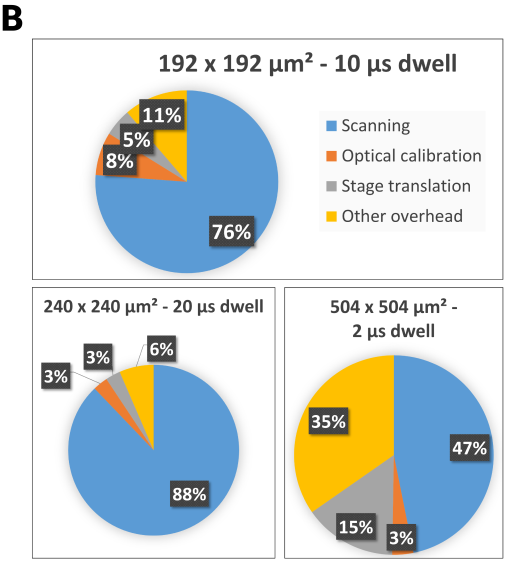

Figure A6: A: Set up, per-field and per-section overhead times for FAST-EM. B: Time spent on scanning and overhead, relatively, for acquisitions in this paper and a large volume. For the dwell times considered here, the acquisition time is mostly limited by the scan speed.

5

Artifacts in single- and multibeam OSTEM detection

Artifacts are frequently encountered in electron micrographs of biological tissue and cells. Biological samples have to undergo rigorous preparation to be resistant to vacuum conditions and electron beam exposure. Knowledge about the appearance of image artifacts and how they arise is crucial for their recognition and mitigation and for proper image interpretation. How artifacts appear depends strongly on the electron detection modality and the imaging conditions. Optical scanning transmission electron microscopy (OSTEM) is a new detection technique, compatible with single-beam and multibeam electron microscopes, in which tissue samples are directly deposited on a scintillator for imaging in transmission mode. Here, we identified several types of artifacts that may occur in single-beam and multibeam OSTEM detection. These artifacts arise or appear as a result of combining existing sample preparation protocols with solid scintillator substrates and optical transmission detection. Through investigation it is further shown that artifacts can be effectively mitigated or minimized to ultimately enable high quality large-scale 2D and 3D acquisitions.

5.1 Introduction

Artifacts are common in electron microscopy (EM). The sample has to meet several requirements for successful imaging with an electron beam, such as resistivity to high vacuum conditions and electron radiation damage. The appearance of image artifacts may complicate the interpretation, as they may alter or obscure the native structure of the sample. Thus it is crucial to recognize and understand the origin of artifacts, in order to prevent them or limit their effect on interpretation.

A very common cause of artifacts is sample charging. Charging of insulating samples may lead to image contrast differences and distortions. Negative charging may induce strong local fields and eventually lead to electric breakdown, which can damage the sample [297]. How these charging artifacts appear in the image may be further influenced by the sample geometry, tilt angle and used imaging conditions, which affect the total electron yield [298].

Additionally, sample quality may suffer from radiation damage. Heating by the electron beam may lead to melting, deformation or thermal decomposition. However, most radiation damage is caused by ionisation (carbon bond-breaking). In organic samples, this results in the formation of carbon double bonds [298]. During this process, the specimen may also shrink or deform. Bubbles may form under high intensity radiation (i.e. in transmission EM) by volatile fragments that escape the specimen. Finally, contrast differences can be created through contamination by hydrocarbon molecules on the specimen surface.

Sample charging, damaging and contamination in EM have been intensively investigated, which has led to strategies for optimizing imaging conditions to control, mitigate or prevent them altogether [299, 300, 301, 302, 303, 63, 120, 304]. Additionally, the understanding of artifacts has led to the development of exquisite preparation protocols to preserve the natural structure of the sample as best as possible. This holds especially true for samples of biological nature, as they are naturally insulating and sensitive to electron-beam irradiation. As a result, biological sample preparation protocols generate artifacts, which in turn have been extensively documented as well [305, 306]. Traditionally, samples are first fixed to preserve the ultrastructure, which may shrink and distort structures in comparison to cryo-fixation. They are then treated with heavy metal salts for further preservation, enhancing contrast and increasing conductivity. This step may result in staining gradients and aggregations or precipitations of heavy metal complexes. Then, the samples are dehydrated and embedded in plastic resins to maintain their structural integrity during specimen preparation (sectioning) and subsequent imaging. Common artifacts during these steps arise from tissue shrinkage, lipid extraction, compression and the formation of cracks during resin curation. In several techniques, the sample must be physically sectioned. This typically leads to artifacts as section compression, warping, folding, knife marks and thickness variations.

Conventionally, an electron microscopist would distinguish artifacts from structures native to the specimen, and circumvent them by imaging an artifact-free region in the sample. Modern EM techniques allow imaging of large areas or volumes, commonly known as large-scale EM [307] and volume EM (vEM) [2]. Because these techniques typically produce large datasets, artifacts will inevitably be included. This approach may also be preferred over single images since it gives an unbiased view of the sample. How and whether artifacts appear in the datasets may ultimately be determined by the type of electron microscope, the mode of operation and the detection scheme.

Novel EM techniques and detection schemes have been developed to increase throughput in large-scale EM and vEM [264]. For example, multibeam scanning EM uses multiple beams in parallel to scan the sample, thereby increasing the scan speed. Multibeam scanning EM has motivated the use of optical tranmission detection (OSTEM) [26, 28], since it is more straightforward to separate the signals than in detection schemes based on secondary electrons [60]. However, such a detection scheme may also reveal or lead to (new) artifacts. Optical transmission detection is less sensitive to sample charging than secondary electron detection due to the higher energy of the primary and transmission electrons. As opposed to other scintillation-based detectors (e.g. Everhart-Thornley), the electron beam interaction volume with the scintillator substrate in OSTEM is tightly confined to a small region. Thus, the sample-substrate boundary, the coating layer and scintillator surface are also revealed.

Here, we investigate artifacts that appear as a result of combining single-beam and multibeam OSTEM detection with conventional biological sample preparation protocols for large-scale imaging and a scintillator-based solid substrate. Multibeam OSTEM is implemented in FAST-EM, a commercially available multibeam scanning EM. The artifacts as investigated here typically do not appear in array tomography studies which combine solid substrates with backscattered (BSD) or secondary electron (SE) detection schemes. It is shown that multibeam scanning and optical detection can introduce specific artifacts and that these may be aggravated by image processing. Lastly, procedures are presented to minimize or mitigate these artifacts in future experiments.

5.2 Optical transmission detection visualizes artifacts

In OSTEM, ultrathin biological sections are placed on a thin film-coated scintillator substrate, which converts transmitted electrons into photons. These photons are collected by a high NA optical objective and projected onto a multipixel photon counter (Figure 1). In BSD and SE detection schemes, the interaction volume of the beam is typically confined to the section [308, 268] (Figure 1A), to maximize tissue contrast. When the electron beam landing energy is increased, the beam starts to penetrate into the underlying substrate. In EM techniques where solid substrates are used to support the sections, this reveals its underlying structure, leading to deteriorated image contrast [268, 309]. In OSTEM, the interaction volume extends into the coating and scintillator. Any features between the substrate and sample and elevations in the substrate profile that have transmission contrast therefore become visible (Figure 1B). Contrast differences generated by inhomogeneities in the coating and substrate are directly superimposed on the tissue contrast. The transmission signal may also be modulated or blocked by electron-dense features in and on top of the sample.

In multibeam OSTEM detection (FAST-EM), there are additional effects that must be taken into account. The scan area between adjacent beamlets must overlap to ensure no sample area is missed and to reconstruct a single composite image from the multiple beams. As a consequence, some areas in the sample are exposed twice, or even four times. This leads to differences in the transmission signal between overlapping and non-overlapping areas and thus contrast differences in the composite image (Figure 1C), which necessitates correction. Furthermore, the signal from one beam may influence that of neighbor-

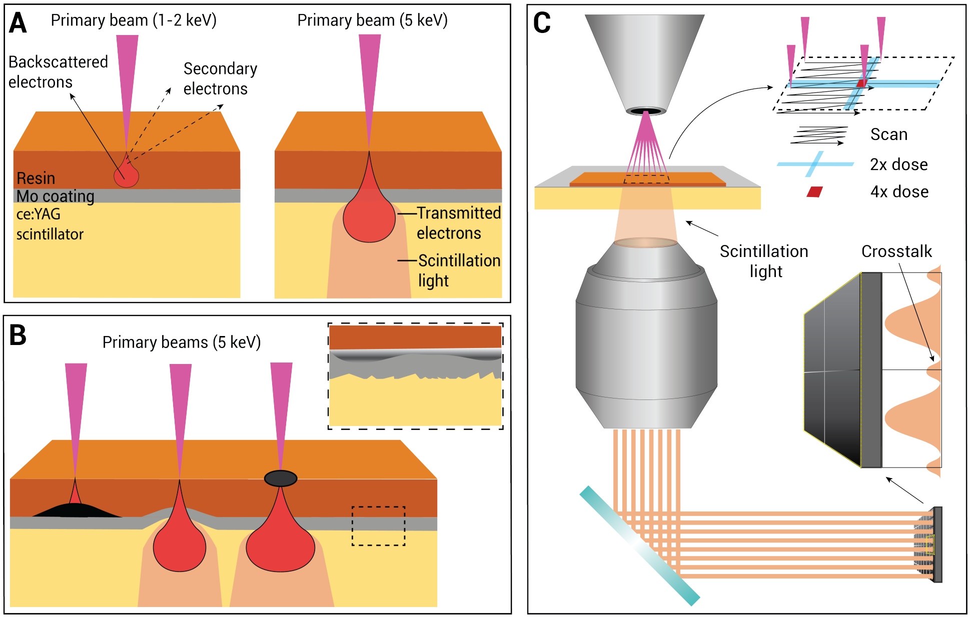

Figure 1: OSTEM detection scheme and artifacts. **A:** For low landing energies (1-3keV, depending on the section thickness), the interaction beam is typically confined to the section. In OSTEM, the interaction volume extends further into the coating and scintillator, thus revealing the underlying substrate variation. **B:** Multibeam OSTEM detection, illustrating four kinds of possible artifacts: (1) the transmitted signal of one or more beams can be blocked by electron-dense features on the sample-substrate boundary; (2) variations in the substrate profile may be captured by the detection scheme; (3) increased scattering may broaden the interaction volume and optical spot, which may affect neighboring beams; (4) inhomogeneities in the coating layer and scintillator roughness may deteriorate the image quality. **C:** Parallel scanning may lead to contrast differences due to inhomogeneous electron fluences. Crosstalk between adjacent detectors may lead to image artifacts.

ing beams through crosstalk between signals detected by adjacent detectors. All aforementioned factors lead to distinguishable artifacts that will be discussed in the following sections.

5.3 Role of the substrate-sample interface

5.3.1 Artifacts on the substrate-sample interface

En bloc staining approaches are preferred in large-scale EM and vEM (Chapter 2). In correlative array tomography, however, heavy metal post-staining can be applied to the sections after fluorescence microscopy to enhance the image contrast for EM [47]. Thus, post-staining may be used to further enhance tissue section contrast in FAST-EM, if combined with correlative techniques that require preservation of fluorescence.

Post-stained tissue sections imaged with OSTEM detection demonstrate artifacts with darker contrast than the surroundings (Figure 2A). These artifacts are not visible in sections from similar tissues prepared with *en bloc* staining (Figure 2B). Interestingly, BSD at 1.5 keV landing energy does not reveal the precipates in the post-stained sections (Figure 2A), whereas increasing the landing energy of the beam to 5 keV did (Figure 2C). Moreover, the artifacts are not observed outside of the section on the substrate, although the staining solution is applied there. This implies that the artifacts are formed on the section-substrate boundary and not in the tissue section. We rationalize that these artifacts are thus created by residual staining solution that is trapped under the section by capillary force.

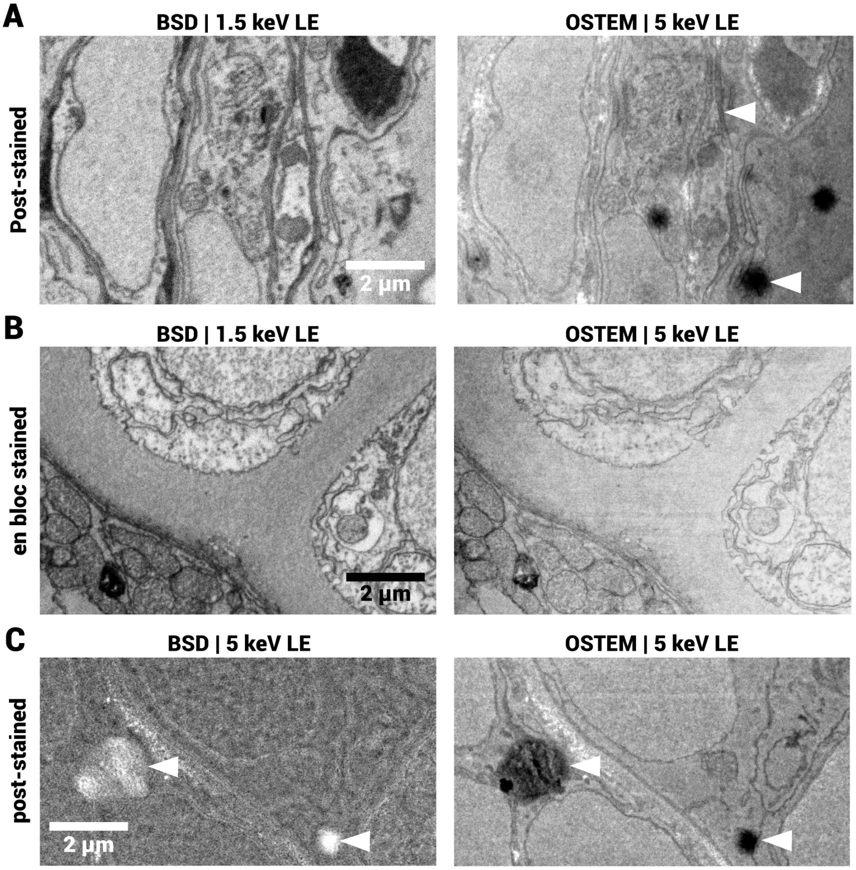

Figure 2: Post-staining introduces artifacts in OSTEM. **A**: BSD and OSTEM images of 80nm thin sections of zebrafish larva post-stained with 4% neodymium acetate. **B**: BSD and OSTEM images of 80nm thin sections of zebrafish larva *en bloc* stained with 4% neodymium acetate. Arrows indicate artifacts that are present in OSTEM image, but not in BSD image at 1.5 keV landing energy. **C**: BSD with the same landing energy as OSTEM (5keV), now revealing the same artifacts (indicated by arrows), although the contrast mechanism is compromised due to the suboptimal landing energy.

Post-staining artifacts may be prevented by putting the sections onto a droplet of staining solution, then washing the sections and subsequently transferring them to the scintillator substrate. However, this only works for individual sections and small ribbons, since they have to be transferred with a loop. This process is also more error-prone than on-substrate staining and may thus generate additional artifacts. A full conformal contact

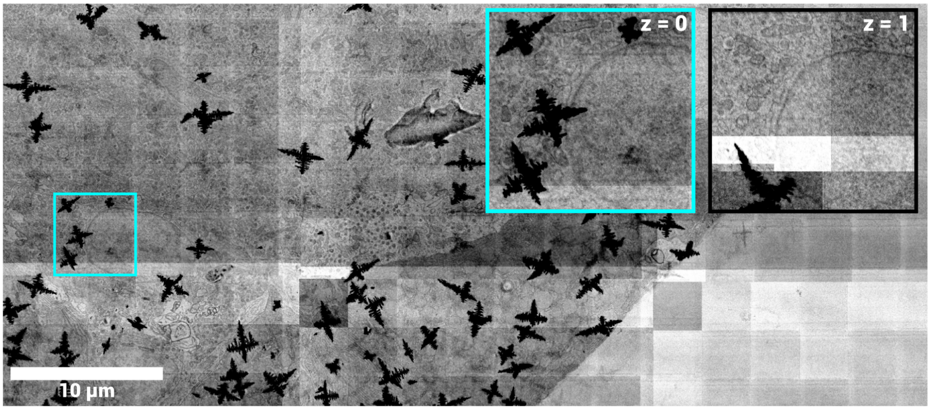

Figure 3: Electron-dense precipitates in large scale acquisitions. Precipitates obscure ultrastructural details, but are not continuous in serial sections, indicating that they form after sectioning. Rat pancreas was prepared with the rOTO protocol and uranyl acetate. Images are unprocessed. Cyan inset shows endocrine tissue. The right panel shows the same region as the inset, but in the adjacent serial section. Full dataset can be viewed through WebKnossos.

between the sections and the substrate may reduce or prevent these artifacts.

5.3.2 Interaction of the coating layer with the sample

Molybdenum nanofilms have useful properties, such as good adherence to glass, high electrical and thermal conductivity, dimensional stability and corrosion resistance [310]. The thin molybdenum film used as a coating of scintillators has two additional functions in OSTEM image formation, apart from providing electrical conductivity. The coating acts as a spacer between the sample and the scintillator. Electrons traveling through the coating layer scatter further before they interact with the scintillator, which increases the interaction volume and may therefore reduce saturation (Chapter 3). Moreover, the metallic coating is reflective, a property which may aid in enhancing the signal collection because photons that are emitted towards the scintillator surface are (partially) reflected towards the objective lens.

The nature and composition of the molybdenum thin film surface depends on the medium (air, aqueous), pH and processing parameters (temperature, pressure) [311]. We observed specific electron-dense precipitates in pancreas tissue prepared with reduced osmium-thiocarbohydrazide-osmium (rOTO) protocol (Figure 3) on scintillators that had been stored for prolonged time. The sections were picked up from the knife bath using a loop and then deposited on a droplet of water put on the scintillator (Chapter 3). The precipitates resembled fractal-like structures which are typically created by diffusion limited aggregation. This may be caused by a reaction between the coating layer and a compound in the sample preparation protocol, possibly mediated by the aqueous medium. We addressed whether the precipitates were formed on the sample-substrate boundary and attempted to determine the elemental composition using energy-dispersive X-ray spectroscopy (EDX).

High-magnification images indicated that the precipitates are located both on top of and under the section (Figure 4). In one sample, their structure is clearly distinguishable in SE images and they obscured the tissue ultrastructure (Figure 4A). In a different sample, images taken with the backscattered electron detector of the FAST-EM show distinguishable tissue ultrastructure on top of the precipitates and curving of the tissue section around the precipitate (Figure 4B). In the FAST-EM (transmission) image, the ultrastructure is obscured by the precipitate. The EDX signal of area scans (Figure 5) shows elevated X-ray counts (+20%) for molybdenum and lead in the precipitates, although it is not possible to distinguish between these elements because of overlap in the X-ray spectra for the M shell electrons. The shape of the precipitate can also be identified in the Al, Os and Y spectra, though here the counts are lower (-10%) in the precipitate area than for the surroundings. This may be because increased electron scattering in the precipitate reduces the X-ray yield in the underlying sample area or substrate. In conclusion, the precipitates are likely formed as a reaction between lead or molybdenum in the sample.

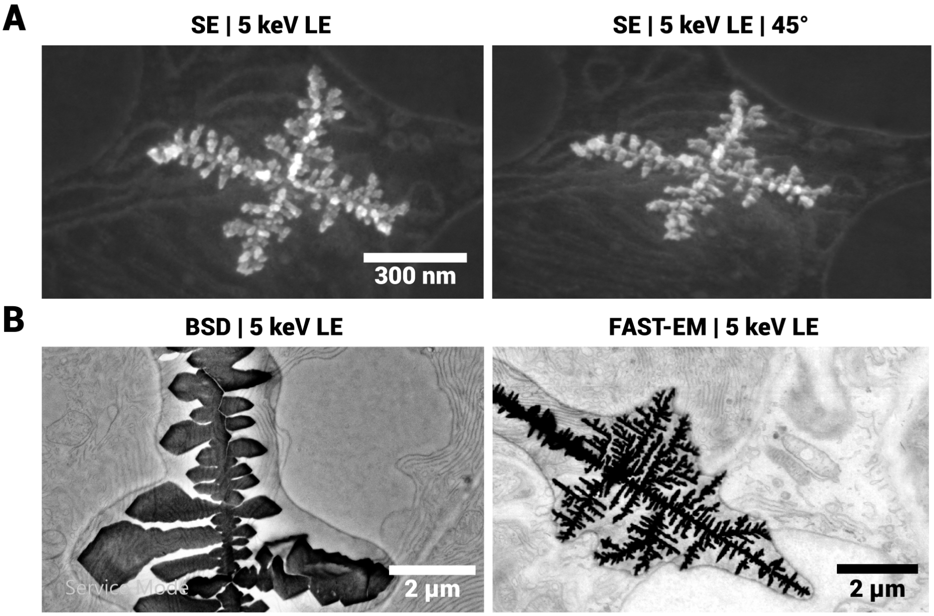

Figure 4: High magnification images of ectron-dense precipitates in different detection methods on top and under tissue. Different specimens were prepared with an identical protocol. **A**: Secondary electron (SE) images of electron-dense precipitates (Nova NanoSEM). Left panel: tilt angle of 0 degrees. Right panel: at a 45 degree tilt angle. **B**: Images of precipitates in FAST-EM, showing that the tissue section around the precipitates is curved. Left panel: single-beam backscatter electron image. Right panel: FAST-EM image.

The precipitates were not continuous in serial sections of the same sample (Figure 3). Therefore, they must form after embedding, likely during section deposition. The precipitates do not form when depositing sections on scintillators coated with a thin layer of chromium, or a single atomic layer of graphene (data not shown). Moreover, precipitates are mostly present in tissue and only very marginally in the surrounding empty resin (Fig-

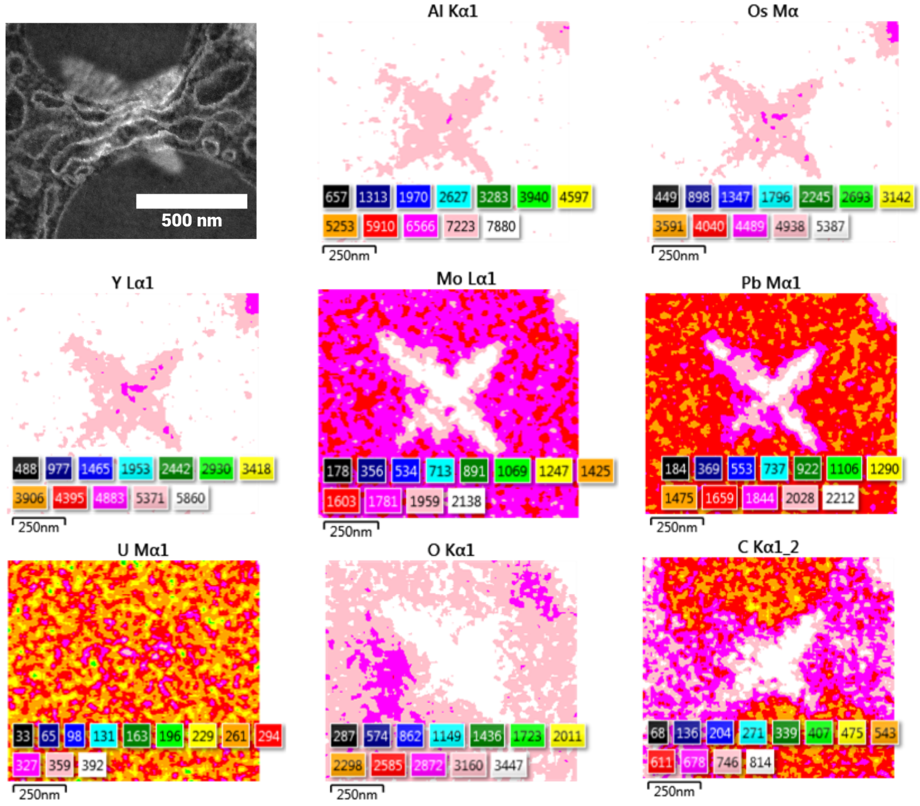

Figure 5: Energy-dispersive X-ray (EDX) analysis of electron-dense precipitates, showing that they contain lead or molybdenum. A secondary electron image shows the scanned area. The figures show X-ray counts for different elements in the sample and substrate. Data were acquired with a 10 keV beam, 1.4 nA beam current, 10 µs dwell time and averaging of 100 frames.

ure 3). Thus, a reaction with a compound in the resin seems unlikely. The precipitates do not form on the tissue sections when prepared according to the protocol for FAST-EM array tomography, where the scintillator is submersed in the knife boat and then dried by lowering the water level (Chapter 4). Neither are the precipitates observed in the cell specimens (Chapter 4), which were prepared according to a similar rOTO protocol at the University Medical Center Utrecht.

Based on these observations, we conclude that the precipitates form upon reaction of residues from the staining solutions and the molybdenum coating layer, possibilities being a reaction between molybdenum or molybdenum oxides and lead aspartate, or thiocarbohydrazide, which are compounds specific to the rOTO staining protocol. A modification to the rOTO protocol was made accordingly, based on the earlier observation that thiocarbohydrazide formed precipitates in solution (since it has limited solubility in water). Samples prepared with this modified protocol do not show any precipitates [312].

5.4 Solid substrate non-homogeneity

5.4.1 Substrate surface roughness, scratches and defects

Earlier work shows that quality of the substrate surface finish affects the image quality in OSTEM detection, notably the image contrast [27]. Datasets recorded with single-beam and multibeam OSTEM exhibited apparent differences in image quality. This variation in image quality is present even in datasets from multiple specimens prepared with identical sample preparation protocols. Therefore, we reasoned that the image quality is affected by variations in substrate quality, possibly resulting from differences between batches. To what extent the surface roughness impacts the biological contrast has not been quantified. Any surface defects which are comparable to or larger than the beam profile impinging on the surface (after transmission through the biological sample) will contribute to the image formation and thereby reduce the biological contrast. The total surface roughness of the substrate is a combination of the scintillator and coating roughness, and both will contribute to the background contrast in the transmission image. We therefore characterized uncoated as well as coated scintillators from different batches and suppliers and investigated whether the observed differences could be linked to the obtained biological image quality.

Surface scans of uncoated scintillators with atomic force microscopy (AFM) show varying roughness between batches and suppliers (Figure 6A-B). One scintillator (batch 1) exhibits a particularly high surface roughness, as well as numerous visible scratches and defects. A different scintillator from the same supplier (batch 2) shows lower surface roughness but still many apparent scratches. The scintillators from a different supplier (SPL), used in the experiments in Chapter 4, are of the highest quality, demonstrating little to no defects and near-atomic surface roughness.

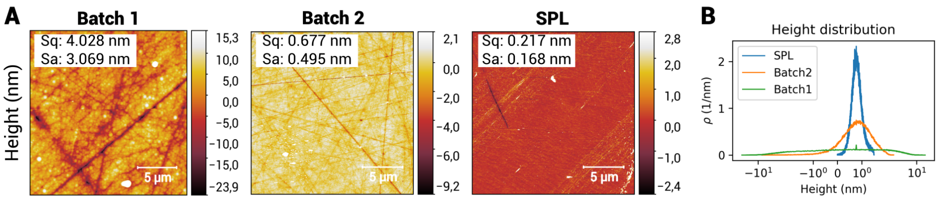

Figure 6: **A**: AFM measurements (20 µm field-of-view) of uncoated YAG scintillators from different batches and suppliers show varying roughness and surface quality finish. Surface roughness is measured as RMS roughness (Sq) and mean roughness (Sa). **B**: Height distribution of images in **A**. Scintillators from batch 1 and 2 demonstrate numerous surface defects such as scratches, whereas the SPL scintillator is free of large defects. AFM images were aqcuired on an Oxford Instruments/Asylum Research Cypher system, using Bruker Fastscan-A cantilevers. The imaging mode used was AC (tapping) mode, with drive frequency of approximately 1.5 MHz and oscillation amplitudes of 5-10 nm. Images were background corrected using a polynomial subtraction (a=3), then row aligned using the median. Sq and Sa values were computed after masking obvious dirt particles in the image with a simple height threshold.

Coated scintillators were imaged first characterized with SEM in SE detection mode. For SE imaging, the beam is focused on the substrate surface and an image is acquired with a small pixel size, thus directly revealing any nanoscale variations in the substrate profile. The results are compared to biological images taken from the same substrate, acquired with single-beam OSTEM detection. The coated scintillators with biological samples (subsequently referenced to as ”PD02” and ”PD11”) exhibit notable difference in SE contrast (Figure 7). Although both scintillators show a similar surface profile (supposedly the sputtered structure of the molybdenum film), PD11 shows apparent higher image contrast, which can be explained by stronger SE emission as a result of a rougher surface. The apparent biological image quality of PD11 is compromised with respect to PD02. In the image from PD02, small features such as the nuclear membrane and mitochondrial cristae can be discerned, whereas in the image of PD11 these features are less pronounced.

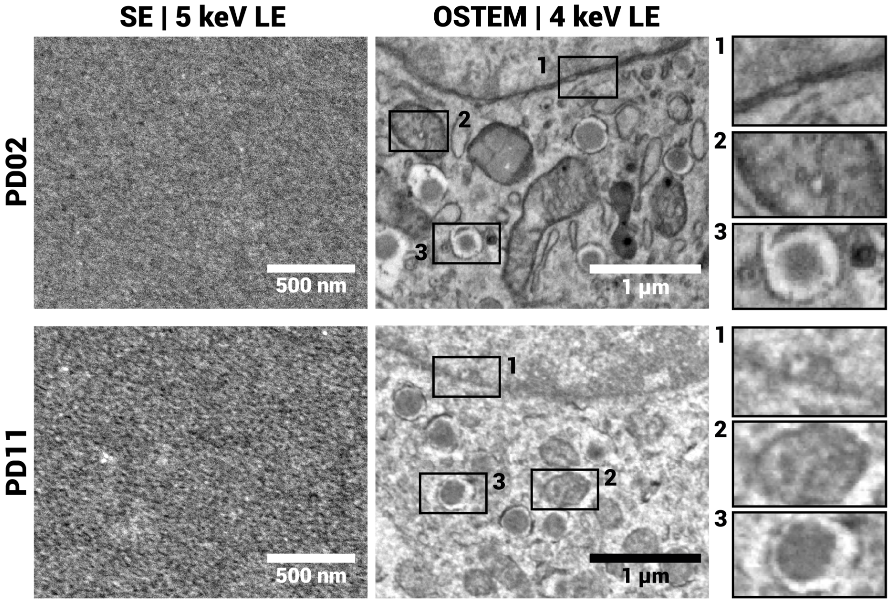

Figure 7: Secondary electron (SE) images of the substrate surface, and OSTEM images of biological samples, from two different scintillators (PD02 and PD11). The surface SE contrast is clearly increased for PD11, which translates to reduced contrast in the biological image (OSTEM). Insets show from top to bottom: a nuclear membrane, mitochondria (supposedly) and a granule. OSTEM datasets of rat pancreas on PD02 and PD11 can be viewed on WebKnossos (PD02 and PD11). SE images were acquired with a 5 µs dwell time, OSTEM images with a 10 µs dwell time (PD02) and 20 µs dwell time (PD11), respectively.

The surface roughness was determined by AFM for the PD02 and PD11 scintillators as well as two different coated scintillators (”SPL” and ”Delmic”), which did not undergo biological specimen preparation (Figure 8A-B). Prior to these experiments, the supplier (Delmic) improved their scintillator processing procedure to reduce the variability in surface roughness between scintillator batches. The ”Delmic” scintillator was taken from the latest batch received by TU Delft from the supplier and therefore represents the optimized substrate quality. The surface roughness varies signficantly between scintillators as shown by the height distribution (Figure 8C). Autocorrelation plots of the surface show apparent larger scale variations in PD11 and PD02 but not for the ”SPL” and ”Delmic” scintillators (Figure 8D). The highest surface roughness is found, as expected, for the PD11 scintillator

(Sq: 5.04-5.51 nm, Sa 4.34-4.06 nm). Notably, the PD02 scintillator has a twofold reduced surface roughness compared to PD11 (Sq: 2.64-2.36 nm, Sa: 2.12-1.80 nm). The "SPL" and "Delmic" scintillators have the lowest surface roughness (Sq: 0.28-0.44 nm, Sa: 0.22-0.35 nm, Sq: 0.47-0.57, Sa: 0.37-0.45 respectively), as well as the lowest maximum peak heights ("SPL": 2.20 nm, "Delmic": 1.82 at 2 µm field-of-view). These scintillators also do not show any scratch marks, indicating that their surface polishing is better. Scintillators from the same batch have subsequently demonstrated high biological image quality ("SPL": Figure 5, "Delmic": Figure 15).

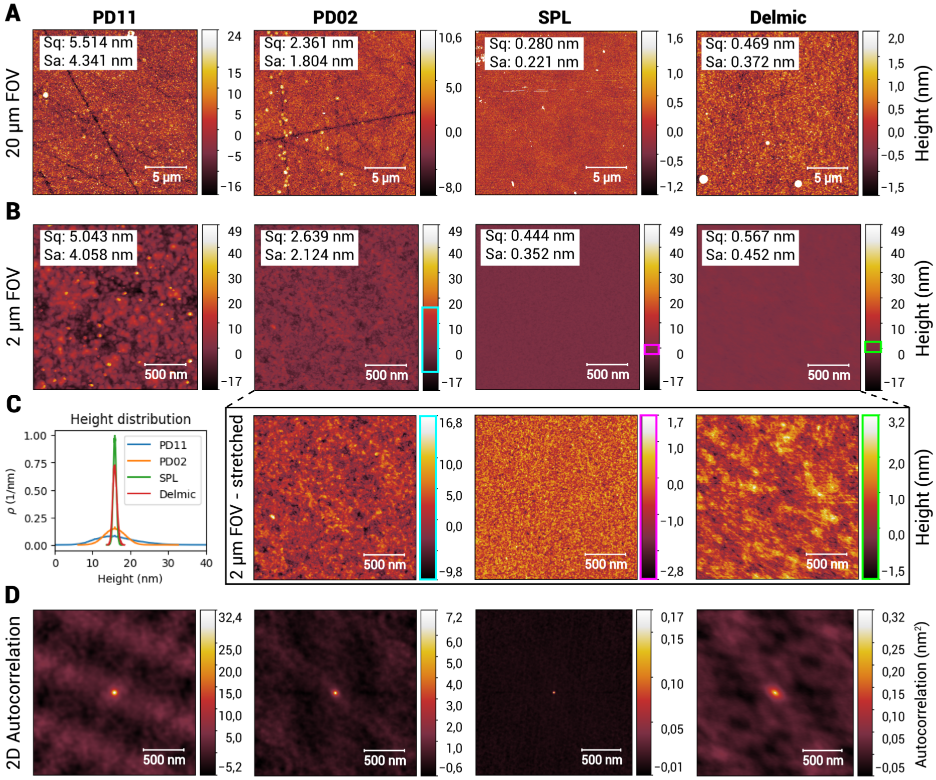

Figure 8: AFM measurements of molybdenum-coated YAG scintillators, showing a link between biological image quality and substrate roughness as well as an improved surface finish of supplied substrates. Scintillators were compared from different batches and suppliers, with biological specimen (PD02/PD11, Figure 7) and without (SPL/Delmic), as shown in the order of acquisition from left to right. Coated scintillators demonstrated varying roughness, with the SPL and Delmic scintillators having the lowest roughness. **A**: 20 µm field-of-view; **B**: 2 µm field-of-view, at same intensity scale as PD11. Inset shows intensities at full scale. **C**: Height distribution of images in **B**. **D** 2D autocorrelation of images in **B**. Images were acquired and processed as described previously. *Sq*: RMS roughness; *Sa*: mean roughness.

The 2 µm FOV scan of the SPL scintillator (Figure 8C) represents the texture of the molybdenum coating, as the image is apparently similar to the SE images of PD02. The roughness of the molybdenum coating can be estimated as the difference between the uncoated and coated SPL scintillators. For a single measurement, this corresponds to 0.063 nm Sq and 0.053 nm Sa. The 2 µm FOV scans of ”PD11” (Figure 8B) and ”Delmic” (Figure 8C) do not show this detailed surface structure.

We excluded the effect of sample preparation on the variation in OSTEM image quality by acquiring BSD images with increasing landing energy from 1.5 to 4 keV (Figure 9). This range of energies probed an interaction volume that would be confined to the biological section at energies lower than 3 keV and extended into the coating and scintillator for energies between 3 and 4 keV. The apparent contrast and image quality is similar for both samples at lower beam energies. The contrast is highest at 2 keV, and diminishes with increasing energies. A more apparent degradation of contrast is observed for tissue on PD11 as compared to PD02 from 3 keV and higher, most notably in homogeneous regions such as nuclei and empty resin.

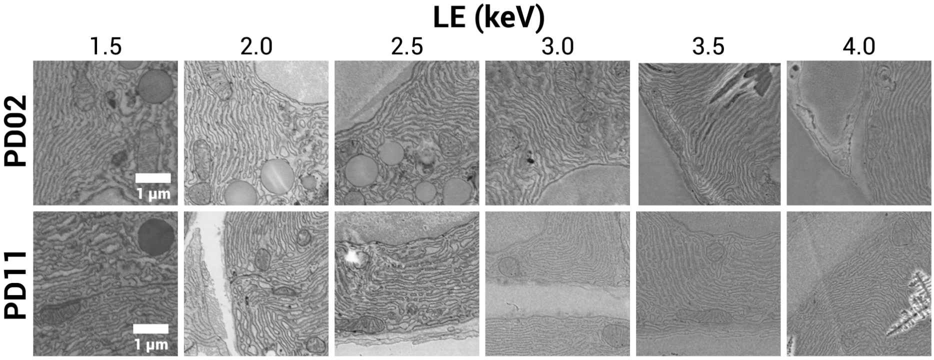

Figure 9: Biological image contrast in backscattered electron detection (BSD) as a function of electron landing energy (LE) for PD02 and PD11 scintillators. The image contrast is apparently similar for lower landing energies, but degrades more quickly for PD11 upon increasing the landing energy.

5.4.2 Coating quality

For high quality specimen preparation in array tomography, a homogeneously sputtered coating stable to prolonged water exposure is required. Thus, the coating should adhere well to the scintillator surface and have low reactivity with water or air. The thin film coating properties are dependent on the radio frequency sputtering conditions, such as the argon pressure and radio frequency power [313]. A low quality film may be a result of poor adhesion to the surface, which may be affected by film stress [314], surface roughness [315], surface contaminants [316] and particle contamination induced by the sputtering process [317]. Molybdenum thin films are known to oxidize at room temperature in exposure to (moisturized) air [318, 319, 320, 321]. Furthermore, the film properties may change by a reaction with compounds in the specimen, as discussed earlier.

High quality sputtered molybdenum films appear as homogeneous grey, reflective surfaces. They retain this appearance even after being submersed for prolonged time in the water bath during sectioning (Figure 10, left). However, the coating of some scintillators changed appearance after specimen preparation. One example where the coating seems

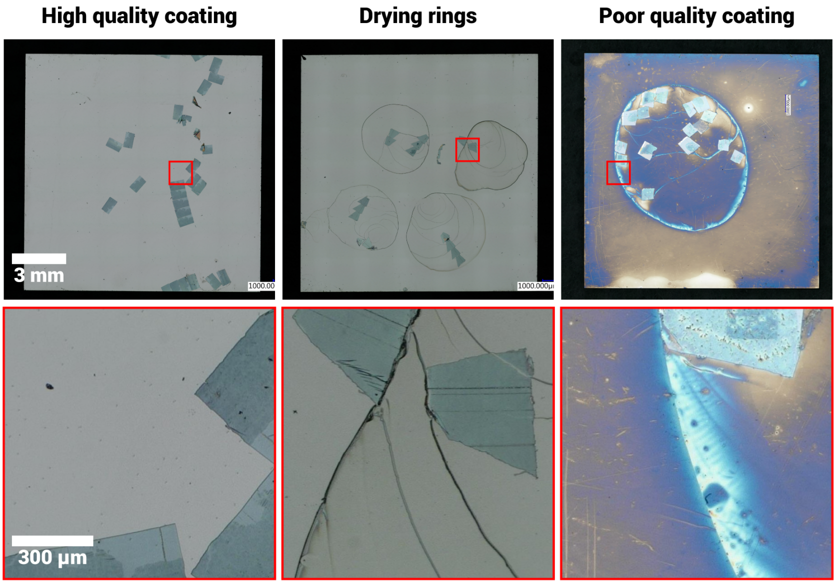

Figure 10: Scintillators with molybdenum films affected by specimen preparation, indicating poor sputtering quality. Left: scintillator with coating which is apparently unaffected by the sample preparation, since the molybdenum layer is not changed in appearance. Middle: scintillator with coating which is clearly changed by the sample preparation or exposure to air or water. Right: scintillator which shows drying patterns where the water was in contact with the coating. Images were acquired with a Keyence VHX-6000 digital microscope at 100x magnification in epi-illumination mode.

affected by water exposure, is the formation of drying rings (Figure 10, middle). Several scintillators lost their grey reflective appearance and became more transparent (Figure 10, right), which may be indicative of a reaction with air or water. The change in appearance may be due to oxidation of the molybdenum layer. In this example the entire surface seems affected and not only the part that was exposed to water.

The effect of a low quality coating on the image quality is further exemplified by images from a scintillator with low surface roughness but an affected molybdenum film as identified by visual inspection. We observed reduced biological image quality and an apparent ”wooliness” in FAST-EM acquisitions (Figure 11). It can be noted that the ultrastructure is still well discernible, as opposed to images obtained with large-scale acquisitions from scintillators with high surface roughness, were small ultrastructural features are significantly obscured.

5.4.3 Broad ion-beam polishing

The Ce:YAG substrates supplied by Delmic are by default mechanically polished after the growth process. However, the surface finish by mechanical polishing is typically not sufficient for imaging with FAST-EM. The substrates are broad-ion beam milled to etch the top surface and further reduce the surface roughness to a tolerable low level for imaging. Without polishing by the broad-ion beam, the (molybdenum-coated) scintillator surface

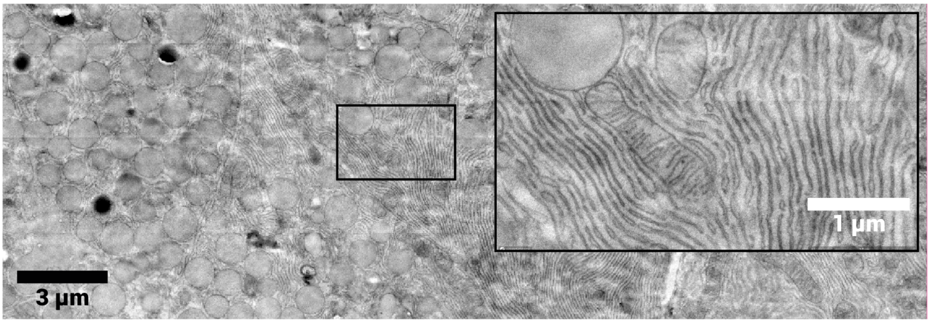

Figure 11: Large-scale acquisition of scintillator with low quality molybdenum film. Inset shows ultrastructure at full resolution. The low quality molybdenum causes intensity variations (”woolliness”) that reduce the overall image quality and apparent contrast. Dwell time: 20 µm. The full dataset can be viewed on WebKnossos.

contains many micrometer- and nanometer-scale defects (Figure 12, left image), mostly appearing as scratches. These defects are visible in FAST-EM images of ultrathin tissue sections (data not shown). The broad ion-beam polishing removes these large defects, but the surface after milling shows dome-shaped structures of typically a few micrometers in size (Figure 12, right image).

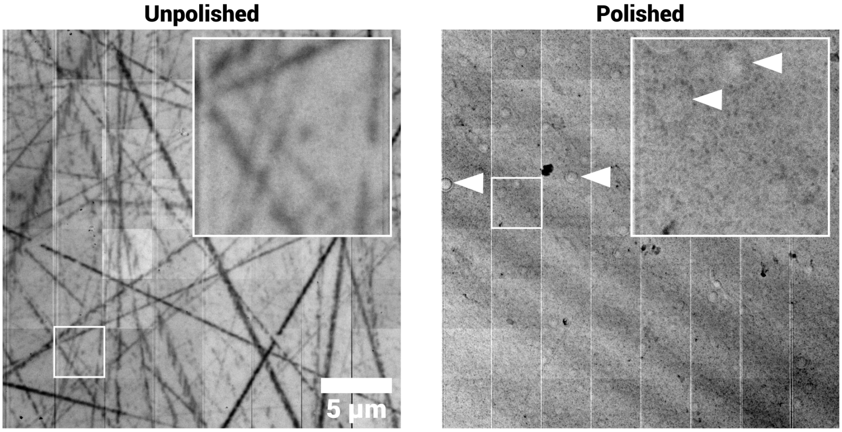

Figure 12: Single field in FAST-EM of both unpolished and ion-beam polished side of scintillator, coated on both sides with 30nm molybdenum. The unpolished side shows significant defects in the form of scratches. Arrows indicate dimple-like artifacts on the ion-beam polished side which are understood to be a result of the ion-beam polishing.

Similar artifacts were also seen in FAST-EM array tomography datasets (Figure 13), both in the section as well as on the substrate surface around the section. In FAST-EM datasets, they have varying prevalence, although usually their occurrence is rare. The artifacts have the highest contrast at the edges, which is likely where there is high curvature. In this specific example, the number of milling artifacts is quite high, and they noticeably obscure the biological contrast. However, most of the biological ultrastructure can still be discerned through artifacts, suggesting that the structures are not composed of material accumulated on the surface by ion sputtering, as this type of artifact would be expected to attenuate the transmission signal.

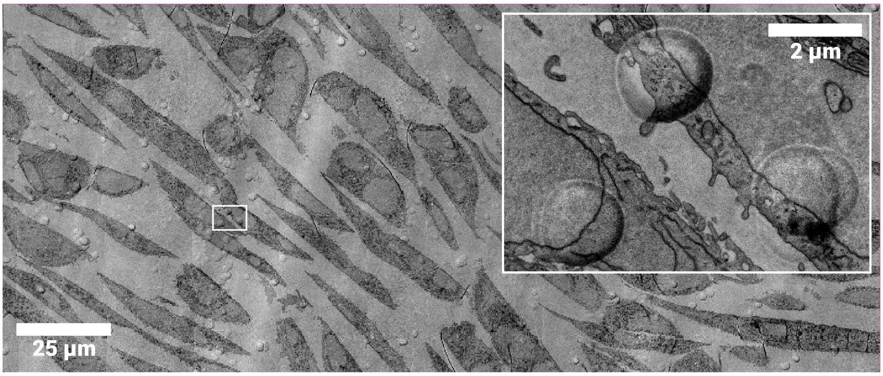

Figure 13: Milling artifacts on the substrate. MCF-7 cell dataset with apparent artifacts that appear as dimples on the surface of the scintillator and are visible through the tissue section.

The structures may be local deformations of the thin molybdenum film. To investigate this, a cross section of the substrate surface was made with a focused ion beam (FIB) in a Helios G3 FIB-SEM (Figure 14). A platinum layer was deposited and subsequently a trench was milled in the substrate. The cross section view shows elevations in the substrate of several hundreds of nanometers. The molybdenum film can be discerned with confidence. It is continuous over the full field-of-view, which contains the full artifact. This observation is consistent with the fact that the transmission signal is not blocked in OSTEM detection (Figure 13). The artifacts appear to have a certain directionality as the transmission signal is most obscured on one specific side.

5.4.4 Striations

A subset of FAST-EM and single-beam OSTEM datasets shows large-scale, quasi-periodic intensity variations, reminiscent of ripples or waves (visible in both Figure 12 and Figure 13). These intensity variations are understood to arise from variations in dopant ion concentration [27]. They are commonly referred to as growth striations and are thought to form mainly by convection and temperature fluctuations in the growth interface [322]. The variations are directional in the scintillator, possibly reflecting the growth direction of the crystal. Since the scan orientation is always the same in FAST-EM, the artifacts have the same directionality in images from serial sections. Interesting, the intensity variations are only apparent on the broad-ion beam polished side of the scintillator, and SPL scintillators did not show these intensity variations. The crystal growth process can thus introduce additional background variation in OSTEM images.

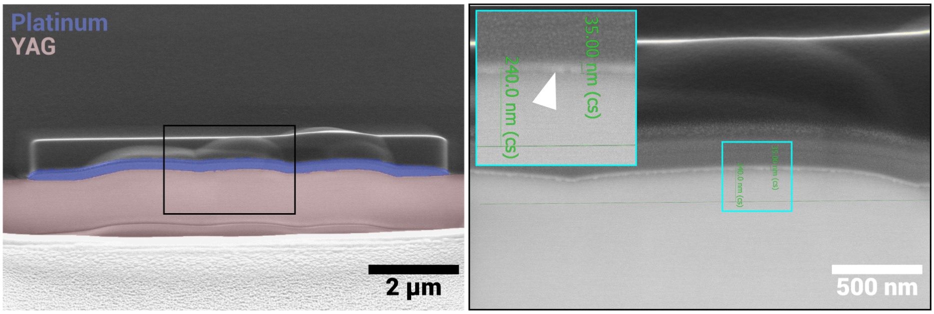

Figure 14: FIB cross section a milling artifact. Indicated in blue and pink are the platinum protection layer and substrate (YAG), respectively. The black inset shows a zoom in on the intersection boundary of the platinum layer and substrate. In immersion mode, the molybdenum layer can be distinguished. The green lines indicate the distance from the material intersection to a line approximately parallel to the substrate surface next to the artifact, showing an elevation of approximately 240 nanometers, and a thickness estimate of the molybdenum layer respectively (white arrow in cyan inset).

5.5 The role of neighbouring beams

5.5.1 Beam damage artifacts by overscanning

In array tomography experiments, some regions of the specimen may be scanned repeatedly by the electron beam, which can lead to artifacts. In BSD and SE these can appear as contrast differences in the image by carbon deposition. In multibeam OSTEM, certain areas of the sample are exposed multiple times at high magnification already in the first scan. Upon reacquisition of the same area, which may be necessary in case of acquisition errors, there is a cumulative effect. The transmission coefficient of the sample may be changed by exposure to the electron beam, thus there could be a different effect on image contrast in OSTEM detection compared to BSD and SE. Additionally, the stability of sections on the substrate could affect their resistance to electron beam irradiation.

The effect of reacquisitions from the same ROA on the image quality and contrast in multibeam OSTEM detection was studied by reacquiring a single ROA from a MCF-7 cell sample (rOTO staining with uranyl acetate, Chapter 4) 19 times in order to investigate how the image quality progressed in repetitive rescans of the sample (Figure 15). This experiment differs from reacquisitions performed for ROAs where the initial acquisition failed (Chapter 4), since in these experiments, the ROAs had to be redefined approximately to the same location for the reacquisitions.

The first scan of the sample shows variations in intensity due to the inhomogeneous electron dose and demonstrates the necessity of post-correction (Chapter 4). Most notably, the overlap scan areas of the adjacent beamlets show a higher image intensity (Figure 15, ”Field” images). The transmission coefficient changes slightly when these areas are scanned twice, thus the image intensity is affected. A thinning of the sample as induced by the electron beam is the most likely explanation. In the second and third scan, the intensity differences diminish, because the differences in section thickness are reduced by the dose accumulated from multiple exposures. From the 5th scan onwards, the effect of electron beam exposure becomes increasingly apparent as horizontal and vertical as

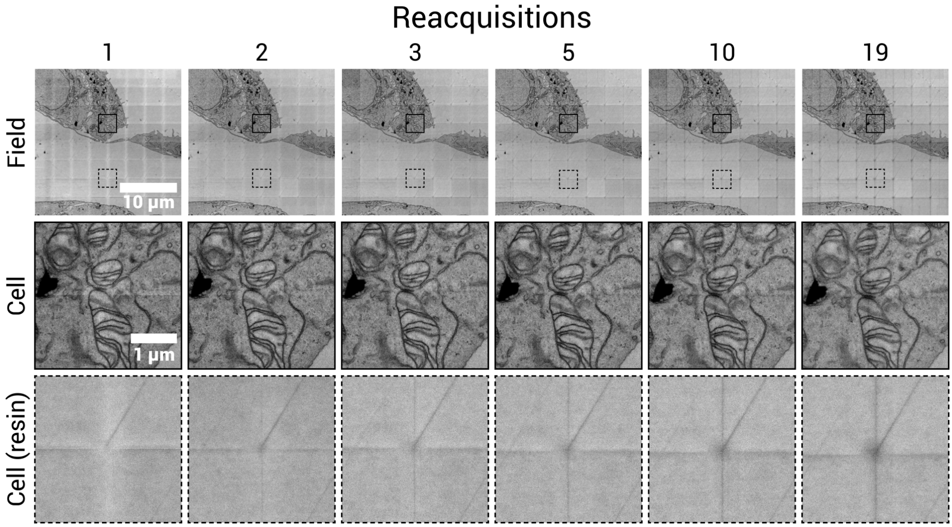

Figure 15: Beam damage artifacts caused by repeated acquisition with FAST-EM. The same field and cell images are shown through progressive scans of a MCF-7 cell sample. The full dataset can be viewed through WebKnossos.

well as diagonal lines form on the sample (Figure 15, ”Cell” images). The effect is most pronounced on the corners of the cell images, which correspond to a sample area that is exposed four times in a single scan (Figure 1C). The edges of the cell have a lower intensity than the surroundings for scans 5 and onwards, which can be explained by increased carbon deposition. The ultrastructure remains visible throughout all 19 repeated scans, which shows that the sample is stable on the substrate and electron beam-induced specimen warping is minimal. The content in the cell images does slightly change position in subsequent rescans, but this is also affected by the repositioning accuracy of the stage. In conclusion, repeated scanning of certain areas reduces intensity differences between cells but introduces (unwanted) beam artifacts.

5.5.2 Crosstalk-induced phantoms

The optical system of the FAST-EM introduces some crosstalk between the signals of adjacent beamlets [27], which may lead to ”phantom” artifacts in neighboring cell images. The interaction volume of the electron beam is converted by the scintillator into a diffraction-limited optical spot. Magnification by the optical system leads to a spot size of several millimeters, which is in the size range of a single MPPC sensor. The optical spot profile on the detector is a convolution of the electron beam interaction volume with the point spread function of the optical system, which will typically have tails since the interaction volume is not homogeneous. The crosstalk is dependent on the setting of the objective correction collar and the local scintillator thickness. Due to the high NA, variations in scintillator thickness may lead to aberrations in the spot, which increase crosstalk. Electron-dense features lead to increased electron scattering and therefore a broadening of the interaction volume and optical spot profile, thereby enhancing the crosstalk. This effect is visible as ”phantoms” in neighboring cell images (Figure 16). It is very apparent for certain image artifacts caused by dirt particles or section folds, but it may also be caused by sharp transitions in contrast from biological features.

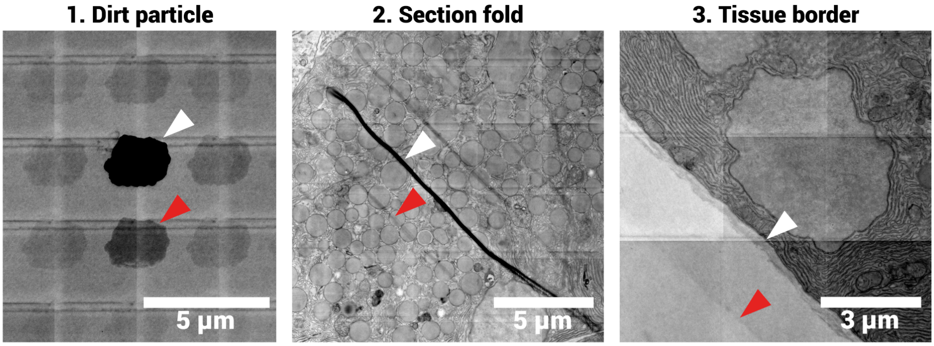

Figure 16: Crosstalk creates ”phantoms” in FAST-EM images. Images show several examples of high contrast features, including (1) a dirt particle, (2) section fold artifact and (3) a transition from tissue to empty resin. The high contrast features locally amplify the detector crosstalk, generating phantom images of the feature in neighboring cells. The white arrows indicate the feature, red arrows indicate the phantom image of the feature in the neighboring cell.

5.5.3 Post-correction artifacts

The effect of artifacts may be aggravated by image processing. Post-corrected FAST-EM images sometimes contained additional image artifacts which could not explained by all aforementioned mechanisms. Some datasets are corrupted by electron-dense artifacts (Figure 17, ”Artifact biased” 1st column image). The image post-correction compensates for intensity differences caused by the multibeam scanning acquisition, by averaging all field images in a single ROA and subtracting this average image from all other field images (Chapter 4, 3rd column in Figure 17). This procedure fails to average out artifact-corrupted images of the average field image. If the number of physical artifacts in the sample is high, the post-correction image (3rd column) introduces pronounced digital artifacts, effectively adding an additional background texture to the post-corrected images (4th and 5th column in Figure 17). The effect is most pronounced in empty resin images that have been corrected (column 2 vs 5). For a dataset without prominent artifacts or electron-dense features (”Artifact free” in Figure 17), the correction image has a mostly uniform background, although intensity differences may still remain on the borders of cell images. The outlier removal procedure as described in Chapter 4 excludes fields with artifacts from the correction image, as long as the number of artifact-free fields in a single ROA remains above a threshold.

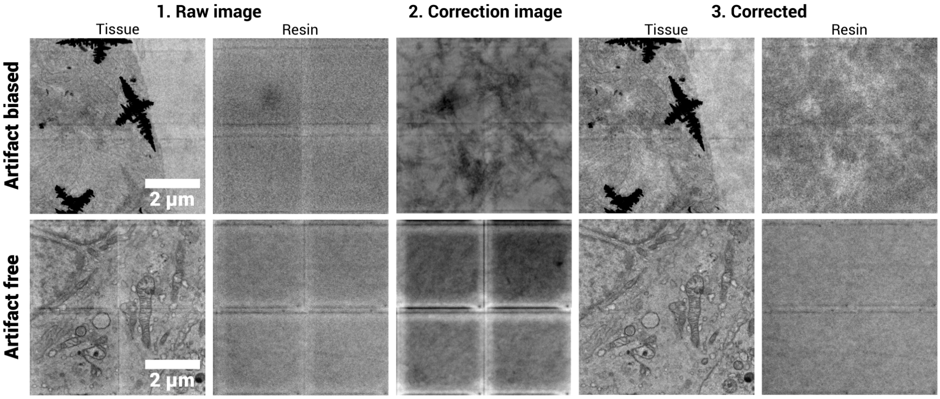

Figure 17: Post-correction of datasets with electron-dense artifacts leads to image artifact. A dataset with many artifacts ("Artifact biased") and without artifacts ("Artifact free") are compared. A 2x2 cell crop of a single field of tissue and empty resin is shown before and after post-correction, as well as the correction image used to create the corrected image. The post-correction, for these image performed without outlier exclusion, fails to average out high-contrast features from the correction image in the upper row, which generates a copying effect where these features are introduced in every field image.

5.6 Discussion

In OSTEM detection, the biological specimen is placed directly on a sample substrate. In this configuration, seamless imaging is possible as opposed to TEM or STEM, where the sample is put on a grid support which leads to obstructed sample areas. However, the biological sample and solid substrate are in direct contact. The substrate condition may therefore affect the biological sample, or vice versa, leading to novel ways in which artifacts may appear in EM images.

Thus far, OSTEM detection seems incompatible with post-staining protocols because of apparent staining solution retention between the substrate and the specimen, leading to artifacts that obscure biological ultrastructure. This specific issue has not been reported in earlier array tomography studies where post-staining was applied to silicon substrates and/or ITO-coated coverslips, despite several studies using landing energies that would enable the electron beam to penetrate the underlying substrate for the used section thickness. Post-staining is typically applied after the sample is imaged with fluorescence microscopy (made possible by immunolabelling or genetically encoded fluorescent probes), because the fluorescence would otherwise be quenched by the heavy metal staining. Silicon wafers are hydrophylized by incubation in sulphuric acid and perhydrol to improve section attachment [308], but such a treatment may affect the molybdenum coating. Glass coverslips are gelatin-coated (subbed) to promote the adhesion of sections [46], which may also prevent post-staining artifacts. However, it is unclear how thick the obtained gelatin layer is and whether a transmission signal would still be obtained when performing OSTEM on subbed substrates.

We conclude that a stable, homogeneous thin-film coating is a prerequisite for obtaining high quality datasets. The coating layer of the scintillator must be resistant to specimen preparation. However, the observed variability in appearance between coatings on different scintillators after specimen preparation suggests that the coating is not inert. The data from these scintillators indicate that an imperfect coating leads to contrast differences in images of biological specimens. The coating can react with sample preparation reagents to form artifacts. The formation of these artifacts as a result of depositing sections onto a scintillator with a loop, as opposed to submersion of the scintillator in the knife boat, suggests that the residence time of the water on the scintillator affects the formation of artifacts. The water droplet may facilitate the reaction between the coating and sample, whereas quick removal by lowering the water level in the bath does not allow for the reaction to occur. An alternative coating or an optimized sample and specimen preparation protocol can prevent the artifacts altogether. Therefore, the interaction of the coating layer with the specimen is not considered a general issue for OSTEM detection.

Oxidation of the molybdenum coating can be a possible cause of the change in appearance after prolonged water or air exposure, since the reflectance of molybdenum oxide (0.14 at 550 nm) is less than metallic molybdenum (0.96). This would explain why the affected scintillator is more transparent. For array tomography, especially the long-term stability of the film when immersed in the water bath is important. Samples could be stored under inert gas to limit oxidation over prolonged time periods. Alternatively, optimization of sputtering protocols may yield coatings that are more resistant to air, water or chemical exposure. Sputtering conditions could be tuned to deliver thin molybdenum films with superior adhesion and reflectance, but the adhesion is linked to grain size which affects the surface roughness [323].

A high substrate quality and good surface polishing is shown to be critical for successful FAST-EM data collection. Irregularities in the substrate surface and doping concentration translate to contrast differences in FAST-EM data, which in turn reduce the biological contrast and may impair the interpretability of biological ultrastructure. Therefore, quality control of substrates prior to specimen preparation should be performed by default. Artifacts from the substrate typically do not show up in conventional array tomography studies that use secondary or backscattered electron detection schemes. This may be because the beam either does not penetrate the underlying substrate at the used landing energies [115, 324, 293] or gets scattered significantly by the underlying substrate [46, 325].

We have shown that low surface roughness correlates strongly with apparent OSTEM image quality of biological samples. However, the roughness measurements of the coated scintillators may have been affected by biological specimen preparation or contamination of the AFM tip, as the 2 µm FOV scans of ”PD11” and ”Delmic” scintillators do not show the detailed surface structure present in the image of SPL scintillator. The ”Delmic” and ”PD11” scans were performed last, thus contamination from ”PD02” or ”SPL” will have affected the results. The biological sample quality contributes minimally to differences seen between scintillators, since BSD images showed no apparent differences in image quality up till 3 keV landing energy. This is roughly the energy at which the interaction volume extends into the scintillator substrate, thus the increased surface roughness fully explains the negative effect on the biological contrast as a function of the landing energy.

Defining an unbiased passing criterium for scintillators based on the presented experimental data is difficult, but scintillators should have low RMS and mean roughness as well as low maximum peak height. Inspection with SEM can yield assessment of relative surface roughness. Quantification of surface roughness by AFM or white light interferometry is a more objective way of assessing whether to pass or reject batches. The highest quality scintillators demonstrate RMS and mean roughness values below 1 nm and 2-3 nm peak height differences before specimen preparation. The coating of PD11 and PD02, based on visual inspection, was clearly affected after biological specimen preparation and imaging. Therefore it is possible that the roughness before specimen preparation was lower, since the coating was still unaffected. A minimum passing criterium could be defined as the average of PD02 and SPL, which would roughly equate to 1 nm RMS/mean roughness and 10nm maximum peak height.

Whether to use a batch of scintillators for experiments can be further motivated by the presence of doping variations, striations and milling artifacts. The extent of these artifacts may be determined prior to specimen preparation by imaging the substrate surface in FAST-EM or single-beam OSTEM. Broad-ion beam milling reduces substrate surface roughness, but it may also introduce artifacts that are attributed to irregularities in the milling speed. Insufficient cleaning of the surface before polishing, resulting in (organic) residues may locally decrease the milling speed of the substrate. Since they are relatively rare, they do not strictly pose a problem for image interpretation. Still, an extra cleaning step prior to broad-ion beam polishing, if not already part of the workflow, may reduce the occurrence of these artifacts.

It has been established that the SPL scintillators have a lower light yield than the main supplier (Delmic), which can be explained by a lower cerium concentration. This may relate to the observation that growth strations patterns are not seen in FAST-EM and single-beam OSTEM acquisitions from SPL scintillators. The absolute differences in cerium concentration can be lower, or the growth process of these scintillators is better controlled. Alternatively, the higher concentration of cerium in the scintillators from Delmic may give rise to more defects introduced in the crystal lattice. This leads to a higher surface roughness which necessitates the ion-beam polishing and more variation in cerium concentrations due to interruptions of the growth process. The high surface roughness may obscure strations in scintillators that have not been broad-ion beam polished.

Detector crosstalk creates new kinds of artifacts in multibeam OSTEM images, which appear as phantoms in neighboring cell images. In general, crosstalk adds uncorrelated intensity contributions to a pixel, therefore it lowers the effective image SNR and contrast. Thus, the amount of crosstalk in the system should be minimized. This can be achieved by optimizing the setting of the correction collar at the beginning of an experiment. The correct setting can be found by focusing a single beam on the substrate surface and acquiring a z stack of the point spread function, while moving the objective lens through the optical focus position. The correction collar should then be set to the value that minimizes the size of the point spread function tails.

The repeated imaging of sections with FAST-EM leads to electron beam-induced artifacts in rOTO stained, EPON-embedded samples. The effect and extent of electron-beam exposure and damage may be sample and embedding material specific. A thorough investigation on different samples and embedding materials was not performed, but may be interesting for future research, especially when extending FAST-EM to different applications. In serial-section TEM or large-scale STEM, 'prebaking' or pre-exposure steps are typically performed at low magnification [8, 326], to reduce warping and shrinkage of the

Table 1: Identified artifacts, their cause and mitigation.

Category	Type of artifact	(Possible) cause	Mitigation
Sample preparation	Post-staining artifacts (section 5.3.1)	Heavy metal staining retention between the section and substrate	Use en bloc staining, perform washing steps of post-stained sections
	Electron-dense precipitates (section 5.3.2)	Reaction between molybdenum coating and sample preparation chemicals	Use alternative coating (chromium), prepare sections with array tomography knife boat
Substrate quality	Reduced contrast, grainy images (section 5.4.1)	Substrate roughness	Better surface polishing, perform quality control of substrates with AFM or white light interferometry
	Image "wooliness" (section 5.4.2)	Low film coating quality	Quality control of substrates by visual inspection
	Milling artifacts (section 5.4.3)	Broad-ion beam polishing	Alternative polishing technique, quality control with SEM
	Directional intensity variations (section 5.4.4)	Growth striations and fluctuations in cerium concentrations	Digital image correction
Imaging, detection	Diagonal stripe patterns (section 5.5.1)	Beam damage	Pre-exposure with defocused beam
	Phantoms (section 5.5.2)	Crosstalk between adjacent beam signals	Minimize crosstalk by optical objective correction collar, reduce landing energy
Image processing	Post-correction artifacts (section 5.5.3)	Average correction image is biased towards electron-dense features	Correction with exclusion of outlying fields from average image

specimen under high-dose acquisition. Such a procedure may be useful to prevent e-beam induced artifacts in FAST-EM acquisitions. In TEM, a parallel beam is used to pre-irradiate the sample. Thus, pre-exposure in FAST-EM should be performed with a defocused beam. Such a procedure, applied before imaging, may also have the benefit of removing intensity differences induced by the multibeam scanning procedure, thus avoiding the need for post-processing. The outlier removal procedure as described in

In conclusion, we identified several previously unnoticed artifacts when combining conventional EM sample preparation with scintillator substrates and OSTEM detection, which we summarize in (Table 1). It is shown that common artifacts in single and multibeam OSTEM can be attributed to interactions between the sample and scintillator substrate, the quality of the substrate or the crosstalk between neighboring beams in a multibeam OSTEM detection system. Awareness of artifacts in general helps discriminating biological features from artificial features. A thorough listing of these features will help future users of FAST-EM in the interpretation of the data and in optimizing and evaluating sample preparation protocols, acquisition, and data processing pipelines. In addition, understanding the root causes for how there artifacts arise, helps finding mitigation strategies and thus preventing their occurrence.

Acknowledgments

Cecilia de Heus from UMC Utrecht and Anouk Wolters, Peter Duinkerken and Harita Yedavally from UMC Groningen prepared the biological samples. The content of this chapter has benefited significantly from input and discussion by Peter Duinkerken, Ryan Lane, Ben Giepmans and Jacob Hoogenboom. Additionally, we thank Mike Simons and Cristiano Glessi from the department of Imaging Physics for assisting with the cross-section and EDX experiments, Allard Katan from the department of Quantum Nanoscience for performing the AFM measurements and Marre Niessen, Wilco Zuidema and Thera Pals from Delmic for technical support.

Data availability

The raw microscopy data underlying the figures is available through the 4TU repository (DOI: `https://doi.org/10.4121/01efed58-9427-478a-8687-50b35daf3d9c`). Access to large-scale datasets is provided via the links in the figures.

6

Conclusion and outlook

6.1 Main conclusions per chapter

This thesis is centered around implementing volume electron microscopy (vEM) with a novel multibeam scanning transmission electron microscope (FAST-EM). FAST-EM utilizes optical transmission detection to separate the signals from the individual beams. Multibeam scanning electron microscopy (mSEM) increases the acquisition speed in vEM workflows, thereby effectively reducing the time required to acquire volume datasets. This enables novel types of experiments involving larger sample volumes or multiple samples with different biological conditions.

In Chapter 2 we conclude that instrumentation development is a key driving factor for innovation and progress in vEM research. It has enabled large-scale (3D) imaging, ensured better accessibility of EM techniques and recently made possible the imaging of millimeter-sized samples. Faster electron microscopes are shifting the bottleneck from acquisition to data analysis and management. The developments in automatic segmentation of vEM data have progressed at a fast pace; yet, the use of automated segmentation is not widespread except for connectomics studies, which means that the research field still relies on extensive manual annotation efforts to analyze vEM datasets. The expertise and resources for high-throughput vEM remain accessible only to a limited number of research groups; the role of core facilities to invest in commercial fast electron microscopes and an elaborate data infrastructure could be crucial in accelerating vEM research.

The adoption of FAST-EM as a vEM instrumentation tool requires extensive characterization and benchmarking. In Chapter 3 it is demonstrated that deposition of ultrathin sections directly on scintillator substrates combined with optical transmission electron detection (OSTEM) is a viable technique for large-scale EM. It provides large unobstructed views as opposed to grid supports in (S)TEM. OSTEM detection performs similar to backscattered and secondary electron detection in terms of apparent image contrast, signal-to-noise ratio and resolution. Backscattered electron detection with a negative stage bias and annular dark-field scanning transmission EM may outperform OSTEM for moderate to long dwell times, whereas for dwell times shorter than 1 µs, OSTEM detection outperforms biased backscattered electron detection. This is favorable in large-scale imaging since dwell times should be as short as possible to minimize acquisition times. Furthermore, we found indirect evidence for partial saturation of the scintillator, which may arise because the interaction of the focused electron beam is confined to a very small volume in the scintillator substrate. Further optimization of the substrate may therefore lead to faster acquisition speeds in single-beam SEMs and mSEMs.

Chapter 4 presents the implementation of a full workflow, from sample preparation to data analysis, for using FAST-EM in volume electron microscopy. FAST-EM array tomography produces high resolution vEM datasets of consistent quality, suitable for biological interpretation. It is further shown that FAST-EM is compatible with conventional EM sample preparation protocols and that image analysis tools developed for different vEM modalities can be applied to FAST-EM datasets directly. While being significantly faster than a single-beam SEM, the throughput of the early adopter FAST-EM system is currently at least an order lower than other state-of-the-art techniques. However, it can be further increased by minimizing overhead and optimizing imaging parameters and detection conditions. An optimized electron optical column design is required to close the remaining throughput gap with other techniques.

The combination of conventional biological EM sample preparation, scintillator solid substrates and single-beam or multibeam OSTEM leads to several unexpected image artifacts that do not show up in conventional array tomography techniques (Chapter 5). We have identified possible interactions between the sample and substrate boundary, which lead to artifacts that obscure biological ultrastructure. Moreover, we found that OSTEM is particularly sensitive to variations in the substrate profile, which are visible as artifacts in the biological images. Multibeam OSTEM has the added effect of generating contrast differences in the image by repeated exposure of certain sample regions and lowering the effective signal-to-noise ratio and contrast by detector crosstalk. Together, these image artifacts may hamper the acquisition of high-quality vEM datasets with FAST-EM, but the impact of most artifacts is minimized or mitigated through modification of sample preparation protocols, quality control of substrates, pre-irradiation of samples and optimization of detection settings.

6.2 FAST-EM AT and OSTEM in correlative and very large scale applications

Bridging different imaging modalities with EM offers several advantages: fluorescence microscopy provides (live) molecular labeling and specificity [12], and both fluorescence microscopy and x-ray microscopy may facilitate region-of-interest targeting for vEM in larger samples [327, 328]. As such, vEM is typically performed in combination with correlative microscopy techniques. FAST-EM can be integrated in different correlative microscopy workflows. In correlative light and electron microscopy (CLEM), the light microscopy can be performed either pre-embedding on live or fixed samples (as in sequential CLEM) or post-embedding (i.e. in-resin or integrated CLEM). In sequential CLEM, the light and electron microscopy are separated, thus FAST-EM can be readily integrated in such a workflow. The combination of FAST-EM with post-embedding CLEM will require the development of scintillator substrates that are transparent to commonly used laser excitation wavelengths. Moreover, post-staining will be required for optimal contrast in embedding protocols that are optimized to retain fluorescence of genetically encoded reporters or fluorescent dyes. Thus, the development of post-staining protocols for FAST-EM is necessary that do not produce the typical artifacts as shown in section 5.3.

As demonstrated, FAST-EM delivers datasets of several hundreds of micrometers in the largest dimension. FAST-EM array tomography can be used to create and image specimens consisting of hundreds of serial sections (up to 220 has been demonstrated, data not shown). Nonetheless, limitations are set by the amount of sections that can be collected on a single scintillator substrate, as well as the maximum amount of serial sections that can be collected in array tomography using ribbons. Scintillator substrates (14 x 14 mm) are smaller than coverslips (22 x 22 mm) and silicon wafers, which are typically used in array tomography. For coverslips, this results in a 2.5 times smaller usable area for section collection. This restricts millimeter scale vEM, as the number of sections that fit on a single substrate would be limited to 100-150. Transferring long ribbons to coverslips without breaking or losing sections is challenging, but collection of a thousand serial sections on a single coverslip has been demonstrated [329, 330], thus setting the practical limit for scintillators around 500 sections. Collecting sections on multiple substrates is theoretically possible, but there is a significantly increased risk of material loss as it requires an interruption of the section process. Increasing the amount of serial sections above the practical limit of array tomography with ribbons is possible with magnetic collection and the use of larger scintillator substrates (Chapter 4), but both have yet to be tested for compatibility with FAST-EM. The limited flexibility of FAST-EM with respect to the imaging parameters also poses restrictions for array tomography. Without landing energy optimization and the ability to go to higher probe currents in the early adopter models, contrast of thin (40-60 nm) sections will be suboptimal (Chapter 3). However, lateral and axial resolution will both increase with thinner sections as the interaction volume of the low voltage electron beam decreases. Thinner sections also limit the specimen dimension in the sectioning direction, since the upper section limit remains constant.

6.3 Future outlook

6.3.1 Novel applications of FAST-EM array tomography

We have identified several applications where FAST-EM array tomography could be applied to answer novel biological research questions, without the direct need to combine FAST-EM with correlative techniques. One of them is visualizing organelle structural changes in large populations of cells. Correlative organelle microscopy [331, 295] enables functional-structural studies by tracking dynamical processes in live cells and correlating this information with 3D ultrastructural context. While this technique allows for the study of hundreds of organelle interactions at a time, it fails to capture the full ultrastructural variation of these interactions. The used vEM technique, FIB-SEM, has limited throughput and is therefore capable of only imaging few cells of interest, which may not be a representative sample. The higher throughput of FAST-EM allows the sampling of tens to hundreds of cells and thus a multitude of organelles (albeit with lower z resolution). This will highlight subtle structural changes in organelles induced by molecular perturbations to the cells, which may be implicated in disease. The sampling of many cells also lends itself to studying other (rare) cellular processes, such as the different stages of cell division.

vEM studies typically prepare multiple specimens, but usually only one is targeted for acquisition because of restrictions on acquisition time and resources. It is feasible to study brain development of several individuals from the same species (e.g. *C. elegans* [67]), as well as for targeted regions in mice using partial connectomic reconstructions [205]. Still, these studies only sample limited discrete time points and rely on only a few selected replicates. This implies that the biological 3D ultrastructural variation between specimens, but also between different species, remains largely unexplored. Since FAST-EM significantly accelerates array tomography studies, it should become possible to image several specimens of interest and to test multiple biological conditions where the molecular biology is perturbed by genetic modifications or treatment with compounds.

6.3.2 Interpretation and image analysis of FAST-EM datasets

FAST-EM can only be used to its full potential if several bottlenecks are solved. This includes, among other things, the combination of FAST-EM with complementary imaging modalities. In addition to the correlative techniques discussed earlier, a different and potentially low-cost approach for adding biological specificity to FAST-EM datasets relies on label-free predictions of fluorescence [332]. Artificial fluorescence is generated by training a convolutional neural network (CNN) to predict fluorescence directly from the EM images. First, a small specimen is prepared for integrated correlative array tomography (CAT), with sample preparation optimized to preserve fluorescence [293]. CAT produces a collection of registered fluorescence and electron microscopy image pairs with high (1 µm) registration accuracy, which serve as training inputs for the CNN. A similar specimen can then be prepared for FAST-EM array tomography, but with optimal staining for high EM contrast, and the artificial fluorescence is predicted from FAST-EM data using the CNN. However, since the network is trained using data from a different EM modality, an extra transformation step is required to make the FAST-EM data resemble this modality. It has been shown that single-beam OSTEM data (Chapter 3) can be transformed to resemble BSD data as acquired in CAT using cycle-consistent generative adversarial networks (GANs) [333]. CycleGANs ensure that the transformed data (BSD-like images) retains the characteristics from the original (OSTEM data) by computing the cycle-consistency loss by comparing the output of a retransformed image to the original input image [334]. The cycleGAN networks are trained using unpaired BSD and OSTEM images. A similar approach could be used to infer elemental specificity in FAST-EM datasets using energy-dispersive X-ray spectroscopy, which has been demonstrated to be useful for label-free, unsupervised annotation and segmentation of distinct biological structures of interest [335].

6.3.3 Further throughput improvements of FAST-EM

In this thesis, research is performed with an early adopted version of FAST-EM, where the emphasis has been on image quality. As a result, FAST-EM has not yet been optimized for high throughput. We discussed how the throughput of FAST-EM can be improved in section 4.3. To provide concrete suggestions for future directions, the throughput gain is calculated for a volume acquisition as proposed in section 4.2.6, for five separate improvements (Table 1). The first improvement is reduction of the dwell time. The second is optimization of the overhead. The latter three improvements require modifications to the FAST-EM electron-optical column, of which the first is to increase the field size. An alternative option is to implement multifield scanning (suggested by Zuidema), increasing the effective field size [27]. The last and most extensive option is to design a new, small electron-optical column with fast electrostatic beam deflection dedicated to operating at low energies.

Reduction of the dwell time should be the first priority, since the total acquisition time is currently dominated by the scanning time (Chapter 4, Figure A6). The lower limit (400 ns) is set by the mirror galvanometers, which should be feasible by several improvements, and can lead to a throughput of 20.5 MPx/s. The improvements are (a) increasing the probe current to 1 nA (possible in the current MBS design), (b) optimization of the landing energy to the section thickness and (c) optimization of the OSTEM detector layout.

(c) is a topic of current research. Partial saturation in OSTEM implies that there is loss of potential signal, which reduces SNR and contrast. Saturation increases mostly as a function of the beam current [27, 282]. To understand the mechanism of saturation and provide means to improve it, a model is required that describes the electron scattering, energy transfer to the material and conversion to scintillation light. Since scintillation in ce:YAG relies on energy transfer to the cerium dopant, Monte-Carlo simulations of low energy electron interactions should be performed [336]. The spatial distribution of energy deposition can be used to determine what fraction of the interaction volume saturates, which can then be converted to a photon output. The simulation results can be coupled to experimental data of photon intensity from the OSTEM detector at different landing energies and probe currents. The model can be step-wise extended to include the contributions of different coating materials, thicknesses and a biological sample in order to determine the optimum imaging parameters and optimal coating that maximize the signal-to-noise ratio and contrast for a given substrate-sample combination.

Optimization of the overhead is the next step after dwell time reduction, since it will become the second limiting factor. Currently, stage translations require 0.52 s overhead time. However, the nominal settling time of the stage for a 1D movement is much lower (150 ms). It should therefore be feasible to reduce stage overhead. If this is not possible in practice, the implementation of a piezo stage could be considered, which has a faster settling time. The remaining overhead is caused by the precalibration (optical focusing) and beam shift correction after each stage translation (personal communication with Delmic). Optimization of both overhead times should be possible, especially since these calibrations may not be necessary after every section and field acquisition. Ultimately this should lead to a throughput of 39.0 MPx/s.

After reducing the dwell time and optimizing the overhead times, the throughput will still be limited by stage overhead. Thus, next strategies should aim to reduce the number of stage translations. First, we investigate an increase of the field size. This could be achieved by increasing the scan resolution and simultaneously reducing the magnification of the electron beam and optical system, under the assumption that the beam pitch can be scaled accordingly without influencing the resolution. A twofold increase in scan resolution with a field overlap of 3% leads to an effective field size of 49.6 μm, which reduces the amount of stage translations needed by 73% and further increases the throughput to 59.5 MPx/s.

The second option is multi-field scanning, which is achieved by an electron beam shift. It is possible to scan 3 x 3 fields without a stage translation. The field-of-view of the optical objective lens is large enough to accomodate the multifield width, thus descanning can be performed by the galvonometric mirrors and no modifications are required in the optical detection system. The effective field size increases to 74.4 µm (assuming 100 pixels overlap between fields, and 2% stage overlap). This cuts the amount of stage translations by 91% with respect to a normal field-of-view and increases the throughput to 73.9 MPx/s.

The final option is a small electron column with electrostatic deflectors optimized for mSEM. This has recently been proposed at TU Delft, since the Apreo SEM column in FAST-EM is not designed for mSEM. The use of electrostatic deflectors would eliminate the overhead currently reserved for pre-compensation of the scan coil self-induction [27]. The possibility to add more beams (up to 196 has been demonstrated [96]) leads to a further throughput increase. Adding more beams in the current FAST-EM implementation would increase Coulomb interactions between electrons, which necessitates a reduction in probe current to retain a similar probe size. Thus the throughput would not increase. Coulomb repulsions result in trajectory displacement of electrons (increasing the virtual source size) and give rise to the Boersch effect (increased energy spread of the beam). The Boersch effect for a multibeam system with typical parameters as considered here is much smaller than the energy spread of the source, and thus can be neglected [337]. For typical beam currents in mSEM, it is further assumed that interactions are weak and incomplete, and occur between single particles. Two regimes are considered: the Holtzmark regime, in which the beam diameter is larger than the average distance between electrons; and the pencil beam regime, in which the beam size is considered to be much smaller than the average distance between electrons. Subsequently, for a beam segment of length L with a narrow crossover at position S_c, the trajectory displacement (FW50) in the Holtzmark and pencil beam regime is given by the expressions derived by Jansen [338]:

$$FW50_H = 0.172\frac{m^{1/3}}{\epsilon_0}[S_c^{2/3} + (1 - S_c)^{2/3}]\frac{I^{2/3}L^{2/3}}{V^{4/3}\alpha^{4/3}} \tag{6.1}$$

$$FW50_P = 0.145\frac{m^{3/2}}{e^{7/2}\epsilon_0}[S_c^3 + (1 - S_c)^3]\frac{I^3\alpha L^3}{V^{5/2}} \tag{6.2}$$

with m the electron mass, I the beam current, V the potential and α the aperture angle.

The expressions for a multibeam system are derived by Stopka & Kruit [337] and depend on the number of beams as well as the pitch. The slice method [339] is used to precisely calculate the total trajectory displacement contribution from all regimes in thin cylindrical slices and then integrate these over the full segment length. Nonetheless, it follows directly from equations 6.1 and 6.2 that a smaller L (which can be achieved by reducing the column length) leads to a smaller trajectory displacement. This implies that the beam current (or the number of beams) could be increased while limiting the effect of Coulomb interactions. With an optimized column, we assume that the number of beams can be increased to 196 with a pitch scaled down to 1.8 µm to limit off-axis aberrations. In such a design, each beam scans 557 pixels in each direction (including overlap). This leads to an effective throughput of 70.0 MPx/s, approximately the same as in the multi-field scanning approach.

In conclusion, an estimated maximum throughput of 73.9 MPx/s is possible. Thus, even in the most optimistic case, FAST-EM remains slower than ATUM-MultiSEM and beam deflection TEM (91.48, 133.55 MPx/s respectively, section 4.2.6). To close the remaining

Table 1: Estimated throughput and acquisition times of a 500 x 500 x 50 μm^3 volume from 500 serial sections for different improvements of FAST-EM.

Improvement	**Key changes**	**Throughput (MPx/s)**	**Difference**	**Acquisition time for 500x500x50 μm^3 (h)**
-	-	10.8	-	201,0
1. Dwell time reduction	Beam current increase to 1 nA, landing energy optimization, substrate saturation reduction	20.5	190%	105,8
2. Overhead optimization	Reduced stage overhead, optimized duration and amount of calibrations	39.0	361%	55,6
3.1. Field size increase	Increased scan resolution, reduced amount of necessary stage translations	59.5	551%	36,5
3.2. Multi-field scanning	Increased scan resolution, further reduced amount of necessary stage translations	73.9	684%	29,4
3.3. Small electrostatic column with 196 beams	No overhead from scan coils, increased number of beams (total pitch remains constant)	70.0	648%	31,0

gap with the other techniques, the field size must be further increased. It may be possible to extend the field-size in an electrostatic column with 196 beams, if the pitch between the beams can be increased. In order to achieve this, the off-axial aberrations on the outer beams have to be compensated.

6.3.4 Towards near-isotropic resolution in FAST-EM AT

FAST-EM array tomography, as opposed to ATUM-MultiSEM, is currently a sub-optimal technique for certain applications where higher axial resolution (30-40 nm) is required, such as the inference of synaptic relations between neurons. There is no physical restriction to cutting ribbons of 40 nm thick sections, but the contrast will be low since landing energy optimization is still limited in the early adopter FAST-EM.

To increase the z resolution of FAST-EM datasets beyond that of the sectioning limit, it has recently been proposed to combine FAST-EM with iterative broad-ion beam milling, an approach referred to as BIB-mSTEM [340]. In the field of connectomics, automated segmentation is frequently used to segment neurons. The majority of mistakes made by segmentation algorithms result from ultrathin sectioning artifacts. To reduce the occurrence of such artifacts and increase the axial resolution, it is proposed to cut semithin (200-1000 nm) serial sections, which is more reliable. The semithin sections are then iteratively milled with a broad ion beam, while performing successive rounds of FAST-EM imaging in between milling steps (Figure 1). This process is repeated until the sections are fully destructed. This procedure generates a set of projection images of increasingly thinner sections, which are then deconvolved to reconstruct a vEM dataset compromised of images of the tissue that is removed during each milling step. With precise increments of the broad ion beam and homogeneous milling, a large-scale EM dataset with near-isotropic voxel resolution (4 x 4 x 10-15 nm) could then be created.

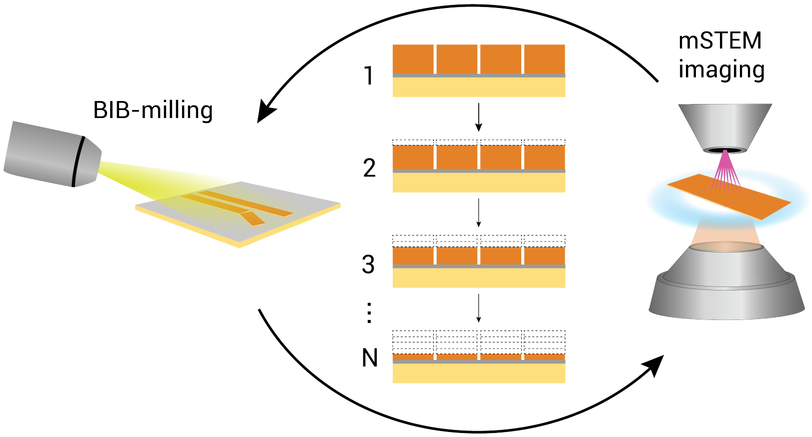

Figure 1: Approach for broad-ion beam milling combined with multibeam scanning transmission electron microscopy (BIB-mSTEM) to acquire large volumes with near-isotropic voxel resolution. BIB milling is applied to semithin (200-1000 nm) serial sections to iteratively remove a thin layer of material from each section, after which the sections are imaged with FAST-EM. The volume is reconstructed from the images of the iteratively milled sections. Near-isotropic resolution can be achieved by applying a deconvolution between imaging steps to retrieve the information that corresponds to the layer that is removed between milling steps (dashed lines).

6.4 Final remarks

This thesis describes the implementation of multibeam array tomography using a 64-beam scanning transmission electron microscope (FAST-EM). FAST-EM array tomography is benchmarked and demonstrated for vEM of ultrathin biological tissue sections. In the preceding sections, we discussed a broader implementation of FAST-EM in biological applications, extension to workflows including correlative techniques, and further improvements to increase the overall acquisition throughput and axial resolution of data sets. We reasoned that a throughput of 70 MPx/s should be feasible. This is less than ATUM-MultiSEM and beam deflection TEM, but of comparable and competitive magnitude. Recently started research and development projects have taken the first steps in the direction of implementing these improvements.

The throughput increase offered by fast electron microscopy techniques, such as FAST-EM, opens up new avenues for exploring biological ultrastructure. It can make vEM a more quantitative technique, for example through comparative and systems-level studies which offer statistically significant measurements on the nanoscale structure and organization of tissues and cells. However, such a prospect comes with significant challenges in sample preparation, but even more in data analysis and management. The time required to produce a full analysis of large-scale datasets currently exceeds their acquisition time, as evidenced by recent results from the combined effort of researchers in large international collaborations [281, 9, 341]. High-throughput, large-scale EM therefore drastically changes the view on how to deal with electron microscopy and ultrastructural data. Reliable and easy-to-use solutions for fully automated segmentation and extensive validation of these methods are required. Meticulous documentation of data and metadata should become the standard. Only then can the full potential from vEM datasets be realized.

References

[1] M. Nagai et al. “Glomerular cellular interactions following disruption of the glomerular basement membrane in IgA nephropathy: ultrastructural analyses by 3-dimensional serial block-face scanning electron microscopy”. *Kidney Medicine* 2.2 (2020), pp. 222–225.

[2] C. J. Peddie et al. “Volume electron microscopy”. *Nature Reviews Methods Primers* 2.1 (2022), p. 51.

[3] L. Heinrich et al. “Whole-cell organelle segmentation in volume electron microscopy”. *Nature* (2021), pp. 1–6.

[4] A. Müller et al. “3D FIB-SEM reconstruction of microtubule–organelle interaction in whole primary mouse β cells”. *Journal of Cell Biology* 220.2 (2020).

[5] J. G. White et al. “The structure of the nervous system of the nematode Caenorhabditis elegans”. *Philos Trans R Soc Lond B Biol Sci* 314.1165 (1986), pp. 1–340.

[6] K. Ryan, Z. Lu, and I. A. Meinertzhagen. “The CNS connectome of a tadpole larva of Ciona intestinalis (L.) highlights sidedness in the brain of a chordate sibling”. *Elife* 5 (2016), e16962.

[7] D. G. C. Hildebrand et al. “Whole-brain serial-section electron microscopy in larval zebrafish”. *Nature* 545.7654 (2017), pp. 345–349.

[8] Z. Zheng et al. “A complete electron microscopy volume of the brain of adult Drosophila melanogaster”. *Cell* 174.3 (2018), pp. 730–743.

[9] S. Dorkenwald et al. “Neuronal wiring diagram of an adult brain”. *Nature* 634.8032 (2024), pp. 124–138.

[10] F. Balzarotti et al. “Nanometer resolution imaging and tracking of fluorescent molecules with minimal photon fluxes”. *Science* 355.6325 (2017), pp. 606–612.

[11] S. C. Reinhardt et al. “Ångström-resolution fluorescence microscopy”. *Nature* 617.7962 (2023), pp. 711–716.

[12] P. De Boer, J. P. Hoogenboom, and B. N. Giepmans. “Correlated light and electron microscopy: ultrastructure lights up!” *Nature methods* 12.6 (2015), pp. 503–513.

[13] R. Egerton and M. Watanabe. “Spatial resolution in transmission electron microscopy”. *Micron* 160 (2022), p. 103304.

[14] P. Hawkes. “Aberration correction past and present”. *Philosophical Transactions of the Royal Society A: Mathematical, Physical and Engineering Sciences* 367.1903 (2009), pp. 3637–3664.

[15] M. Bronsgeest et al. “Probe current, probe size, and the practical brightness for probe forming systems”. *Journal of Vacuum Science & Technology B: Microelectronics and Nanometer Structures Processing, Measurement, and Phenomena* 26.3 (2008), pp. 949–955.

[16] J. Barth and P. Kruit. “Addition of different contributions to the charged particle probe size”. *Optik (Stuttgart)* 101.3 (1996), pp. 101–109.

[17] Z. Zheng et al. “Fast imaging of millimeter-scale areas with beam deflection transmission electron microscopy”. *Nature Communications* 15.1 (2024), p. 6860.

[18] T. Chang et al. “Multiple electron-beam lithography”. *Microelectronic Engineering* 57 (2001), pp. 117–135.

[19] W. Van Dorp et al. “Growth behavior near the ultimate resolution of nanometer-scale focused electron beam-induced deposition”. *Nanotechnology* 19.22 (2008), p. 225305.

[20] M. Malloy et al. “Massively parallel E-beam inspection: enabling next-generation patterned defect inspection for wafer and mask manufacturing”. *Alternative Lithographic Technologies VII.* Vol. 9423. SPIE. 2015, pp. 265–274.

[21] W. Ren et al. “Multi-beam technology for defect inspection of wafer and mask”. *35th European Mask and Lithography Conference (EMLC 2019)*. Vol. 11177. SPIE. 2019, pp. 52–56.

[22] M. J. van Bruggen. “Multi-electron beam system for high resolution electron beam induced deposition”. PhD thesis. 2008. URL: `https://api.semanticscholar.org/CorpusID:135527095`.

[23] Y. Zhang. “A 100-electron-beam source from a high brightness Schottky emitter for fast patterning applications”. PhD thesis. 2008. URL: `https://api.semanticscholar.org/CorpusID:136747827`.

[24] A. Mohammadi-Gheidari. “196 Beams in a Scanning Electron Microscope”. *Delft University of Technology, Delft* (2013).

[25] Y. Ren. “Imaging systems in the Delft Multi-Beam Scanning Electron Microscope 1”. PhD thesis. 2017.

[26] Y. Ren and P. Kruit. “Transmission electron imaging in the Delft multibeam scanning electron microscope 1”. *Journal of Vacuum Science & Technology B, Nanotechnology and Microelectronics: Materials, Processing, Measurement, and Phenomena* 34.6 (2016), 06KF02.

[27] W. Zuidema. “High Speed Electron Microscopy: Engineering of a commercial multi-beam scanning electron microscope with transmission imaging” (2023).

[28] W. Zuidema and P. Kruit. “Transmission imaging on a scintillator in a scanning electron microscope”. *Ultramicroscopy* 218 (2020), p. 113055.

[29] P. Kruit and W. Zuidema. “A Dedicated Multi-Beam SEM for Transmission Imaging of Thin Samples”. *Microscopy and Microanalysis* 25.S2 (2019), pp. 1034–1035.

[30] K. L. Briggman and D. D. Bock. “Volume electron microscopy for neuronal circuit reconstruction”. *Current opinion in neurobiology* 22.1 (2012), pp. 154–161.

[31] C. Xiao et al. “Automatic mitochondria segmentation for EM data using a 3D supervised convolutional network”. *Frontiers in neuroanatomy* 12 (2018), p. 92.

[32] J. Liu et al. “Automatic reconstruction of mitochondria and endoplasmic reticulum in electron microscopy volumes by deep learning”. *Frontiers in neuroscience* 14 (2020).

[33] E. Gómez-de-Mariscal et al. “Deep-learning-based segmentation of small extracellular vesicles in transmission electron microscopy images”. *Scientific reports* 9.1 (2019), pp. 1–10.

[34] J. R. Harris. “Transmission electron microscopy in molecular structural biology: a historical survey”. *Archives of biochemistry and biophysics* 581 (2015), pp. 3–18.

[35] A. Birch-Andersen. “Reconstruction of the Nuclear Sites of Salmonella typhimurium from Electron Micrographs of Serial Sections”. *Microbiology* 13.2 (1955), pp. 327–329.

[36] B. Bang and F. Bang. “Graphic reconstruction of the third dimension from serial electron microphotographs”. *Journal of ultrastructure research* 1.2 (1957), pp. 138–146.

[37] J. K. Stevens et al. “A systematic approach to reconstructing microcircuitry by electron microscopy of serial sections”. *Brain Research Reviews* 2.1-3 (1980), pp. 265–293.

[38] K. M. Harris et al. “Uniform serial sectioning for transmission electron microscopy”. *Journal of Neuroscience* 26.47 (2006), pp. 12101–12103.

[39] C. J. Peddie and L. M. Collinson. “Exploring the third dimension: volume electron microscopy comes of age”. *Micron* 61 (2014), pp. 9–19.

[40] G. E. Soto et al. “Serial section electron tomography: a method for three-dimensional reconstruction of large structures”. *Neuroimage* 1.3 (1994), pp. 230–243.

[41] M. Bárcena and A. J. Koster. “Electron tomography in life science”. *Seminars in cell & developmental biology*. Vol. 20. 8. Elsevier. 2009, pp. 920–930.

[42] M. F. Hohmann-Marriott et al. “Nanoscale 3D cellular imaging by axial scanning transmission electron tomography”. *Nature methods* 6.10 (2009), pp. 729–731.

[43] W. Denk and H. Horstmann. “Serial block-face scanning electron microscopy to reconstruct three-dimensional tissue nanostructure”. *PLoS Biol* 2.11 (2004), e329.

[44] J. A. Heymann et al. “Site-specific 3D imaging of cells and tissues with a dual beam microscope”. *Journal of structural biology* 155.1 (2006), pp. 63–73.

[45] G. Knott et al. "Serial section scanning electron microscopy of adult brain tissue using focused ion beam milling". *Journal of Neuroscience* 28.12 (2008), pp. 2959–2964.

[46] K. D. Micheva and S. J. Smith. "Array tomography: a new tool for imaging the molecular architecture and ultrastructure of neural circuits". *Neuron* 55.1 (2007), pp. 25–36.

[47] I. Wacker and R. Schroeder. "Array tomography". *Journal of microscopy* 252.2 (2013), pp. 93–99.

[48] K. Hayworth et al. "Automating the collection of ultrathin serial sections for large volume TEM reconstructions". *Microscopy and Microanalysis* 12.S02 (2006), pp. 86–87.

[49] R. Schalek et al. "ATUM-based SEM for high-speed large-volume biological reconstructions". *Microscopy and Microanalysis* 18.S2 (2012), pp. 572–573.

[50] A. Kremer et al. "Developing 3D SEM in a broad biological context". *Journal of microscopy* 259.2 (2015), pp. 80–96.

[51] B. Titze and C. Genoud. "Volume scanning electron microscopy for imaging biological ultrastructure". *Biology of the Cell* 108.11 (2016), pp. 307–323.

[52] D. Smith and T. Starborg. "Serial block face scanning electron microscopy in cell biology: Applications and technology". *Tissue and Cell* 57 (2019), pp. 111–122.

[53] V. Baena et al. "FIB-SEM as a Volume Electron Microscopy Approach to Study Cellular Architectures in SARS-CoV-2 and Other Viral Infections: A Practical Primer for a Virologist". *Viruses* 13.4 (2021), p. 611.

[54] G. Wolff and M. Bárcena. "Multiscale Electron Microscopy for the Study of Viral Replication Organelles". *Viruses* 13.2 (2021), p. 197.

[55] K. Narayan and S. Subramaniam. "Focused ion beams in biology". *Nature methods* 12.11 (2015), pp. 1021–1031.

[56] L. K. Scheffer et al. "A Connectome and Analysis of the Adult Drosophila Central Brain". *BioRxiv* (2020).

[57] W. Yin et al. "A petascale automated imaging pipeline for mapping neuronal circuits with high-throughput transmission electron microscopy". *Nature communications* 11.1 (2020), pp. 1–12.

[58] M. Helmstaedter et al. "Connectomic reconstruction of the inner plexiform layer in the mouse retina". *Nature* 500.7461 (2013), pp. 168–174.

[59] A. Motta et al. "Dense connectomic reconstruction in layer 4 of the somatosensory cortex". *Science* 366.6469 (2019).

[60] A. Eberle et al. "High-resolution, high-throughput imaging with a multibeam scanning electron microscope". *Journal of microscopy* 259.2 (2015), pp. 114–120.

[61] K. J. Hayworth et al. "Ultrastructurally smooth thick partitioning and volume stitching for large-scale connectomics". *Nature methods* 12.4 (2015), pp. 319–322.

[62] D. D. Bock et al. "Network anatomy and in vivo physiology of visual cortical neurons". *Nature* 471.7337 (2011), pp. 177–182.

[63] C. S. Xu et al. "Enhanced FIB-SEM systems for large-volume 3D imaging". *Elife* 6 (2017), e25916.

[64] J. S. Phelps et al. "Reconstruction of motor control circuits in adult Drosophila using automated transmission electron microscopy". *Cell* 184.3 (2021), pp. 759–774.

[65] J. Kornfeld and W. Denk. "Progress and remaining challenges in high-throughput volume electron microscopy". *Current opinion in neurobiology* 50 (2018), pp. 261–267.

[66] N. Kasthuri et al. "Saturated reconstruction of a volume of neocortex". *Cell* 162.3 (2015), pp. 648–661.

[67] D. Witvliet et al. "Connectomes across development reveal principles of brain maturation". *BioRxiv* (2021), pp. 2020–04.

[68] A. Shapson-Coe et al. "A connectomic study of a petascale fragment of human cerebral cortex". *BioRxiv* (2021).

[69] C. Pinali et al. "Three-dimensional reconstruction of cardiac sarcoplasmic reticulum reveals a continuous network linking transverse-tubules: this organization is perturbed in heart failure". *Circulation research* 113.11 (2013), pp. 1219–1230.

[70] C. S. Xu et al. “Transforming fib-sem systems for large-volume connectomics and cell biology”. *Volume Microscopy*. Springer, 2020, pp. 221–243.

[71] J. P. Schneider, J. Hegermann, and C. Wrede. “Volume electron microscopy: analyzing the lung”. *Histochemistry and Cell Biology* (2020), pp. 1–20.

[72] J. A. Bae et al. “Functional connectomics spanning multiple areas of mouse visual cortex”. *bioRxiv* (2021).

[73] A. Machireddy et al. “Robust Segmentation of Cellular Ultrastructure on Sparsely Labeled 3D Electron Microscopy Images using Deep Learning”. *Available at SSRN 3830021* (2021).

[74] D. Wei et al. “High-resolution three-dimensional reconstruction of a whole yeast cell using focused-ion beam scanning electron microscopy”. *Biotechniques* 53.1 (2012), pp. 41–48.

[75] L. Hughes et al. “Patterns of organelle ontogeny through a cell cycle revealed by whole-cell reconstructions using 3D electron microscopy”. *Journal of cell science* 130.3 (2017), pp. 637–647.

[76] H. M. Vergara et al. “Whole-body integration of gene expression and single-cell morphology”. *Cell* 184.18 (2021), pp. 4819–4837.

[77] H. E. Armer et al. “Imaging transient blood vessel fusion events in zebrafish by correlative volume electron microscopy”. *PLoS One* 4.11 (2009), e7716.

[78] R. B. Svensson et al. “Evidence of structurally continuous collagen fibrils in tendons”. *Acta Biomaterialia* 50 (2017), pp. 293–301.

[79] G. Parlakgül et al. “Regulation of liver subcellular architecture controls metabolic homeostasis”. *Nature* 603.7902 (2022), pp. 736–742.

[80] S. J. Cook et al. “Whole-animal connectomes of both Caenorhabditis elegans sexes”. *Nature* 571.7763 (2019), pp. 63–71.

[81] T. Ohyama et al. “A multilevel multimodal circuit enhances action selection in Drosophila”. *Nature* 520.7549 (2015), pp. 633–639.

[82] J. Buhmann et al. “Automatic detection of synaptic partners in a whole-brain Drosophila electron microscopy data set”. *Nature Methods* (2021), pp. 1–4.

[83] S.-y. Takemura et al. “A connectome of a learning and memory center in the adult Drosophila brain”. *Elife* 6 (2017), e26975.

[84] W. F. Tobin, R. I. Wilson, and W.-C. A. Lee. “Wiring variations that enable and constrain neural computation in a sensory microcircuit”. *Elife* 6 (2017), e24838.

[85] A. Vishwanathan et al. “Electron microscopic reconstruction of functionally identified cells in a neural integrator”. *Current Biology* 27.14 (2017), pp. 2137–2147.

[86] N. N. Guan et al. “A specialized spinal circuit for command amplification and directionality during escape behavior”. *Proceedings of the National Academy of Sciences* 118.42 (2021).

[87] Y. Hua et al. “Electron Microscopic Reconstruction of Neural Circuitry in the Cochlea”. *Cell Reports* 34.1 (2021), p. 108551.

[88] G. S. Tomassy et al. “Distinct profiles of myelin distribution along single axons of pyramidal neurons in the neocortex”. *Science* 344.6181 (2014), pp. 319–324.

[89] W.-C. A. Lee et al. “Anatomy and function of an excitatory network in the visual cortex”. *Nature* 532.7599 (2016), pp. 370–374.

[90] J. L. Morgan et al. “The fuzzy logic of network connectivity in mouse visual thalamus”. *Cell* 165.1 (2016), pp. 192–206.

[91] R. L. Felts et al. “3D visualization of HIV transfer at the virological synapse between dendritic cells and T cells”. *Proceedings of the National Academy of Sciences* 107.30 (2010), pp. 13336–13341.

[92] H. Vihinen, I. Belevich, and E. Jokitalo. “Three dimensional electron microscopy of cellular organelles by serial block face SEM and ET”. *Microsc. Anal* 27 (2013), pp. 7–10.

[93] D. P. Hoffman et al. “Correlative three-dimensional super-resolution and block-face electron microscopy of whole vitreously frozen cells”. *Science* 367.6475 (2020).

[94] D. Cretoiu et al. “Human cardiac telocytes: 3D imaging by FIB-SEM tomography”. *Journal of cellular and molecular medicine* 18.11 (2014), pp. 2157–2164.

[95] J. P. Schneider, C. Wrede, and C. Mühlfeld. “The three-dimensional ultrastructure of the human alveolar epithelium revealed by focused ion beam electron microscopy”. *International journal of molecular sciences* 21.3 (2020), p. 1089.

[96] A. Mohammadi-Gheidari, C. Hagen, and P. Kruit. “Multibeam scanning electron microscope: experimental results”. *Journal of Vacuum Science & Technology B, Nanotechnology and Microelectronics: Materials, Processing, Measurement, and Phenomena* 28.6 (2010), C6G5–C6G10.

[97] D. Meisburger et al. “Proposed architecture of a multicolumn electron-beam wafer inspection system for high-volume manufacturing”. *Journal of Vacuum Science & Technology B, Nanotechnology and Microelectronics: Materials, Processing, Measurement, and Phenomena* 33.6 (2015), 06FN01.

[98] T. Kemen et al. “Further advancing the throughput of a multi-beam SEM”. *Metrology, Inspection, and Process Control for Microlithography XXIX*. Vol. 9424. International Society for Optics and Photonics. 2015, 94241U.

[99] C. Riedesel et al. “First demonstration of a 331-beam SEM”. *Metrology, Inspection, and Process Control for Microlithography XXXIII*. Vol. 10959. International Society for Optics and Photonics. 2019, p. 1095931.

[100] S. Shibata et al. “Large-area fluorescence and electron microscopic correlative imaging with multibeam scanning electron microscopy”. *Frontiers in neural circuits* 13 (2019), p. 29.

[101] A. Günther et al. “Double cones and the diverse connectivity of photoreceptors and bipolar cells in an avian retina”. *Journal of Neuroscience* 41.23 (2021), pp. 5015–5028.

[102] B. J. Graham et al. “High-throughput transmission electron microscopy with automated serial sectioning”. *Biorxiv* (2019), p. 657346.

[103] K. J. Hayworth et al. “Gas cluster ion beam SEM for imaging of large tissue samples with 10 nm isotropic resolution”. *Nature methods* 17.1 (2020), pp. 68–71.

[104] B. Winiarski et al. “Broad ion beam serial section tomography”. *Ultramicroscopy* 172 (2017), pp. 52–64.

[105] T. Burnett et al. “Large volume serial section tomography by Xe Plasma FIB dual beam microscopy”. *Ultramicroscopy* 161 (2016), pp. 119–129.

[106] A. Gholinia et al. “Coupled Broad Ion Beam-Scanning Electron Microscopy (BIB-SEM) for polishing and three dimensional (3D) Serial Section Tomography (SST)”. *Ultramicroscopy* (2020), p. 112989.

[107] G. Sergey et al. “Oxygen plasma focused ion beam scanning electron microscopy for biological samples”. *BioRxiv* (2018), p. 457820.

[108] G. Kislinger et al. “Multiscale ATUM-FIB microscopy enables targeted ultrastructural analysis at isotropic resolution”. *Iscience* 23.7 (2020), p. 101290.

[109] H. Schmidt et al. “Axonal synapse sorting in medial entorhinal cortex”. *Nature* 549.7673 (2017), pp. 469–475.

[110] A. M. Seligman, H. L. Wasserkrug, and J. S. Hanker. “A new staining method (OTO) for enhancing contrast of lipid-containing membranes and droplets in osmium tetroxide-fixed tissue with osmiophilic thiocarbohydrazide (TCH)”. *The Journal of cell biology* 30.2 (1966), p. 424.

[111] J. C. Tapia et al. “High-contrast en bloc staining of neuronal tissue for field emission scanning electron microscopy”. *Nature protocols* 7.2 (2012), p. 193.

[112] Y. Hua, P. Laserstein, and M. Helmstaedter. “Large-volume en-bloc staining for electron microscopy-based connectomics”. *Nature communications* 6.1 (2015), pp. 1–7.

[113] S. Mikula and W. Denk. “High-resolution whole-brain staining for electron microscopic circuit reconstruction”. *Nature methods* 12.6 (2015), pp. 541–546.

[114] C. Genoud et al. “Fast homogeneous en bloc staining of large tissue samples for volume electron microscopy”. *Frontiers in neuroanatomy* 12 (2018), p. 76.

[115] I. Wacker et al. “Hierarchical imaging: a new concept for targeted imaging of large volumes from cells to tissues”. *BMC cell biology* 17.1 (2016), pp. 1–12.

[116] T. Koike et al. “A device for ribbon collection for array tomography with scanning electron microscopy”. *Acta Histochemica et Cytochemica* 50.5 (2017), pp. 135–140.

[117] T. J. Lee et al. “Large-scale neuroanatomy using LASSO: loop-based automated serial sectioning operation”. *PLoS One* 13.10 (2018), e0206172.

[118] Y. Kubota et al. “A carbon nanotube tape for serial-section electron microscopy of brain ultrastructure”. *Nature communications* 9.1 (2018), pp. 1–15.

[119] T. Templier. “MagC, magnetic collection of ultrathin sections for volumetric correlative light and electron microscopy”. *Elife* 8 (2019), e45696.

[120] T. J. Deerinck et al. “High-performance serial block-face SEM of nonconductive biological samples enabled by focal gas injection-based charge compensation”. *Journal of microscopy* 270.2 (2018), pp. 142–149.

[121] B. Titze and W. Denk. “Automated in-chamber specimen coating for serial block-face electron microscopy”. *Journal of microscopy* 250.2 (2013), pp. 101–110.

[122] A. A. Wanner et al. “Dense EM-based reconstruction of the interglomerular projectome in the zebrafish olfactory bulb”. *Nature neuroscience* 19.6 (2016), pp. 816–825.

[123] H. B. Nguyen et al. “Conductive resins improve charging and resolution of acquired images in electron microscopic volume imaging”. *Scientific reports* 6.1 (2016), pp. 1–10.

[124] T. Q. Thai et al. “Rapid specimen preparation to improve the throughput of electron microscopic volume imaging for three-dimensional analyses of subcellular ultrastructures with serial block-face scanning electron microscopy”. *Medical molecular morphology* 49.3 (2016), pp. 154–162.

[125] X. Heiligenstein et al. “HPM live μ for a full CLEM workflow”. *Methods in Cell Biology*. Vol. 162. Elsevier, 2021, pp. 115–149.

[126] M. Guizar-Sicairos, S. T. Thurman, and J. R. Fienup. “Efficient subpixel image registration algorithms”. *Optics letters* 33.2 (2008), pp. 156–158.

[127] D. G. Lowe. “Object recognition from local scale-invariant features”. *Proceedings of the seventh IEEE international conference on computer vision*. Vol. 2. Ieee. 1999, pp. 1150–1157.

[128] H. Bay et al. “Speeded-up robust features (SURF)”. *Computer vision and image understanding* 110.3 (2008), pp. 346–359.

[129] M. A. Fischler and R. C. Bolles. “Random sample consensus: a paradigm for model fitting with applications to image analysis and automated cartography”. *Communications of the ACM* 24.6 (1981), pp. 381–395.

[130] J. R. Anderson et al. “Exploring the retinal connectome”. *Molecular vision* 17 (2011), p. 355.

[131] P. Thevenaz, U. Ruttimann, and M. Unser. “A pyramid approach to subpixel registration based on intensity”. *IEEE Transactions on Image Processing* 7.1 (1998), pp. 27–41.

[132] K. Khairy, G. Denisov, and S. Saalfeld. “Joint deformable registration of large EM image volumes: a matrix solver approach”. *arXiv preprint arXiv:1804.10019* (2018).

[133] A. Cardona et al. “TrakEM2 software for neural circuit reconstruction”. *PloS one* 7.6 (2012), e38011.

[134] J. R. Kremer, D. N. Mastronarde, and J. R. McIntosh. “Computer visualization of three-dimensional image data using IMOD”. *Journal of structural biology* 116.1 (1996), pp. 71–76.

[135] I. Belevich et al. “Microscopy image browser: a platform for segmentation and analysis of multidimensional datasets”. *PLoS biology* 14.1 (2016), e1002340.

[136] A. W. Wetzel et al. “Registering large volume serial-section electron microscopy image sets for neural circuit reconstruction using FFT signal whitening”. *2016 IEEE Applied Imagery Pattern Recognition Workshop (AIPR)*. IEEE. 2016, pp. 1–10.

[137] S. Saalfeld et al. “CATMAID: collaborative annotation toolkit for massive amounts of image data”. *Bioinformatics* 25.15 (2009), pp. 1984–1986.

[138] M. Helmstaedter, K. L. Briggman, and W. Denk. “High-accuracy neurite reconstruction for high-throughput neuroanatomy”. *Nature neuroscience* 14.8 (2011), pp. 1081–1088.

[139] K. M. Boergens et al. “webKnossos: efficient online 3D data annotation for connectomics”. *nature methods* 14.7 (2017), pp. 691–694.

[140] D. R. Berger, H. S. Seung, and J. W. Lichtman. “VAST (volume annotation and segmentation tool): efficient manual and semi-automatic labeling of large 3D image stacks”. *Frontiers in neural circuits* 12 (2018), p. 88.

[141] J. Kornfeld, F. Svara, and A. A. Wanner. “Image processing for volume electron microscopy”. *Volume Microscopy.* Springer, 2020, pp. 245–262.

[142] V. Jain et al. “Supervised learning of image restoration with convolutional networks”. *2007 IEEE 11th International Conference on Computer Vision.* IEEE. 2007, pp. 1–8.

[143] I. Arganda-Carreras et al. “Crowdsourcing the creation of image segmentation algorithms for connectomics”. *Frontiers in neuroanatomy* 9 (2015), p. 142.

[144] O. Ronneberger, P. Fischer, and T. Brox. “U-net: Convolutional networks for biomedical image segmentation”. *International Conference on Medical image computing and computer-assisted intervention.* Springer. 2015, pp. 234–241.

[145] Ö. Çiçek et al. “3D U-Net: learning dense volumetric segmentation from sparse annotation”. *International conference on medical image computing and computer-assisted intervention.* Springer. 2016, pp. 424–432.

[146] T. M. Quan, D. G. Hildebrand, and W.-K. Jeong. “Fusionnet: A deep fully residual convolutional neural network for image segmentation in connectomics”. *arXiv preprint arXiv:1612.05360* (2016).

[147] A. Fakhry, T. Zeng, and S. Ji. “Residual deconvolutional networks for brain electron microscopy image segmentation”. *IEEE transactions on medical imaging* 36.2 (2016), pp. 447–456.

[148] T. Zeng, B. Wu, and S. Ji. “DeepEM3D: approaching human-level performance on 3D anisotropic EM image segmentation”. *Bioinformatics* 33.16 (2017), pp. 2555–2562.

[149] T. Beier et al. “Multicut brings automated neurite segmentation closer to human performance”. *Nature methods* 14.2 (2017), pp. 101–102.

[150] K. Lee et al. “Superhuman accuracy on the SNEMI3D connectomics challenge”. *arXiv preprint arXiv:1706.00120* (2017).

[151] J. Funke et al. “Large scale image segmentation with structured loss based deep learning for connectome reconstruction”. *IEEE transactions on pattern analysis and machine intelligence* 41.7 (2018), pp. 1669–1680.

[152] M. Januszewski et al. “Flood-filling networks”. *arXiv preprint arXiv:1611.00421* (2016).

[153] M. Januszewski et al. “High-precision automated reconstruction of neurons with flood-filling networks”. *Nature methods* 15.8 (2018), pp. 605–610.

[154] K. Lee et al. “Convolutional nets for reconstructing neural circuits from brain images acquired by serial section electron microscopy”. *Current opinion in neurobiology* 55 (2019), pp. 188–198.

[155] A. Kreshuk et al. “Automated detection and segmentation of synaptic contacts in nearly isotropic serial electron microscopy images”. *PloS one* 6.10 (2011), e24899.

[156] A. Kreshuk et al. “Automated detection of synapses in serial section transmission electron microscopy image stacks”. *PloS one* 9.2 (2014), e87351.

[157] W. G. Roncal et al. “Volumetric exploitation of synaptic information using context localization and evaluation”. *arXiv preprint arXiv:1403.3724* (2014).

[158] G. B. Huang and S. Plaza. “Identifying synapses using deep and wide multiscale recursive networks”. *arXiv preprint arXiv:1409.1789* (2014).

[159] S. Dorkenwald et al. “Automated synaptic connectivity inference for volume electron microscopy”. *Nature methods* 14.4 (2017), pp. 435–442.

[160] S. Santurkar et al. “Toward streaming synapse detection with compositional convnets”. *arXiv preprint arXiv:1702.07386* (2017).

[161] B. Staffler et al. “SynEM, automated synapse detection for connectomics”. *Elife* 6 (2017), e26414.

[162] G. B. Huang, L. K. Scheffer, and S. M. Plaza. “Fully-automatic synapse prediction and validation on a large data set”. *Frontiers in neural circuits* 12 (2018), p. 87.

[163] L. Heinrich et al. “Synaptic cleft segmentation in non-isotropic volume electron microscopy of the complete drosophila brain”. *International Conference on Medical Image Computing and Computer-Assisted Intervention*. Springer. 2018, pp. 317–325.

[164] J. Buhmann et al. “Synaptic partner prediction from point annotations in insect brains”. *International Conference on Medical Image Computing and Computer-Assisted Intervention*. Springer. 2018, pp. 309–316.

[165] H. Spiers et al. “Deep learning for automatic segmentation of the nuclear envelope in electron microscopy data, trained with volunteer segmentations”. *Traffic* (2021).

[166] K. L. Briggman, M. Helmstaedter, and W. Denk. “Wiring specificity in the direction-selectivity circuit of the retina”. *Nature* 471.7337 (2011), pp. 183–188.

[167] J. S. Kim et al. “Space–time wiring specificity supports direction selectivity in the retina”. *Nature* 509.7500 (2014), pp. 331–336.

[168] S. Dorkenwald et al. “Flywire: Online Community for whole-brain connectomics”. *Nature Methods* 19.1 (2021), pp. 119–128. DOI: `10.1038/s41592-021-01330-0`.

[169] D. Wei et al. “Mitoem dataset: Large-scale 3d mitochondria instance segmentation from em images”. *International Conference on Medical Image Computing and Computer-Assisted Intervention*. Springer. 2020, pp. 66–76.

[170] R. Conrad and K. Narayan. “CEM500K, a large-scale heterogeneous unlabeled cellular electron microscopy image dataset for deep learning”. *Elife* 10 (2021), e65894.

[171] I. Oztel et al. “Mitochondria segmentation in electron microscopy volumes using deep convolutional neural network”. *2017 IEEE International Conference on Bioinformatics and Biomedicine (BIBM)*. IEEE. 2017, pp. 1195–1200.

[172] M. Ž. Mekuč et al. “Automatic segmentation of mitochondria and endolysosomes in volumetric electron microscopy data”. *Computers in biology and medicine* 119 (2020), p. 103693.

[173] L. Nightingale et al. “Automatic instance segmentation of mitochondria in electron microscopy data”. *bioRxiv* (2021).

[174] C. Karabağ et al. “Segmentation and modelling of the nuclear envelope of hela cells imaged with serial block face scanning electron microscopy”. *Journal of Imaging* 5.9 (2019), p. 75.

[175] C. Karabağ, M. L. Jones, and C. C. Reyes-Aldasoro. “Volumetric Semantic Instance Segmentation of the Plasma Membrane of HeLa Cells”. *Journal of Imaging* 7.6 (2021), p. 93.

[176] X. Zhang et al. “A unified deep-learning network to accurately segment insulin granules of different animal models imaged under different electron microscopy methodologies”. *Protein & cell* 10.4 (2019), pp. 306–311.

[177] C. Meyer et al. “Automatic Multi Class Organelle Segmentation For Cellular Fib-Sem Images”. *2021 IEEE 18th International Symposium on Biomedical Imaging (ISBI)*. IEEE. 2021, pp. 668–672.

[178] M. G. Haberl et al. “CDeep3M-Plug-and-Play cloud-based deep learning for image segmentation”. *Nature methods* 15.9 (2018), pp. 677–680.

[179] S. C. Turaga et al. “Maximin affinity learning of image segmentation”. *arXiv preprint arXiv:0911.5372* (2009).

[180] D. Linsley et al. “Robust neural circuit reconstruction from serial electron microscopy with convolutional recurrent networks”. *arXiv preprint arXiv:1811.11356* (2018).

[181] M. Januszewski and V. Jain. “Segmentation-Enhanced CycleGAN”. *bioRxiv* (2019), p. 548081.

[182] J. Roels et al. “Domain adaptive segmentation in volume electron microscopy imaging”. *2019 IEEE 16th International Symposium on Biomedical Imaging (ISBI 2019)*. IEEE. 2019, pp. 1519–1522.

[183] I. Arganda-Carreras et al. “Trainable Weka Segmentation: a machine learning tool for microscopy pixel classification”. *Bioinformatics* 33.15 (2017), pp. 2424–2426.

[184] E. Gómez-de-Mariscal et al. "DeepImageJ: A user-friendly plugin to run deep learning models in ImageJ". *bioRxiv* (2019), p. 799270.

[185] S. Berg et al. "Ilastik: interactive machine learning for (bio) image analysis". *Nature Methods* (2019), pp. 1–7.

[186] I. Belevich and E. Jokitalo. "DeepMIB: user-friendly and open-source software for training of deep learning network for biological image segmentation". *PLoS computational biology* 17.3 (2021), e1008374.

[187] H. Urakubo et al. "UNI-EM: an environment for deep neural network-based automated segmentation of neuronal electron microscopic images". *Scientific reports* 9.1 (2019), pp. 1–9.

[188] L. von Chamier et al. "Democratising deep learning for microscopy with ZeroCostDL4Mic". *Nature communications* 12.1 (2021), p. 2276.

[189] A. Iudin et al. "EMPIAR: a public archive for raw electron microscopy image data". *Nature methods* 13.5 (2016), pp. 387–388.

[190] E. Williams et al. "Image Data Resource: a bioimage data integration and publication platform". *Nature methods* 14.8 (2017), pp. 775–781.

[191] M. D. Wilkinson et al. "The FAIR Guiding Principles for scientific data management and stewardship". *Scientific data* 3.1 (2016), pp. 1–9.

[192] U. Sarkans et al. "REMBI: Recommended Metadata for Biological Images-enabling reuse of microscopy data in biology". *Nature methods* (2021), pp. 1–5.

[193] J. Moore et al. "OME-NGFF: scalable format strategies for interoperable bioimaging data". *BioRxiv* (2021).

[194] T. Zhao et al. "Neutu: software for collaborative, large-scale, segmentation-based connectome reconstruction". *Frontiers in Neural Circuits* 12 (2018), p. 101.

[195] C. Allan et al. "OMERO: flexible, model-driven data management for experimental biology". *Nature methods* 9.3 (2012), pp. 245–253.

[196] M. Linkert et al. "Metadata matters: access to image data in the real world". *Journal of Cell Biology* 189.5 (2010), pp. 777–782.

[197] J. T. Vogelstein et al. "A community-developed open-source computational ecosystem for big neuro data". *Nature methods* 15.11 (2018), pp. 846–847.

[198] R. Hider Jr et al. "The brain observatory storage service and database (BossDB): a cloud-native approach for petascale neuroscience discovery". *Frontiers in Neuroinformatics* 16 (2022), p. 828787.

[199] C. S. Xu et al. "An open-access volume electron microscopy atlas of whole cells and tissues". *bioRxiv* (2021), pp. 2020–11.

[200] R. Vescovi et al. "Toward an Automated HPC Pipeline for Processing Large Scale Electron Microscopy Data". *2020 IEEE/ACM 2nd Annual Workshop on Extreme-scale Experiment-in-the-Loop Computing (XLOOP)*. IEEE. 2020, pp. 16–22.

[201] W. T. Katz and S. M. Plaza. "DVID: distributed versioned Image-Oriented dataservice". *Frontiers in neural circuits* 13 (2019), p. 5.

[202] T. Pietzsch et al. "BigDataViewer: visualization and processing for large image data sets". *Nature methods* 12.6 (2015), pp. 481–483.

[203] S. Kume. "Short Review: Pathology of the image big data era using electron microscopy". *arXiv preprint arXiv:2111.13627* (2021).

[204] C. Cali et al. "The effects of aging on neuropil structure in mouse somatosensory cortex-A 3D electron microscopy analysis of layer 1". *PLoS One* 13.7 (2018), e0198131.

[205] A. Gour et al. "Postnatal connectomic development of inhibition in mouse barrel cortex". *Science* 371.6528 (2021).

[206] A. Badea, A. Ali-Sharief, and G. A. Johnson. "Morphometric analysis of the C57BL/6J mouse brain". *Neuroimage* 37.3 (2007), pp. 683–693.

[207] G. Wanner, T. Schäfer, and U. Lütz-Meindl. “3-D analysis of dictyosomes and multivesicular bodies in the green alga Micrasterias denticulata by FIB/SEM tomography”. *Journal of Structural Biology* 184.2 (2013), pp. 203–211.

[208] D. Scheuring et al. “Actin-dependent vacuolar occupancy of the cell determines auxin-induced growth repression”. *Proceedings of the National Academy of Sciences* 113.2 (2016), pp. 452–457.

[209] K. M. Furuta et al. “Arabidopsis NAC45/86 direct sieve element morphogenesis culminating in enucleation”. *Science* 345.6199 (2014), pp. 933–937.

[210] J. P. Remis et al. “Bacterial social networks: structure and composition of M yxococcus xanthus outer membrane vesicle chains”. *Environmental microbiology* 16.2 (2014), pp. 598–610.

[211] A. Schertel et al. “Cryo FIB-SEM: volume imaging of cellular ultrastructure in native frozen specimens”. *Journal of structural biology* 184.2 (2013), pp. 355–360.

[212] A. J. Bushby et al. “Imaging three-dimensional tissue architectures by focused ion beam scanning electron microscopy”. *Nature protocols* 6.6 (2011), pp. 845–858.

[213] N. S. Kalson et al. “Nonmuscle myosin II powered transport of newly formed collagen fibrils at the plasma membrane”. *Proceedings of the National Academy of Sciences* 110.49 (2013), E4743–E4752.

[214] M. Y. Rennie et al. “3D imaging of the early embryonic chicken heart with focused ion beam scanning electron microscopy”. *Microscopy and Microanalysis* 20.4 (2014), pp. 1111–1119.

[215] S.-y. Takemura et al. “Synaptic circuits and their variations within different columns in the visual system of Drosophila”. *Proceedings of the National Academy of Sciences* 112.44 (2015), pp. 13711–13716.

[216] K. M. Boergens et al. “Full reconstruction of large lobula plate tangential cells in Drosophila from a 3D EM dataset”. *Plos one* 13.11 (2018), e0207828.

[217] S.-y. Takemura et al. “A visual motion detection circuit suggested by Drosophila connectomics”. *Nature* 500.7461 (2013), pp. 175–181.

[218] P. Ronchi et al. “High-precision targeting workflow for volume electron microscopy”. *Journal of Cell Biology* 220.9 (2021), e202104069.

[219] S. Gerhard et al. “Conserved neural circuit structure across Drosophila larval development revealed by comparative connectomics”. *Elife* 6 (2017), e29089.

[220] A. Cardona et al. “An integrated micro-and macroarchitectural analysis of the Drosophila brain by computer-assisted serial section electron microscopy”. *PLoS biology* 8.10 (2010), e1000502.

[221] C. L. Schwartz et al. “A detailed, hierarchical study of Giardia lamblia’s ventral disc reveals novel microtubule-associated protein complexes” (2012).

[222] A. Pollreisz et al. “Visualizing melanosomes, lipofuscin, and melanolipofuscin in human retinal pigment epithelium using serial block face scanning electron microscopy”. *Experimental eye research* 166 (2018), pp. 131–139.

[223] M. T. Arévalo et al. “Primary human endothelial cells support direct but not antibody-dependent enhancement of dengue viral infection”. *Journal of medical virology* 81.3 (2009), pp. 519–528.

[224] J. Y. Mun et al. “A low fluence Q-switched Nd: YAG laser modifies the 3D structure of melanocyte and ultrastructure of melanosome by subcellular-selective photothermolysis”. *Journal of electron microscopy* 60.1 (2010), pp. 11–18.

[225] C. Villinger et al. “FIB/SEM tomography with TEM-like resolution for 3D imaging of high-pressure frozen cells”. *Histochemistry and cell biology* 138.4 (2012), pp. 549–556.

[226] T. Do et al. “Three-dimensional imaging of HIV-1 virological synapses reveals membrane architectures involved in virus transmission”. *Journal of virology* 88.18 (2014), pp. 10327–10339.

[227] A. E. Bennett et al. “Ion-abrasion scanning electron microscopy reveals surface-connected tubular conduits in HIV-infected macrophages”. *PLoS pathogens* 5.9 (2009), e1000591.

[228] M. Klose et al. “FIB-SEM-based analysis of Borrelia intracellular processing by human macrophages”. *Journal of cell science* 134.5 (2021), jcs252320.

[229] E. B. Bloss et al. “Single excitatory axons form clustered synapses onto CA1 pyramidal cell dendrites”. *Nature neuroscience* 21.3 (2018), pp. 353–363.

[230] D. V. Bohórquez et al. “An enteroendocrine cell–enteric glia connection revealed by 3D electron microscopy”. *PloS one* 9.2 (2014), e89881.

[231] H. Ding et al. “Species-specific wiring for direction selectivity in the mammalian retina”. *Nature* 535.7610 (2016), pp. 105–110.

[232] M. E. Coulter et al. “The ESCRT-III protein CHMP1A mediates secretion of sonic hedgehog on a distinctive subtype of extracellular vesicles”. *Cell reports* 24.4 (2018), pp. 973–986.

[233] F. Drawitsch et al. “FluoEM, virtual labeling of axons in three-dimensional electron microscopy data for long-range connectomics”. *Elife* 7 (2018), e38976.

[234] A. Karimi et al. “Cell-type specific innervation of cortical pyramidal cells at their apical dendrites”. *Elife* 9 (2020), e46876.

[235] O. Thaunat et al. “Asymmetric segregation of polarized antigen on B cell division shapes presentation capacity”. *Science* 335.6067 (2012), pp. 475–479.

[236] C. Pfeifer et al. “Quantitative analysis of mouse pancreatic islet architecture by serial block-face SEM”. *Journal of structural biology* 189.1 (2015), pp. 44–52.

[237] A. Rao et al. “Determination of secretory granule maturation times in pancreatic islet β-cells by serial block-face electron microscopy”. *Journal of Structural Biology* 212.1 (2020), p. 107584.

[238] B. G. Kopek et al. “Correlative 3D superresolution fluorescence and electron microscopy reveal the relationship of mitochondrial nucleoids to membranes”. *Proceedings of the National Academy of Sciences* 109.16 (2012), pp. 6136–6141.

[239] L. C. Soares Medeiros et al. “Visualizing the 3D architecture of multiple erythrocytes infected with Plasmodium at nanoscale by focused ion beam-scanning electron microscopy”. *PLoS One* 7.3 (2012), e33445.

[240] G. E. Murphy et al. “Ion-abrasion scanning electron microscopy reveals distorted liver mitochondrial morphology in murine methylmalonic acidemia”. *Journal of structural biology* 171.2 (2010), pp. 125–132.

[241] P. Schneider et al. “Serial FIB/SEM imaging for quantitative 3D assessment of the osteocyte lacuno-canalicular network”. *Bone* 49.2 (2011), pp. 304–311.

[242] P. S. Holcomb et al. “Synaptic inputs compete during rapid formation of the calyx of Held: a new model system for neural development”. *Journal of Neuroscience* 33.32 (2013), pp. 12954–12969.

[243] J. Rodriguez-Moreno et al. “Quantitative 3D ultrastructure of thalamocortical synapses from the ”lemniscal” ventral posteromedial nucleus in mouse barrel cortex”. *Cerebral Cortex* 28.9 (2018), pp. 3159–3175.

[244] C. Bosch et al. “FIB/SEM technology and high-throughput 3D reconstruction of dendritic spines and synapses in GFP-labeled adult-generated neurons”. *Frontiers in neuroanatomy* 9 (2015), p. 60.

[245] G. Wildenberg et al. “Partial connectomes of labeled dopaminergic circuits reveal non-synaptic communication and axonal remodeling after exposure to cocaine”. *Elife* 10 (2021), e71981.

[246] A. M. Wilson et al. “Developmental rewiring between cerebellar climbing fibers and Purkinje cells begins with positive feedback synapse addition”. *Cell reports* 29.9 (2019), pp. 2849–2861.

[247] R. E. Marc et al. “The AII amacrine cell connectome: a dense network hub”. *Frontiers in neural circuits* 8 (2014), p. 104.

[248] R. Rezakhaniha et al. “Role of elastin anisotropy in structural strain energy functions of arterial tissue”. *Biomechanics and modeling in mechanobiology* 10.4 (2011), pp. 599–611.

[249] C. Calì et al. “3D cellular reconstruction of cortical glia and parenchymal morphometric analysis from Serial Block-Face Electron Microscopy of juvenile rat”. *Progress in neurobiology* 183 (2019), p. 101696.

[250] T. Kikuchi et al. “Volume electron microscopy study of the relationship between synapses and astrocytes in the developing rat somatosensory cortex”. *Cerebral Cortex* 30.6 (2020), pp. 3800–3819.

[251] R. A. Salo et al. “Quantification of anisotropy and orientation in 3D electron microscopy and diffusion tensor imaging in injured rat brain”. *Neuroimage* 172 (2018), pp. 404–414.

[252] J. Rouquette et al. “Revealing the high-resolution three-dimensional network of chromatin and interchromatin space: a novel electron-microscopic approach to reconstructing nuclear architecture”. *Chromosome research* 17.6 (2009), pp. 801–810.

[253] K. Ichimura et al. “Three-dimensional architecture of podocytes revealed by block-face scanning electron microscopy”. *Scientific reports* 5.1 (2015), pp. 1–7.

[254] Y. Mishchenko et al. “Ultrastructural analysis of hippocampal neuropil from the connectomics perspective”. *Neuron* 67.6 (2010), pp. 1009–1020.

[255] N. Vidavsky et al. “Calcium transport into the cells of the sea urchin larva in relation to spicule formation”. *Proceedings of the National Academy of Sciences* 113.45 (2016), pp. 12637–12642.

[256] K. Scott. “3D elemental and structural analysis of biological specimens using electrons and ions”. *Journal of microscopy* 242.1 (2011), pp. 86–93.

[257] S. Mursalimov et al. “Serial Block-Face Scanning Electron Microscopy Reveals That Intercellular Nuclear Migration Occurs in Most Normal Tobacco Male Meiocytes”. *Frontiers in Plant Science* 12 (2021), p. 775.

[258] J. Kornfeld et al. “EM connectomics reveals axonal target variation in a sequence-generating network”. *Elife* 6 (2017), e24364.

[259] P. J. Lafontant et al. “Cardiac myocyte diversity and a fibroblast network in the junctional region of the zebrafish heart revealed by transmission and serial block-face scanning electron microscopy”. *PloS one* 8.8 (2013), e72388.

[260] F. N. Svara et al. “Volume EM reconstruction of spinal cord reveals wiring specificity in speed-related motor circuits”. *Cell reports* 23.10 (2018), pp. 2942–2954.

[261] N. Vidavsky et al. “Cryo-FIB-SEM serial milling and block face imaging: Large volume structural analysis of biological tissues preserved close to their native state”. *Journal of structural biology* 196.3 (2016), pp. 487–495.

[262] E. Dow et al. “Connectomics of the zebrafish’s lateral-line neuromast reveals wiring and miswiring in a simple microcircuit”. *Elife* 7 (2018), e33988.

[263] R. Friedrich, C. Genoud, and A. A. Wanner. “Analyzing the structure and function of neuronal circuits in zebrafish”. *Frontiers in neural circuits* 7 (2013), p. 71.

[264] A. J. Kievits et al. “How innovations in methodology offer new prospects for volume electron microscopy”. *Journal of microscopy* 287.3 (2022), pp. 114–137.

[265] Z. Zheng et al. “Fast imaging of millimeter-scale areas with beam deflection transmission electron microscopy”. *bioRxiv* (2022), pp. 2022–11.

[266] I. Müllerová and I. Konvalina. “Collection of secondary electrons in scanning electron microscopes”. *Journal of microscopy* 236.3 (2009), pp. 203–210.

[267] A. Šakić et al. “Boron-layer silicon photodiodes for high-efficiency low-energy electron detection”. *Solid-state electronics* 65 (2011), pp. 38–44.

[268] R. Lane et al. “Optimization of negative stage bias potential for faster imaging in large-scale electron microscopy”. *Journal of structural biology: X* 5 (2021), p. 100046.

[269] J. Kuipers, P. de Boer, and B. N. Giepmans. “Scanning EM of non-heavy metal stained biosamples: Large-field of view, high contrast and highly efficient immunolabeling”. *Experimental Cell Research* 337.2 (2015), pp. 202–207.

[270] T. Okumura et al. “Electron tomography of whole cultured cells using novel transmission electron imaging technique”. *Micron* 104 (2018), pp. 21–25.

[271] N. Liv et al. “Simultaneous correlative scanning electron and high-NA fluorescence microscopy”. *PloS one* 8.2 (2013), e55707.

[272] M. Unser, B. L. Trus, and A. C. Steven. “A new resolution criterion based on spectral signal-to-noise ratios”. *Ultramicroscopy* 23.1 (1987), pp. 39–51.

[273] J. P. Buban et al. “High-resolution low-dose scanning transmission electron microscopy”. *Journal of electron microscopy* 59.2 (2010), pp. 103–112.

[274] T. Mullarkey, C. Downing, and L. Jones. “Development of a practicable digital pulse read-out for dark-field STEM”. *Microscopy and Microanalysis* 27.1 (2021), pp. 99–108.

[275] D. C. Joy. “SMART–a program to measure SEM resolution and imaging performance”. *Journal of Microscopy* 208.1 (2002), pp. 24–34.

[276] P. Schauer. “Optimization of decay kinetics of YAG: Ce single crystal scintillators for S (T) EM electron detectors”. *Nuclear Instruments and Methods in Physics Research Section B: Beam Interactions with Materials and Atoms* 269.21 (2011), pp. 2572–2577.

[277] J. Kuipers and B. N. Giepmans. “Neodymium as an alternative contrast for uranium in electron microscopy”. *Histochemistry and cell biology* 153.4 (2020), pp. 271–277.

[278] J. Walton. “Lead asparate, an en bloc contrast stain particularly useful for ultrastructural enzymology.” *Journal of Histochemistry & Cytochemistry* 27.10 (1979), pp. 1337–1342.

[279] R. J. Moerland et al. “Time-resolved cathodoluminescence microscopy with sub-nanosecond beam blanking for direct evaluation of the local density of states”. *Optics Express* 24.21 (2016), pp. 24760–24772.

[280] J. Fermie et al. “High-throughput imaging of biological samples with Delmic’s FAST-EM”. *Microscopy and Microanalysis* 27.S1 (2021), pp. 558–560.

[281] A. Shapson-Coe et al. “A petavoxel fragment of human cerebral cortex reconstructed at nanoscale resolution”. *Science* 384.6696 (2024), eadk4858.

[282] A. J. Kievits et al. “Optical STEM detection for scanning electron microscopy”. *Ultramicroscopy* 256 (2024), p. 113877.

[283] G. Mahalingam et al. “A scalable and modular automated pipeline for stitching of large electron microscopy datasets”. *Elife* 11 (2022), e76534.

[284] M. C. Willingham and A. V. Rutherford. “The use of osmium-thiocarbohydrazide-osmium (OTO) and ferrocyanide-reduced osmium methods to enhance membrane contrast and preservation in cultured cells.” *Journal of Histochemistry & Cytochemistry* 32.4 (1984), pp. 455–460.

[285] S. Saalfeld et al. “Elastic volume reconstruction from series of ultra-thin microscopy sections”. *Nature methods* 9.7 (2012), pp. 717–720.

[286] C.-L. Chiu, N. Clack, et al. “napari: a Python Multi-Dimensional Image Viewer Platform for the Research Community”. *Microscopy and Microanalysis* 28.S1 (2022), pp. 1576–1577.

[287] R. Conrad and K. Narayan. “Instance segmentation of mitochondria in electron microscopy images with a generalist deep learning model trained on a diverse dataset”. *Cell Systems* 14.1 (2023), pp. 58–71.

[288] P. V. Watkins, E. Jelli, and K. L. Briggman. “msemalign: a pipeline for serial section multibeam scanning electron microscopy volume alignment”. *Frontiers in Neuroscience* 17 (2023).

[289] S. Popovych et al. “Petascale pipeline for precise alignment of images from serial section electron microscopy”. *Nature Communications* 15.1 (2024), p. 289.

[290] M. Sievers. “Large-scale connectomics in mouse barrel cortex”. PhD thesis. Sl: sn, 2023.

[291] K. A. Fulton, P. V. Watkins, and K. L. Briggman. “GAUSS-EM: Guided accumulation of ultrathin serial sections with a static magnetic field for volume electron microscopy”. *bioRxiv* (2023), pp. 2023–11.

[292] M. R. Tavakoli et al. “Light-microscopy based dense connectomic reconstruction of mammalian brain tissue”. *bioRxiv* (2024), pp. 2024–03.

[293] R. Lane et al. “Integrated array tomography for 3D correlative light and electron microscopy”. *Frontiers in Molecular Biosciences* 8 (2022), p. 1338.

[294] I. Tanida et al. “Recent advances in in-resin correlative light and electron microscopy of Epon-embedded cells”. *Microscopy* 72.5 (2023), pp. 383–387.

[295] N. Liv et al. “Functional characterization of endo-lysosomal compartments by correlative live-cell and volume electron microscopy”. 177 (2023), pp. 301–326.

[296] J. Fermie et al. “Single organelle dynamics linked to 3D structure by correlative live-cell imaging and 3D electron microscopy”. *Traffic* 19.5 (2018), pp. 354–369.

[297] J. Cazaux. “Some considerations on the electric field induced in insulators by electron bombardment”. *Journal of Applied Physics* 59.5 (1986), pp. 1418–1430.

[298] L. Reimer. “Scanning electron microscopy: physics of image formation and microanalysis”. *Measurement Science and Technology* 11.12 (2000), pp. 1826–1826.

[299] D. C. Joy and C. S. Joy. “Low voltage scanning electron microscopy”. *Micron* 27.3-4 (1996), pp. 247–263.

[300] T. Höche, J. W. Gerlach, and T. Petsch. “Static-charging mitigation and contamination avoidance by selective carbon coating of TEM samples”. *Ultramicroscopy* 106.11-12 (2006), pp. 981–985.

[301] B. Titze. “Techniques to prevent sample surface charging and reduce beam damage effects for SBEM imaging”. PhD thesis. 2013.

[302] R. Egerton. “Control of radiation damage in the TEM”. *Ultramicroscopy* 127 (2013), pp. 100–108.

[303] J. C. Bouwer et al. “Deceleration of probe beam by stage bias potential improves resolution of serial block-face scanning electron microscopic images”. *Advanced structural and chemical imaging* 2 (2016), pp. 1–13.

[304] M. Hugenschmidt et al. “Electron-beam-induced carbon contamination in STEM-in-SEM: Quantification and mitigation”. *Microscopy and Microanalysis* 29.1 (2023), pp. 219–234.

[305] R. F. Crang and K. L. Klomparens. “Artifacts in biological electron microscopy”. *(No Title)* (1988).

[306] R. W. Hoetelmans et al. “Effects of acetone, methanol, or paraformaldehyde on cellular structure, visualized by reflection contrast microscopy and transmission and scanning electron microscopy”. *Applied Immunohistochemistry & Molecular Morphology* 9.4 (2001), pp. 346–351.

[307] E. Sokol et al. “Large-scale electron microscopy maps of patient skin and mucosa provide insight into pathogenesis of blistering diseases”. *Journal of Investigative Dermatology* 135.7 (2015), pp. 1763–1770.

[308] H. Horstmann et al. “Serial section scanning electron microscopy (S 3 EM) on silicon wafers for ultrastructural volume imaging of cells and tissues”. *PloS one* 7.4 (2012), e35172.

[309] P. Baatsen et al. “Preservation of fluorescence signal and imaging optimization for integrated light and electron microscopy”. *Frontiers in Cell and Developmental Biology* 9 (2021), p. 737621.

[310] K. V. Chauhan et al. “Molybdenum and its oxide-based coatings: a review”. *International Journal of Ambient Energy* 43.1 (2022), pp. 2271–2277.

[311] V. S. Saji and C.-W. Lee. “Molybdenum, molybdenum oxides, and their electrochemistry”. *ChemSusChem* 5.7 (2012), pp. 1146–1161.

[312] B. P. Duinkerken et al. “Sample preparation for FAST-EM”. 2025.

[313] M. Kalaswad et al. “Sputter-deposited Mo Thin films: multimodal characterization of structure, surface morphology, density, residual stress, electrical resistivity, and mechanical response”. *Integrating Materials and Manufacturing Innovation* 12.2 (2023), pp. 118–129.

[314] X. Dai et al. “Molybdenum thin films with low resistivity and superior adhesion deposited by radio-frequency magnetron sputtering at elevated temperature”. *Thin Solid Films* 567 (2014), pp. 64–71.

[315] J. Whitacre et al. “Surface roughness and in-plane texturing in sputtered thin films”. *Journal of applied physics* 84.3 (1998), pp. 1346–1353.

[316] D. Mattox. “Surface cleaning in thin film technology”. *Thin Solid Films* 53.1 (1978), pp. 81–96.

[317] G. S. Selwyn et al. “In-situ analysis of particle contamination in magnetron sputtering processes”. *Thin Solid Films* 317.1-2 (1998), pp. 85–92.

[318] V. Founta et al. “Properties of ultrathin molybdenum films for interconnect applications”. *Materialia* 24 (2022), p. 101511.

[319] P. A. Spevack and S. McIntyre. “Reactivity and stability of sulphided thin films of molybdenum to dry air”. *Applied catalysis* 64 (1990), pp. 191–207.

[320] T. B. Stewart and P. D. Fleischauer. “Chemistry of sputtered molybdenum disulfide films”. *Inorganic Chemistry* 21.6 (1982), pp. 2426–2431.

[321] A. List et al. *Oxidation of sputtered thin films of molybdenum alloys at ambient conditions.* na, 2009.

[322] Y. Zhu et al. “In-situ detection of growth striations by crystallization electromotive force measurement during Czochralski crystal growth”. *Journal of Crystal Growth* 475 (2017), pp. 70–76.

[323] N. Ahmed et al. “DC magnetron-sputtered Mo thin films with high adhesion, conductivity and reflectance”. *Journal of Electronic Materials* 49 (2020), pp. 4221–4230.

[324] C. J. Peddie et al. “Correlative super-resolution fluorescence and electron microscopy using conventional fluorescent proteins in vacuo”. *Journal of structural biology* 199.2 (2017), pp. 120–131.

[325] A. Burel et al. “A targeted 3D EM and correlative microscopy method using SEM array tomography”. *Development* 145.12 (2018), dev160879.

[326] M. Scotuzzi et al. “Multi-color electron microscopy by element-guided identification of cells, organelles and molecules”. *Scientific reports* 7.1 (2017), p. 45970.

[327] K. Mocaer et al. “Targeted volume correlative light and electron microscopy of an environmental marine microorganism”. *Journal of Cell Science* 136.15 (2023), jcs261355.

[328] M. A. Karreman et al. “Find your way with X-Ray: using microCT to correlate in vivo imaging with 3D electron microscopy”. *Methods in cell biology.* Vol. 140. Elsevier, 2017, pp. 277–301.

[329] E. B. Bloss et al. “Structured dendritic inhibition supports branch-selective integration in CA1 pyramidal cells”. *Neuron* 89.5 (2016), pp. 1016–1030.

[330] K. D. Micheva et al. “Conduction velocity along the local axons of parvalbumin interneurons correlates with the degree of axonal myelination”. *Cerebral Cortex* 31.7 (2021), pp. 3374–3392.

[331] S. V. Loginov et al. “Correlative organelle microscopy: fluorescence guided volume electron microscopy of intracellular processes”. *Frontiers in Cell and Developmental Biology* 10 (2022), p. 829545.

[332] R. Lane et al. “Label-free fluorescence predictions from large-scale correlative light and electron microscopy data”. *Microscopy and Microanalysis* 27.S1 (2021), pp. 94–95.

[333] S. Karaçoban. “Fluorescence predictions and automatic nuclei segmentation in OSTEM images”. MEP thesis. TU Delft, 2023.

[334] J.-Y. Zhu et al. “Unpaired image-to-image translation using cycle-consistent adversarial networks”. *Proceedings of the IEEE international conference on computer vision.* 2017, pp. 2223–2232.

[335] B. P. Duinkerken et al. “Automated analysis of ultrastructure through large-scale hyperspectral electron microscopy” (2024).

[336] L. van Kessel and C. Hagen. “Nebula: Monte Carlo simulator of electron–matter interaction”. *SoftwareX* 12 (2020), p. 100605.

[337] J. Stopka and P. Kruit. “Statistical Coulomb interactions in multi-beam SEM”. *International Journal of Modern Physics A* 34.36 (2019), p. 1942021.

[338] G. H. Jansen. “Coulomb interactions in particle beams”. *Journal of Vacuum Science & Technology B: Microelectronics Processing and Phenomena* 6.6 (1988), pp. 1977–1983.

[339] X. Jiang, J. Barth, and P. Kruit. “Combined calculation of lens aberrations, space charge aberrations, and statistical Coulomb effects in charged particle optical columns”. *Journal of Vacuum Science & Technology B: Microelectronics and Nanometer Structures Processing, Measurement, and Phenomena* 14.6 (1996), pp. 3747–3752.

[340] M. Kormacheva et al. “BIB-mSTEM Approach for Large Scale Acquisition of Brain Tissue”. Vol. 30. S1. Oxford University Press, 2024, pp. 687–688.

[341] P. Schlegel et al. “Whole-brain annotation and multi-connectome cell typing of Drosophila”. *Nature* 634.8032 (2024), pp. 139–152.

Curriculum Vitæ

Arent Johan Kievits

22-05-1996 Born in Leeuwarden, The Netherlands.

WORK AND RESEARCH EXPERIENCE

2025- Postdoctoral Researcher
Paul Scherrer Institute, Switzerland

EDUCATION

2020–2025 PhD in Imaging Physics
Delft University of Technology, The Netherlands
Thesis: Volume electron microscopy with 64 beams and optical transmission detection
Promotor: Prof. Dr. ir. J. P. Hoogenboom
2nd Promotor: Dr. ir. C. S. Smith

2017–2020 Master of Science in Nanobiology
Delft University of Technology, The Netherlands
Erasmus University Rotterdam, The Netherlands
MSc thesis: Automation of electron diffraction for structural biology
Supervisor: Dr. A. J. Jakobi

2014–2017 Bachelor of Science in Nanobiology
Delft University of Technology, The Netherlands
Erasmus University Rotterdam, The Netherlands

2008–2014 Secondary School
RSG Simon Vestdijk, Harlingen, The Netherlands

ACTIVITIES

2021–2024	Applied Sciences PhD council *Delft University of Technology, The Netherlands*
2022–2023	Applied Sciences Onderdeelcommissie *Delft University of Technology, The Netherlands*

List of Publications

JOURNAL PUBLICATIONS

Arent J Kievits, Ryan Lane, Elizabeth C Carroll, and Jacob P Hoogenboom. “How innovations in methodology offer new prospects for volume electron microscopy”. *Journal of microscopy* 287.3 (2022), pp. 114–137. **Chapter 2 of this thesis**.

Arent J Kievits, B H Peter Duinkerken, Job Fermie, Ryan Lane, Ben N G Giepmans, and Jacob P Hoogenboom. “Optical STEM detection for scanning electron microscopy”. *Ultramicroscopy* 256 (2024), Article 113877. **Chapter 3 of this thesis**.

Arent J Kievits, B H Peter Duinkerken, Ryan Lane, Cecilia de Heus, Daan van Beijeren Bergen en Henegouwen, Tibbe Höppener, Anouk H G Wolters, Nalan Liv, Ben N G Giepmans, and Jacob P Hoogenboom. “FAST-EM array tomography: a workflow for multibeam volume electron microscopy”. *Methods in Microscopy* 1.1 (2024), pp. 49–64. **Chapter 4 of this thesis**.

Maria Kormacheva, **Arent Kievits**, Joakim Reuteler, Marre Niessen, Sander den Hoedt, Safe Khan, Carles Bosch, Jacob Hoogenboom, Andreas Schaefer, and Adrian Wanner. “BIB-mSTEM Approach for Large Scale Acquisition of Brain Tissue”. *Microscopy and Microanalysis* 30 (2024), pp. 687–688.

Arent J Kievits, Monika Molnar, and Jacob P Hoogenboom. “Optimizing optical STEM detection for faster acquisition speeds in scanning electron microscopy”. *BIO Web of Conferences* 129 (2024), Article 05035.

B H Peter Duinkerken, **Arent J Kievits**, Anouk H G Wolters, Daan van Beijeren Bergen en Henegouwen, Jeroen Kuipers, Jacob P Hoogenboom, and Ben N G Giepmans. “Sample processing and benchmarking for optical STEM-based multibeam imaging”. *Microscopy and Microanalysis* 31.2 (2025), ozaf024.

SOFTWARE REPOSITORIES

Tibbe Höppener, Ryan Lane, and Arent J Kievits. *scripted-render-pipeline*. Version 0.0.1. July 2024. DOI: `10.5281/zenodo.12733386`.

Ryan Lane and Arent J Kievits. *interactive-render-workflow*. Version 0.0.1. July 2024. DOI: `10.5281/zenodo.12733815`.

Arent J Kievits. *fastem-sofima*. Version 0.0.1. July 2024. `DOI:10.5281/zenodo.12733905`.

PUBLISHED DATASETS

Arent J Kievits, B H Peter Duinkerken, Job Fermie, Ryan Lane, Ben N G Giepmans, and Jacob P Hoogenboom. *Microscopy data, code and analysis underlying the publication "Optical STEM detection for scanning electron microscopy"*. October 2023. DOI: `10.4121/9c98aee1-608e-4c71-8b89-dcb1e8eb3e5e.v2`

Arent J Kievits, B H Peter Duinkerken, Ryan Lane, Cecilia de Heus, Daan van Beijeren Bergen en Henegouwen, Tibbe Höppener, Anouk H G Wolters, Nalan Liv, Ben N G Giepmans, and Jacob P Hoogenboom. *Sample dataset and software for FAST-EM array tomography*. July 2024. DOI: `10.4121/bf3f2b23-2328-4d81-a0f4-05fdb33117d7.v2`

Arent J Kievits, B H Peter Duinkerken, Ryan Lane, Cecilia de Heus, Daan van Beijeren Bergen en Henegouwen, Tibbe Höppener, Anouk H G Wolters, Nalan Liv, Ben N G Giepmans, and Jacob P Hoogenboom. *FAST-EM array tomography data of rat pancreas prepared with rOTO protocol and stained with neodymium acetate*. June 2024. DOI: `10.6019/empiar-12174`.

Arent J Kievits *et al. FAST-EM array tomography data of wild-type MCF-7 cells prepared with the rOTO protocol and stained with uranyl acetate*. June 2024. DOI: `10.6019/empiar-12190`.

Arent J Kievits *et al. FAST-EM array tomography data of wild-type MCF-7 cells prepared with the rOTO protocol and stained with neodymium acetate*. November 2024. DOI: `10.6019/EMPIAR-12193`.

Arent J Kievits. *Data supporting the doctoral thesis "Volume electron microscopy with 64 beams and optical transmission detection"*. December 2024. DOI: `10.4121/01efed58-9427-478a-8687-50b35daf3d9c.v1`.

SUPERVISED STUDENT PROJECTS

Marc Abels. "On CLEMnet: Fluorescence prediction on electron microscopy data without complementary fluorescence data". BEP thesis. Delft University of Technology, September 2021 - March 2022.

Rayen Khazraoui. "Investigation of potential saturation effects in optical scanning electron microscopy". BEP thesis. Delft University of Technology, October 2021 - February 2022.

Luna Feeke. "Optimization of substrate design for FAST-EM multibeam". BEP thesis. Delft University of Technology, August 2022 - November 2022.

Wilco van Nes. "Lytic Granule segmentation in volume electron microscopy data using convolutional neural networks". BEP thesis. Delft University of Technology, February 2023 - July 2023.